Models for Amorphous Calcium Carbonate

by

Sourabh Sinha

A Dissertation Presented in Partial Fulfillment
of the Requirements for the Degree
Doctor of Philosophy

Approved December 2011 by the
Graduate Supervisory Committee:

Peter Rez, Chair
Hamdallah A. Bearat
Peter A. Bennett
Martha R. McCartney
Xihong Peng

ARIZONA STATE UNIVERSITY

May 2012

ABSTRACT

Many species e.g. sea urchin form amorphous calcium carbonate (ACC) precursor phases that subsequently transform into crystalline $CaCO_3$. It is certainly possible that the biogenic ACC might have more than 10 wt% Mg and $\sim$3 wt% of water. The structure of ACC and the mechanisms by which it transforms to crystalline phase are still poorly understood. In this dissertation our goal is to determine an atomic structure model that is consistent with diffraction and IR measurements of ACC. For this purpose a calcite supercell with 24 formula units, containing 120 atoms, was constructed. Various configurations with substitution of Ca by 6 Mg ions (6 wt.%) and insertion of 3-5 H_2O molecules (2.25-3.75 wt.%) in the interstitial positions of the supercell, were relaxed using a robust density function code VASP. The most noticeable effects were the tilts of CO_3 groups and the distortion of Ca sub-lattice, especially in the hydrated case. The distributions of Ca-Ca nearest neighbor distance and CO_3 tilts were extracted from various configurations. The same methods were also applied to aragonite. Sampling from the calculated distortion distributions, we built models for amorphous calcite/aragonite of size $\sim$ 1700 nm^3 based on a multi-scale modeling scheme. We used these models to generate diffraction patterns and profiles with our diffraction code. We found that the induced distortions were not enough to generate a diffraction profile typical of an amorphous material. We then studied the diffraction profiles from several nano-crystallites as recent studies suggest that ACC might be a random array of nano-cryatallites. It was found that the generated diffraction profile from a nano-crystallite of size $\sim$ 2 nm^3 is similar to that from the ACC.

To Ma Baba

ACKNOWLEDGEMENTS

I was privileged to work with my adviser professor Peter Rez who introduced me to the exciting and upcoming field of bio-mineralization. Off course I am grateful for his guidance but the thing which I appreciated most was the freedom he gave me. As a result, I was never rushed and got plenty of opportunities to learn and understand many intricate concepts, involved lessons by myself. The pleasure it brought to me was really the prize, as far as I am concerned. I also thank my committee members for correcting the errors and typos in this manuscript, hopefully it's error-free now!

Next, my big thanks to my great friend Dr. Raman Narayan. This work has greatly benefited from many useful discussions on diffraction, numerical analysis...with you buddy. I also thank my other classmates, specially Dr. Hermann Don-Fuck, Dr. Adam De-Graff for their frequent suggestions. Beyond the academic interactions, I should not forget to mention the great time four of us had in the tennis court.

How can I forget the teachers who shaped my life. I was really fortunate to learn from Professors like J. Page, K. Schmidt, A. K. Dutta, K. P. Maheshwari, R. Nityananda...just to name a few. I learned a lot from them and can certainly say: their unique teaching styles, incredible depth in physics and the way of approaching problems left a permanent impression on me. The story would certainly not be complete without mentioning my previous adviser Prof. John Shumway. Working with him I realized what it takes to be a good at anything (not just physics!). Finally I must to thank ASU physics department for their financial support through teaching assistantship.

Now my closest people – my parents, wife, sisters, family friends – without whose constant support and motivation I would not even come anywhere near, to you all: I am grateful to have you guys in my life. Let me tell you one thing, all this hard work would be worth and meaningful if it brings even a little bit of joy and happiness to you!

TABLE OF CONTENTS

Page

LIST OF TABLES viii

LIST OF FIGURES ix

CHAPTER

1 INTRODUCTION 1

1.1 Biomineralization and its Importance 1

1.2 Calcium Carbonate as a Biomineral 2

1.3 Amorphous Calcium Carbonate (ACC) 4

1.4 Role of H_2O, Mg, Proteins and Macromolecules on Biomineralization and ACC 9

1.5 ACC as Nano Particles 12

1.6 Amorphous Materials and Disorder 12

1.7 Our Approach 13

2 ELECTRONIC STRUCTURE CALCULATION 15

2.1 Quantum Many-Body Hamiltonian 15

2.2 Born-Oppenheimer Approximation 16

2.3 Hartree Theory 17

2.4 Hartree-Fock Theory 18

2.5 Density Functional Theory (DFT) 19

2.5.1 The Hohenberg-Kohn Theorem 20

Chapter Page

2.5.2 The Kohn-Sham Ansatz 21

2.5.3 The Local Density Approximation 23

2.5.4 Working principle of VASP 24

3 THEORY OF DIFFRACTION AND CODE ARCHITECTURE 26

3.1 Reciprocal Lattice 26

3.2 Diffraction Condition Bragg Equation 27

3.3 Ewald Sphere Construction 29

3.4 Scattering Factors 31

3.5 Relationship between Diffracted Peak Width and Crystal Size 33

3.6 Diffraction Code Construction (Flowchart) 35

3.7 Evaluation of the diffraction code 38

4 DENSITY FUNCTIONAL CALCULATIONS 42

4.1 Simulation Systems for VASP 42

4.1.1 Calcite 42

4.1.2 Aragonite 45

4.2 Free Energy Calculation of the Relaxed Structures 46

4.3 CO_3 Tilt and Ca-Ca Nearest Neighbor Distance (NND) Distributions . . 49

4.3.1 Tilt of the Carbonate Planes for Calcite 49

4.3.2 Distortion of calcium sub-lattice for Calcite 61

4.3.3 Tilt of the Carbonate Planes for Aragonite 64

4.3.4 Distortion of calcium sub-lattice for Aragonite 74

Chapter Page

5 MODELING OF AMORPHOUS CALCIUM CARBONATE 77

5.1 Hypothesis Regarding Amorphization of $CaCO_3$ 77

5.2 Carbonate Tilts in Terms of Polar and Azimuthal Angles (θ, ϕ) 78

5.3 Modeling of Amorphous Calcium Carbonate (ACC) 80

5.3.1 Random Sampling from a Distribution 80

5.3.2 Random Sampling from the θ Distribution 82

5.3.3 Random Sampling from the ϕ Distribution 84

5.3.4 Sampling from Ca-Ca Nearest Neighbor Distance (NND) Distribution 87

5.4 Effects of Distortions on Calcite Diffraction Line Profile 89

5.4.1 Carbonate Tilts Only 89

5.4.2 Ca-Ca Sub-lattice Distortion Only 91

5.4.3 Carbonate Tilts and Ca Sub-Lattice Distortion 93

5.4.4 Carbonates Tilts, Ca and C Sub-lattice Distortions 95

5.5 Effects of Distortions on Aragonite Diffraction Line Profile 96

5.5.1 Carbonate Tilts Only 96

5.5.2 Ca Sub-lattice Distortion Only 98

5.5.3 Carbonate Tilts and Ca Sub-Lattice Distortion 100

5.5.4 Carbonate Tilts Combined with Ca and C Sub-lattice Distortions 101

5.6 Discussions and Evaluation of the Hypothesis 102

6 ACC AS NANO-CRYSTALLITES 104

Chapter Page

6.1 Diffraction Profile of the Calcite Nano-Crystallites 104

6.1.1 1x of calcite Supercell 104

6.1.2 2x of calcite Supercell 106

6.1.3 3x of calcite Supercell 107

6.2 Diffraction Profile of the Aragonite Nano-Crystallites 108

6.2.1 1x of aragonite Supercell 108

6.2.2 2x of aragonite Supercell 110

6.2.3 3x of aragonite Supercell 111

6.3 Diffraction Line Profile of Nano-crystallites with Distortions 112

6.3.1 Calcite 112

6.3.2 Aragonite 113

6.3.3 Discussion 114

6.4 Experimental (TEM) Results 115

6.5 Comparison between Theory and Experiment 119

7 CONCLUSION 121

REFERENCES 124

APPENDIX

A THE DIFFRACTION CODE 131

LIST OF TABLES

Table		Page
3.1	Parametrized electron scattering factors for C, O, Ca	33
4.1	Ω_{cl} for clustered impurity configurations	48
4.2	Free energy calculations for calcite	48
4.3	Free energy calculations for aragonite	48
4.4	Angle between normals of O-subgroup in CO_3 groups for 4 clustered water calcite relaxed structure.	51
4.5	Fractional percentage change in individual C-O distance in CO_3 groups for four clustered water calcite relaxed structure. Original C-O bond length in perfect Calcite is 1.292 $\AA$.	52
4.6	Range of tilt angle distributions for simulated calcite supercell with impurities.	59
4.7	Ca-Ca nearest neighbor distance in calcite for all the simulation systems.	63
4.8	Angle between normals of O-subgroup in CO_3 groups for 4 clustered water aragonite relaxed structure.	65
4.9	Fractional percentage change in individual C-O distance in CO_3 groups for four clustered water aragonite relaxed structure. Original C-O bond length in perfect Aragonite is 1.284 $\AA$.	67
4.10	Range of tilt angle distributions for all the simulated aragonite systems.	72
4.11	Ca-Ca nearest neighbor distance in aragonite.	76
5.1	Range of θ and ϕ distributions for simulated calcite supercell with impurities.	79
5.2	Range of θ and ϕ distributions for simulated aragonite supercell with impurities.	79
5.3	Model parameters for the carbonate tilts	87

LIST OF FIGURES

Figure Page

1.1 Scanning electron micrographs of regenerating spines of the sea urchin *Paracentrotus lividus*. (A) Five-day-old regenerated spine growing on the original broken spine. (B) Higher magnification view of the tip of the new growth, showing the typical stereom structure and the protruding newly formed microspines. (C) One microspine formed after 4 days of regeneration, observed fresh. (D) Four-day-old microspine, etched in water while fresh. (E) Four-day-old microspine, etched in water 1 month after regeneration. [Addadi *et al.*, *SCIENCE*, 306 (2004)] 3

1.2 SEM micrographs of the surfaces of triradite sea urchin spicules after etching with *(a)* double-distilled water and *(b)* 1 M KOH. [Beniash *et al., Proc. R. Soc. Lond. B, 264* (1997)]. 4

1.3 Transmission electron micrographs (TEM) and electron diffraction patterns of particles removed from fresh regenerated spines of the sea urchin Paracentrotus lividus. (A) Electron diffraction pattern of the particles observed immediately after removal from the spine; the diffuse rings indicate the presence of an amorphous material. (Inset) TEM of the particles. Bar, 50 nm. (B) Electron diffraction pattern of the same particles as in (A) after 3 weeks on the grid. The most prevalent diffraction peaks correspond to a d-spacing of 3.04 Å, characteristic of the calcite plane 104. They are detected up to fourth order (arrows, enhanced contrast in window). (Inset) TEM of the particles. Bar, 50 nm. [Addadi *et al.*, *SCIENCE*, 306 (2004)]. . 6

1.4 (*a*) Infrared spectrum of sea urchin larval spicules. The peak at 1420 cm^{-1} corresponds to the ν_3 absorption band; the broad peak centred at 1086 cm^{-1} belongs to the ν_1 absorption band of amorphous $CaCO_3$; the peaks at 874 and 713 cm^{-1} correspond to 2 and 4 absorption bands of calcite, respectively. (*b*) Portions of the infrared spectra of amorphous $CaCO_3$, three spectra of sea urchin larval spicules at different stages of development and geological calcite, showing the ν_2 and ν_4 absorptions. The ratios of the maximal intensities of the ν_2 versus the ν_4 absorption bands are presented. [Beniash *et al.*, *Proc. R. Soc. Lond. B*, 264 (1997)] 8

2.1 Flowchart of the working principle of DFT-code VASP 25

3.1 Schematics of elastic scattering from a sample 27

3.2 Ewald sphere construction of a two dimensional lattice 30

3.3 The schematic shows a finite crystal is equivalent to the convolution of an infinite crystal with a finite aparture 34

3.4 Architecture of the diffraction code 37

3.5 Calcite powder diffraction line profile from database (CrystalMaker software library) 38

3.6 Calcite powder diffraction line profile from our diffraction software 39

3.7 Comparison between peak-widths of $10\times10\times17(\text{Å})^3$ and $20\times20\times34\text{Å}^3$ calcite crystals. $\lambda = 0.025\text{Å}$. 41

4.1 A pure calcite supercell viewed down the [100] direction. Color code: Blue = Ca, Red = O, Green = C 43

4.2 Polyhedral view of a pure calcite crystal. Notice, the orientation of triangular carbonate planes and the Ca coordination polyhedral (regular octahedron). 44

4.3 A pure aragonite supercell when viewed from (100) direction. Color code: Blue = Ca, Red = O, Green = C 45

4.4 Orientation of carbonate groups in a pure aragonite crystal. Like in calcite, they are also oriented parallel to the basal plane (001) 46
4.5 Schematics of carbonate tilt 49
4.6 Before relaxation, 4 clustered H_2O molecules inserted in a pure calcite. H atoms are shown in pink 53
4.7 After relaxation, 4 clustered H_2O molecules + calcite system. Notice the tilting of the carbonate planes in the vicinity of H_2O molecule 54
4.8 Polyhedral view of 4 clustered H_2O molecules + calcite system after relaxation. Notice the carbonate plane tilts and distortion of the polyhedron shapes when compared with figure 4.2 55
4.9 Before relaxation, polyhedral view of 6 clustered Mg atoms replacing 6 Ca atoms in a pure calcite. Notice the orderliness of the carbonate planes in the vicinity of impurities and the shapes of the polyhedra formed by Ca atoms. Notice that the carbonate planes are all parallel to the basal plane (001) . . . 56
4.10 Polyhedral view of 6 clustered Mg atoms replacing 6 Ca atoms in a pure calcite after relaxation. Comparing it with figure (4.8) reveals that the tilts of the carbonate planes in the vicinity of impurities but the shapes of the Ca coordination polyhedra are almost unchanged, suggesting there was not much distortion of the Ca sub-lattice 57
4.11 Carbonate $tilt_1$ histogram in 5 clustered H_2O molecules impurities in the calcite system after relaxation. Refer to figure (4.5) for definition of $tilt_1$. . . 58
4.12 Carbonate $tilt_2$ histogram in 5 clustered H_2O molecules impurities in the calcite system after relaxation. Refer to figure (4.5) for definition of $tilt_2$. . . 59
4.13 Carbonate $tilt_3$ histogram in 5 clustered H_2O molecules impurities in the calcite system after relaxation. Refer to figure (4.5) for definition of $tilt_3$. . . 60

4.14 Ca sub-lattice with 4 clustered H_2O molecules as impurities in calcite system. The color blue and yellow represents the Ca ion positions before and after relaxation. Notice greater distortion (compare with figure (4.7)) near the middle of the cell where H_2O molecules were inserted 61

4.15 Polyhedra formed by Ca atoms in 4 clustered H_2O molecules + calcite system after relaxation. Notice the change of polyhedron shapes (compare with figure (4.2)) which suggests distortion of Ca sub-lattice 62

4.16 Ca-Ca nearest neighbor distance distribution in 5 clustered H_2O molecules impurities in calcite system after relaxation. 63

4.17 Before relaxation, 4 clustered H_2O molecules inserted in a pure aragonite. H atoms are shown in pink. Notice the order of the carbonate planes in the vicinity of H_2O molecules and that they are all parallel to the basal plane (001) 66

4.18 After relaxation, 4 clustered H_2O molecules + aragonite system. Notice the tilting of the carbonate planes and the distortion of bonds in the vicinity of H_2O molecules. Compare with figure (4.17) to notice the distortion especially in the middle of the cell where impurities were inserted 68

4.19 Carbonate group orientations after relaxation of 4 clustered H_2O molecules + aragonite system. Compare with figure (4.4) to notice the carbonate tilts. . 69

4.20 Before relaxation, 6 clustered Mg atoms replacing 6 Ca atoms in a pure aragonite. Notice that the carbonate planes in the vicinity of impurities are all parallel to the basal plane 70

4.21 After relaxation, 6 clustered Mg atoms replacing 6 Ca atoms in a pure aragonite. Notice that there is not much distortion after relaxation (compare with figure (4.20)) 71

4.22 Carbonate $tilt_1$ histogram in 4 clustered H_2O molecules impurities in the aragonite system after relaxation. Refer to figure (4.5) for definition of $tilt_1$. 72

4.23 Carbonate $tilt_2$ histogram in 4 clustered H_2O molecules impurities in the aragonite system after relaxation. Refer to figure (4.5) for definition of $tilt_2$. 73

4.24 Carbonate $tilt_3$ histogram in 4 clustered H_2O molecules impurities in aragonite system after relaxation. Refer to figure (4.5) for definition of $tilt_3$. . . 74

4.25 Ca sub-lattice in 4 clustered H_2O molecules as impurities in aragonite system. The color blue and yellow represents the Ca ion positions before and after relaxation. Notice more distortion (compare with figure (4.17)) near the middle of the cell where H_2O molecules were inserted. 75

4.26 Ca-Ca nearest neighbor distance distribution in 4 clustered H_2O molecules impurities in aragonite system after relaxation. 76

5.1 Conversion of tilt angles to the polar angle θ and azimuthal angle ϕ. 78

5.2 Schematics of randomly sampling from a distribution $f(x)$. The blue curve is the normalized PDF of x and red curve is the corresponding CDF. R is a random number drawn from the uniform distribution between 0 to 1. 81

5.3 θ distribution and its best linear fit for 5 clustered H_2O molecules as impurities in calcite system after relaxation. 82

5.4 θ distribution and its best linear fit for 4 clustered H_2O molecules as impurities in aragonite system after relaxation. 83

5.5 ϕ distribution for 5 clustered H_2O molecules + calcite system after relaxation. 85

5.6 ϕ distribution for 4 clustered H_2O molecules + aragonite system after relaxation. 86

5.7 Powder diffraction line profile of a $\sim 100 \times 100 \times 170$ $\AA^3$ calcite crystal containing only carbonate tilts. 90

5.8 Semi-log plot of figure (5.7) to show the small diffraction peaks. 91

5.9 Powder diffraction line profile of a $\sim 100 \times 100 \times 170$ $\AA^3$ Calcite crystal containing only Ca sub-lattice distortion. 92

5.10 Semi-log plot of figure (5.9) to zoon the small diffraction peaks. 93

5.11 Powder diffraction line profile of a $\sim 100 \times 100 \times 170$ $\AA^3$ calcite crystal containing CO_3 tilts + Ca sub-lattice distortion. 94

5.12 Powder diffraction line profile of a $\sim 100 \times 100 \times 170$ $\AA^3$ calcite crystal with CO_3 tilts, C and Ca sub-lattice distortion. 95

5.13 Powder diffraction line profile of a $\sim 100 \times 80 \times 170$ $\AA^3$ aragonite crystal containing only carbonate tilts. 97

5.14 Semi-log plot of figure (5.13) to zoom the small diffraction peaks. 98

5.15 Powder diffraction line profile of a $\sim 100 \times 80 \times 170$ $\AA^3$ aragonite with only Ca sub-lattice distortion. 99

5.16 Semi-log plot of figure (5.15) to zoom the small diffraction peaks. 100

5.17 Powder diffraction line profile of a $\sim 100 \times 80 \times 170$ $\AA^3$ aragonite crystal with CO3 tilts + Ca sub-lattice distortion. 101

5.18 Powder diffraction line profile of a $\sim 100 \sim 80 \sim 170$ $\AA^3$ aragonite crystal with CO_3 tilts + Ca sub-lattice distortion + C sub-lattice distortion. 102

6.1 Powder diffraction line profile (blue) of a $\sim 10 \times 10 \times 17$ $\AA^3$ calcite nanocrystallite. Perfect crystal calcite diffraction line profile (red) was superimposed for comparison. 105

6.2 Powder diffraction line profile (blue) of a $\sim 20 \times 20 \times 35$ $\AA^3$ calcite nanocrystallite. Perfect crystal calcite diffraction line profile (red) was superimposed for comparison. 106

6.3 Powder diffraction line profile (blue) of a $\sim 30 \times 30 \times 50$ $\AA^3$ calcite nanocrystallite. Perfect crystal calcite diffraction line profile (red) was superimposed for comparison. 107

6.4 Powder diffraction line profile (blue) of a $\sim 10 \times 10 \times 20$ $\AA^3$ aragonite nanocrystallite. Perfect crystal aragonite diffraction line profile (red) was superimposed for comparison. 109

6.5 Powder diffraction line profile (blue) of a $\sim 20 \times 20 \times 40\,\mathring{A}^3$ aragonite nano-crystallite. Perfect crystal aragonite diffraction line profile (red) was superimposed for comparison. 110

6.6 Powder diffraction line profile (blue) of a $\sim 30 \times 30 \times 60\,\mathring{A}^3$ aragonite nano-crystallite. Perfect crystal aragonite diffraction line profile (red) was superimposed for comparison. 111

6.7 Powder diffraction line profile (blue) of a $\sim 10 \times 10 \times 17\,\mathring{A}^3$ calcite nano-crystallite with CO_3 tilts + Ca sub-lattice distortion + C sub-lattice distortions. Pure calcite diffraction line profile (red) was plotted on same scale for comparison. 113

6.8 Powder diffraction line profile (blue) of a $\sim 10 \times 10 \times 20\,\mathring{A}^3$ aragonite nano-crystallite with CO_3 tilts + Ca sub-lattice distortion + C sub-lattice distortions. Pure aragonite diffraction line profile (red) was superimposed for comparison. 114

6.9 Transmission electron microscopy (200 keV electron beam) image (i) of amorphous calcium carbonate 115

6.10 Annulus integrated diffracted line profile (blue) of image (i). Diffraction line profile of a $\sim 10 \times 10 \times 17\,\mathring{A}^3$ calcite nano-crystallite (red) is shown on the same scale for comparison purpose. 116

6.11 Another TEM (200 keV electron beam) image (ii) of amorphous calcium carbonate 117

6.12 Annulus integrated diffracted line profile (blue) of image (ii). The baseline (red dots) points were fitted a second order polynomial (greenish-blue curve). 118

6.13 Baseline subtracted annulus integrated diffraction profile (blue) of image (ii). Diffraction line profile of a $\sim 10 \times 10 \times 17\,\mathring{A}^3$ calcite nano-crystallite (red) is shown on the same scale for comparison purpose. 119

Chapter 1

INTRODUCTION

1.1 Biomineralization and its Importance

The formation of minerals by organisms − Biomineralization − is a widespread phenomenon in nature [1, 2, 3]. Biominerals are composites of organic molecules and minerals that serve a variety of functions in different organisms. Some familiar biomineral composites with important biological functions are bones, teeth, and shells in mollusks. Other biominerals like kidney-stones are pathological and a sign of disease. Almost 70 different forms of biominerals , which includes oxides; sulfides; carbonates; phosphates; oxalates and silica families, exist in nature formed by organisms from all over the animal kingdom. Despite the small percentage of organics (0.15 wt. %) [4, 5], with the exception of bone which has $\sim$ 33 wt.% of organics, biomineral composites have vastly different materials properties compared to their geologic counterparts. The biominerals adopt complex shapes, are often aligned to form arrays, and serve a number of useful purposes in organisms, such as mechanical functions of exo- and endo-skeletons, stiffening of soft tissues, temporary storage, metabolic energy generation, navigation in the earth's magnetic field, orientation in the gravity field, light amplification and transmission and much more. What interests the broad scientific community in the field of biomineralogy is that the structure and formation of biominerals are controlled over different length scales by macromolecules such as proteins, lipids, glycoproteins, and polysaccharides [1, 2, 3]. In some cases, these processes lead to the formation of composite structures that incorporate macromolecules on or within the mineral phases themselves. Materials scientists are striving to understand how to synthesize composite materials that outperform their individual constituents, while in nature such remarkable materials have evolved since the Cambrian period, for more than 500 million years [6]. A striking example is nacre, or mother-of-pearl: this

is a layered composite of proteins and aragonite, 3000 times more resistant to fracture than aragonite [7]. Another example of materials design strategies in nature are sea urchin skeletal elements, comprising single calcite crystals of intricate morphology [8, 9]. Although progress is being made in understanding how macromolecules control biomineral formation, the underlying mechanisms responsible for the formation of most biomineralized structures remain elusive.

1.2 Calcium Carbonate as a Biomineral

Calcium carbonate is the most prominent biomineral in terms of global turnover[3]. It is a common substance found in rocks in all parts of the world, and is the main component of shells of marine organisms, snails, coal balls, pearls, and eggshells. Calcium carbonate is the active ingredient in agricultural lime, and is usually the principal cause of hard water. Apart from its natural use by the animals and living organisms, it has practical application in many areas e.g. household, industry, medicine. Calcium carbonate occurs in three anhydrous polymorphic forms − calcite, aragonite and vaterite, where the thermodynamic stability decreases from calcite to vaterite [3]. In addition, two crystallographically defined pseudopolymorphs are known: monohydrocalcite [10, 1, 12] ($CaCO_3.H_2O$), and the hexahydrate form ($CaCO_3.6H_2O$) − the mineral ikaite [12, 13]. Amorphous calcium carbonate (ACC) with variable composition is also well known. The most prevalent, but certainly not the only use of calcium carbonate is in the formation of shells and crusts by a wide variety of undersea animals [14]. Its natural formation generally takes place in specialized, self-assembled components, such as vesicles or layered macromolecular structures, where domains of acidic proteins induce oriented nucleation [15, 16]. Animals have a remarkable ability to control the structure and morphology of calcium carbonate crystals and thus are able to optimize their functionality [17, 18]. For example, Sea urchin teeth are remarkable and complex calcite structures [19], continuously growing at the forming end and self-sharpening at

the mature grinding tip. The calcite crystals of tooth components, plates, fibers, and a high-Mg polycrystalline matrix, have highly co-oriented crystallographic axes. This ability to co-orient calcite in a mineralized structure is shared by all echinoderms. However, the physicochemical mechanism by which calcite crystals become co-oriented in echinoderms remains enigmatic. Artificially we can control the nucleation of calcium carbonate to some degree by the addition of additives to precipitation mixtures [20, 21].

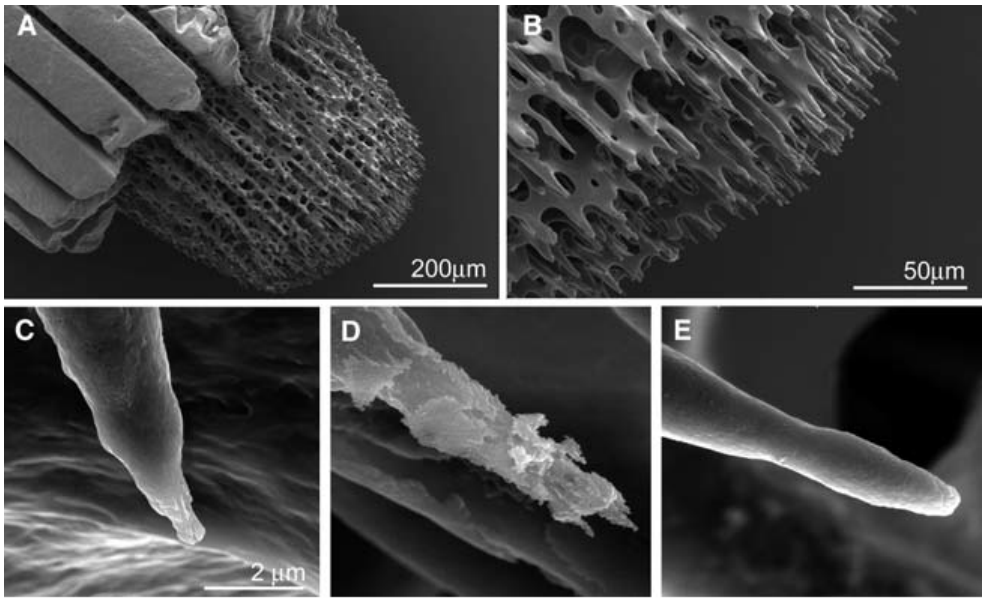

Figure 1.1: Scanning electron micrographs of regenerating spines of the sea urchin *Paracentrotus lividus*. (A) Five-day-old regenerated spine growing on the original broken spine. (B) Higher magnification view of the tip of the new growth, showing the typical stereom structure and the protruding newly formed microspines. (C) One microspine formed after 4 days of regeneration, observed fresh. (D) Four-day-old microspine, etched in water while fresh. (E) Four-day-old microspine, etched in water 1 month after regeneration. [Addadi *et al.*, *SCIENCE*, 306 (2004)]

1.3 Amorphous Calcium Carbonate (ACC)

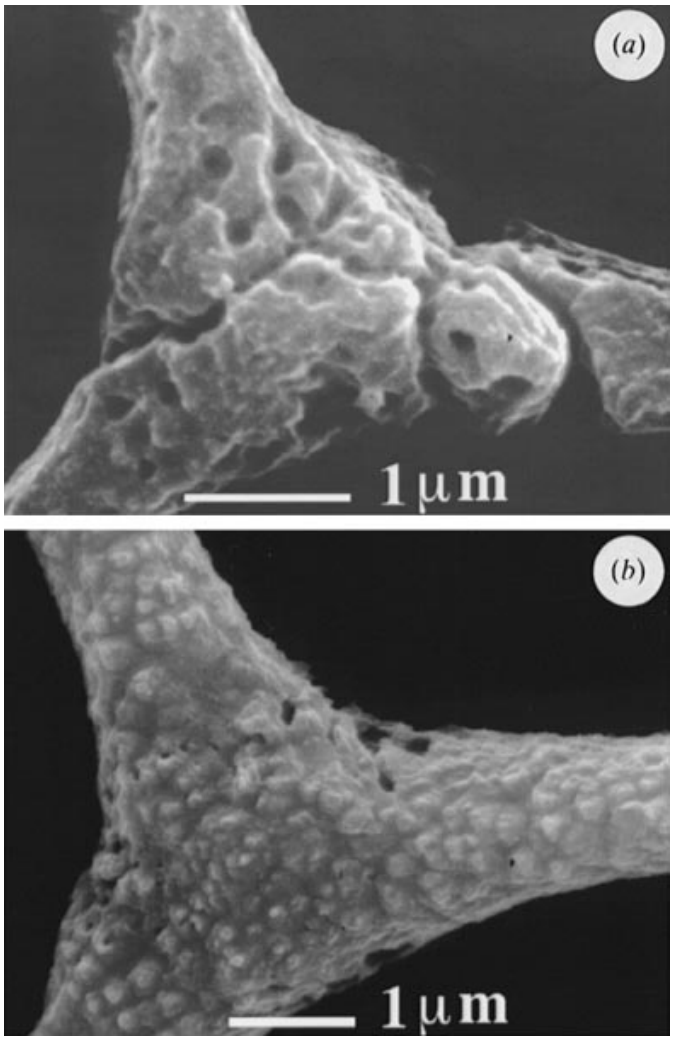

Figure 1.2: SEM micrographs of the surfaces of triradite sea urchin spicules after etching with *(a)* double-distilled water and *(b)* 1 M KOH. [Beniash *et al., Proc. R. Soc. Lond. B, 264* (1997)].

Amorphous calcium carbonate or ACC is an intrinsically metastable phase. In the laboratory it can be formed in supersaturated solutions of calcium and carbonate, but transforms into the stable crystalline phase (calcite or aragonite) within minutes of its formation [22]. Nevertheless, it is formed by at least 15 genera from 7 different animal phyla, and is also formed in leaves of certain plants [23]. Furthermore, in many cases

the biogenic ACC is stable in the organism [3], examples are the cystoliths in leaves of certain plants [25] and exoskeletons of crustaceans [3].

As a general rule, ACC is only stable during the lifetime of the animal, and its characterization is difficult because it usually requires performing in situ experiments. Biogenic calcium carbonate that is first deposited as ACC and subsequently transforms into calcite was first observed in the case of sea urchin larval spicule [26]. Later it was also observed that ACC crystallizes to aragonite in the case of two species of larval bivalves [27]. Recent findings show that the ACC precursor phase strategy is widespread among invertebrates, an example would be its presence in earthworms calciferous gland [28]. Both the magnesium and water content vary among biogenic amorphous calcium carbonate phases with up to 45 % (atomic) Mg being observed in the sea urchin tooth [29]. Some ACC has water content similar to monohydrocalcite while others are believed to be anhydrous. Abiotically amorphous calcium carbonate can also be synthesized in the laboratory most easily by reacting aqueous solution of $CaCl_2$ and Na_2CO_3 at high pH [30] at or below room temperature. These solutions can be totally inorganic or they can contain small organic species which affect the formation and persistence of ACC [31]. The chemically precipitated ACC is also variable in particle size and water content and transforms to a less hydrated or anhydrous form upon heating before crystallization [32]. The formation of ACC, both biotically and abiotically, and its subsequent transformation mechanisms to the stable crystalline phases are still very poorly understood. Classical nucleation theory completely fails to explain [33] the transformation of ACC into single crystal calcite. Also we do not have a clear understanding of the atomic structure of ACC so far. There are many other unanswered perplexing issues directly related to the ACC growth, e.g. how a single crystal of calcite can be molded into such convoluted shapes when inorganically formed calcite crystals are rhombohedra with flat crystal faces, or how the cells can efficiently provide the ions and, at the same time, efficiently remove water, during and after crystal deposition.

The amorphous nature of ACC makes the structural characterization difficult, and the applications of more complex analytical techniques are necessary to provide enough information on the short-range order.

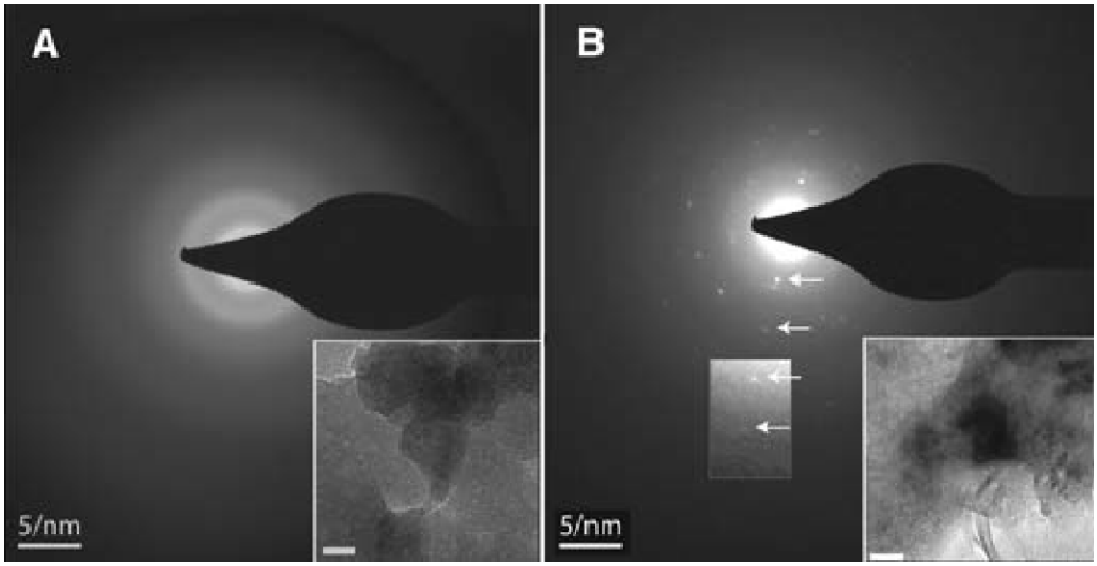

Figure 1.3: Transmission electron micrographs (TEM) and electron diffraction patterns of particles removed from fresh regenerated spines of the sea urchin Paracentrotus lividus. (A) Electron diffraction pattern of the particles observed immediately after removal from the spine; the diffuse rings indicate the presence of an amorphous material. (Inset) TEM of the particles. Bar, 50 nm. (B) Electron diffraction pattern of the same particles as in (A) after 3 weeks on the grid. The most prevalent diffraction peaks correspond to a d-spacing of 3.04 Å, characteristic of the calcite plane 104. They are detected up to fourth order (arrows, enhanced contrast in window). (Inset) TEM of the particles. Bar, 50 nm. [Addadi *et al*., *SCIENCE*, 306 (2004)].

Recent work has suggested that prenucleation clusters of calcium and carbonate ions are the first stage in the formation of biogenic calcite [33]. These clusters aggregate as ACC and eventually transforms into single crystal calcite or aragonite. Variations in the pair distribution function of ACC suggest [34] that this phase can rapidly modify its local order through changes in the number of atoms surrounding a given calcium ion, and that can consequently play an important role in the formation of a particular crystalline phase. The general consensus is that ACC transforms with aging or heating into a less hydrated form, and with time crystallizes to calcite or aragonite. Transforma-

tion and crystallization of ACC can follow an energetically downhill sequence: more metastable hydrated ACC → less metastable hydrated ACC → anhydrous ACC → biogenic anhydrous ACC → vaterite → aragonite → calcite, though not all these phases need to occur necessarily in a given transformation sequence [35]. Range of sophisticated experimental techniques e.g. XRD [35], electron-microscopy [36], NMR [37], IR [38] and Raman spectroscopy [36] are used to date to characterize/analyze ACC. The most prominent physical properties of ACC are probably the lack of optical birefringence and the reduction in the ratio of the ν_4 to ν_2 IR absorption peaks [38] (figure 1.4) from the ratio observed in calcite.

The deposition of transient amorphous phases as a strategy for producing single crystals with complex morphology may have interesting implications for the development of sophisticated materials. Furthermore, this strategy of molding macroscopic elements into any desired morphology and endowing them with the strength and the degree of perfection of a single crystal, but with the reduced brittleness and mechanical properties of a glass, may have interesting implications for the development of sophisticated materials. These are some of the reasons why ACC is attracting attentions recently in the many branches of material researches for example nano-sized functional materials [39], inorganic-organic hybrid materials [40] and thin films [41].

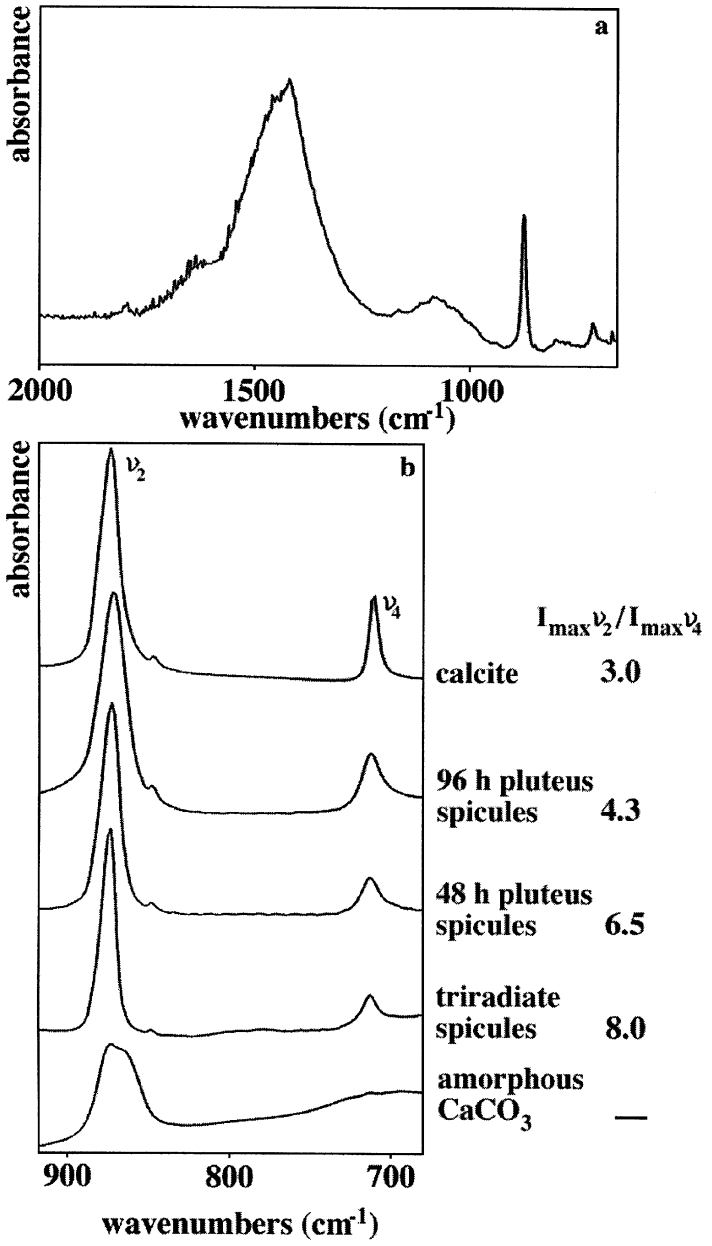

Figure 1.4: (*a*) Infrared spectrum of sea urchin larval spicules. The peak at 1420 cm^{-1} corresponds to the ν_3 absorption band; the broad peak centred at 1086 cm^{-1} belongs to the ν_1 absorption band of amorphous $CaCO_3$; the peaks at 874 and 713 cm^{-1} correspond to 2 and 4 absorption bands of calcite, respectively. (*b*) Portions of the infrared spectra of amorphous $CaCO_3$, three spectra of sea urchin larval spicules at different stages of development and geological calcite, showing the ν_2 and ν_4 absorptions. The ratios of the maximal intensities of the ν_2 versus the ν_4 absorption bands are presented. [Beniash *et al*., *Proc. R. Soc. Lond. B*, 264 (1997)]

1.4 Role of H_2O, Mg, Proteins and Macromolecules on Biomineralization and ACC

Research on biogenic amorphous calcium carbonate clearly suggests that it can contain one or more impurities like water molecules, Mg ions, several proteins and macromolecules. The presence of these molecules and ions definitely has some role in the formation and stabilization of ACC though their exact roles still remain unknown.

NMR results [42] indicate that most of the hydrogen in ACC is present as structural water molecules and not from hydrogencarbonate as suspected earlier. Though generally H_2O content in ACC is very small ($\sim$ 2-3 wt.%) there is evidence [43] that in some cases biogenic ACC can contain up to $\sim$ 15 wt.% of H_2O, e.g. the spicules of pyura pachydermatina (sea tulip). NMR spectroscopy of synthetic ACC reveals [44] that it contains $\sim$ 0.5 mol% of structural water per calcium carbonate unit.

The water content in ACC actually changes its energetic stability [14]. The stable and metastable forms are hydrated whereas the transient forms are not. Study on sea urchin larval spicules inferred [35] that in the transformation process from amorphous calcium carbonate to single crystal phase, the first phase formed is hydrated metastable ACC and the second phase is anhydrous unstable ACC. X-ray absorption spectroscopy (XAS) experiments confirm that the $CaCO_3$ formed in the native cystoliths from Ficus retusa are amorphous and on moistening with water, the mineral part of cystoliths undergoes transformation from amorphous calcium carbonate to crystalline calcite [25].

Magnesium is a key component used by many organisms in biomineralization. Mg is an essential ion in biology, used by all living organisms in many metabolic cycles, including respiration and photosynthesis. In todays sea water, Mg is approximately five times more abundant than Ca. Despite this, of the 70 or so known biogenic minerals, only five have Mg as a major component. Mg is, however, a common additive in carbonate and phosphate biominerals. Specifically, in calcite, the Mg concentrations

can vary from essentially 0 mol% to up to 30 mol% and in some exceptional cases above 40 mol%. Good examples are: mollusk shells that possess near-zero levels of Mg, whereas certain calcareous skeletons of algae and echinoderms contain up to 30 mol% [37] and there is up to 50 mol% in the specialized teeth of sea urchins [45]. The origins of these high Mg levels have been elusive because calcites grown in the laboratory rarely contain $\sim$10-12 mol% Mg [46]. There is growing evidence that one role of Mg in ACC is to stabilize an otherwise unstable amorphous phase. Though the exact way in which this stabilization is achieved is unknown, in vitro experiments show that Mg can significantly alter calcite growth and contribute to the stabilization of ACC [37, 47]. The functionality of Mg in biogenic ACC also depends on the chemistry of the existing local biomolecules. For example, carbonates formed from ACC in the absence of macromolecules contained up to 21 mol% Mg, but Mg contents were increased up to 34 mol% when proteinaceous extracts from coralline algae and acidic polymers were present [36]. Similar Mg-promoting effects are reported in studies of calcification that use polyelectrolytes (polyacrylic acid and polyaspartic acid) to induce carbonate crystallization through an ACC intermediate [48]. In vivo studies of calcification in foraminifera also note the probable role of biomolecules, specifically those in the organic matrix, in modulating species-specific levels of Mg incorporation through ion-specific interactions with Mg versus Ca ions [49]. These studies suggest the possibility that bio-molecular chemistry has a systematic and potentially predictable control on Mg content.

Though the stabilization mechanisms of ACC by Mg ions are not properly understood, some recent research shed light on this topic. Dove *et. al.* [50] found that the Mg-enriching effect in ACC follows a systematic relationship that correlates with the ability of carboxyl groups to interact with calcium relative to magnesium, which suggests that biomolecules influence the formation of amorphous metal carbonate ion-pair clusters. They showed that the electrostatic potential about carboxylated molecules can

greatly increase Mg content to levels that are comparable to the compositions of high magnesium calcites and some dolomites. In another recent study Addadi *et. al.* [51] investigated the influence of chemical environment around magnesium in biogenic and synthetic ACCs using Mg K-edge X-ray absorption spectroscopy. They showed that the introduction of Mg ions in ACC system helps compactification of the host mineral $CaCO_3$ structure around magnesium by reducing cation-anion (Mg-O) bond length, which might be an important factor in subsequent crystallization of ACC.

Apart from H_2O and Mg, it is widely known that macromolecules, such as proteins, can control the nucleation and growth of inorganic solids in biomineralizing organisms. However, what is not known are the complementary molecular interactions, organization, and rearrangements that occur when proteins interact with inorganic solids during the formation of biominerals. The organic-mineral interface is expected to be the site for these phenomena, and is therefore extraordinarily interesting to investigate. Recent analysis of X-ray absorption near edge spectra from calcium carbonate crystals grown in the presence of three mollusk nacre-associated polypeptides (AP7N, AP24N, n16N) and a sea urchin spicule matrix protein (LSM34) by Gilbert *et. al.*[52] showed the reordering of amino acid side chains in the mineral-associated polypeptides and carboxylate binding. Another spectromicroscopy study [53] clearly shows Asp2 peptide permanently disrupts the short-range order in the calcite + Asp2 biomineral composite. Several other studies suggest that the formation and stability of biogenic ACC is regulated by proteins and other macromolecules [54], though the detailed chemistry and structure of these macromolecules vary over the course of mineralization [55]. For example, the ACC of crustaceans contains proteins that have unusually high proportions of glutamate and glutamine residues [56], whereas corals and mollusks contain up to 35% aspartate [55].

1.5 ACC as Nano Particles

The formation of ACC is a matter of active research as the classical nucleation theory fails to explain it [33]. Thanks to current research [14, 44, 57] on the structure of ACC using sophisticated experimental techniques like NMR, XAS, IR spectroscopy, a general consensus is emerging, though still premature, that ACC might be composed of nano-particles. Pair distribution function analysis by Michel *et. al.* [38] on high-energy (100 keV) X-ray diffraction data from synthetic ACC demonstrated a short-range and limited intermediate-range ($\sim$ 10 $\mathring{A}$ – 12 $\mathring{A}$) order but found no structural coherence beyond $\sim$15 $\mathring{A}$. Using cryogenic transmission electron microscopy, Pouget *et. al.* [33] observed that calcium carbonate starts with the formation of prenucleation clusters of dimension of $\sim 6\,\mathring{A} - 11\,\mathring{A}$, which then nucleates to ACC nano-particles of size $\sim$30 nm and finally stabilizes as a single crystal. The shape of these nano-structures is known to be spherical [58]. Along with experiments some limited theoretical study has also been performed. For example, based on equilibrium thermodynamics, Gebauer *et. al.* [59] demonstrated qualitatively the formation of stable $\sim$2 nm clusters prior to nucleation. Furthermore, a recent MD simulation [60], starting from 8 small calcite nanoparticles ($\sim$1.6 nm) placed 1.7 nm apart, showed that these nanoparticles agglomerate with no preferred orientation to from an amorphous calcium carbonate.

1.6 Amorphous Materials and Disorder

Amorphous minerals such as silica, calcium phosphates, calcium and magnesium pyrophosphates and calcium carbonates are widespread in biology [61]. The study of amorphous biominerals has received less attention than their crystalline counterparts largely because of the inherent difficulties in the characterization of their structure and composition. They have a variable stoichiometry and because they have no long-range

order, they cannot be studied by X-ray or electron diffraction techniques (in the sense that there are no precise diffraction features like crystalline materials).

There exist only a few theoretical techniques to model amorphous materials, though they were only tested for covalent solids [62] e.g. a-Si, a-Ge, silica [63]. In general their structure can be considered as a continuous random network [64] of basic units containing short-range order which can be studied by X-ray spectroscopy. Continuous random-network structures preserve local order, but bond-length and bond-angles are somewhat distorted. In their famous work in 1985 Wooten et. al. developed the WWW algorithm [62] which generates realistic random-network with periodic boundary condition to explain the 1-D radial distribution function of covalent materials. This algorithm is still pretty much in use [63] today with a slight modification [65] to model glass like amorphous materials. Despite their success on glass like covalent materials, these kinds of algorithms were never used to model ionic minerals like amorphous $CaCO_3$.

In their recent work Rez and Blackwell [66] explained the Ca L-edge spectra of amorphous $CaCO_3$ by modeling ACC as a distorted lattice of calcite crystal. They showed that distorting the coordination octahedron formed by O atoms around Ca ions lowers the symmetry of the system, which can explain the shift of Ca L lines of ACC from calcite crystal. However, they could not address aragonite, a polymorph of $CaCO_3$, very well because of its very low symmetry compared to calcite.

1.7 Our Approach

The formation of ACC and its subsequent transformation mechanisms to the stable crystalline phases are still very poorly understood. Furthermore, we still do not have clear understanding of its atomistic structure, shape and size. Researches showed that metastable ACC generally transforms into stable crystalline calcite or in some cases to aragonite in an environment rich in Mg, proteins, peptides and often the transformation

goes through a hydrated phase. Regarding the structure, recent studies indicate that ACC might be composed of nano-crystallites of size less than $\sim$15 $\mathring{A}$.

In our current research we are trying to understand the atomistic structure of ACC and the mechanisms by which these structures can be developed from perfect calcite or aragonite crystals. Powder diffraction method will be used to assess the amorphousness of the structures. The roadmap to achieve the goal is the following: Impurities like Mg, H_2O will be introduced in a perfect crystal of calcite/aragonite and the strained structures will be relaxed using the VASP density functional software package. After relaxing we shall extract the distortions in the form of cation-cation bond length and, bond angle distributions from the relaxed structures. Using these distortion distributions we will develop realistic-size ACC structures using a multi-scale modeling scheme. The ACC structures then would be fed to an indigenous diffraction code developed by us, to generate its powder diffraction line profile. The quality of this diffraction line profile will indicate how amorphized the perfect crystal has become and subsequently conclude whether the mechanism of introduction of impurities can produce ACC from the diffraction standpoint. Next we will calculate diffraction profiles from crystals of finite nano size to see whether nano-crystallites as discussed in the literature could give diffraction profiles that appear to come from an amorphous materials. Finally we will compare the theoretical diffraction profile with a transmission electron microscopy (TEM) diffraction measurement we performed on one of our samples, though it should be mentioned that a more systematic investigation is required for better comparison.

Chapter 2

ELECTRONIC STRUCTURE CALCULATION

In our work (Result section) we used density functional theory (DFT) software Vienna ab-initio simulation package (VASP) to relax the atom positions in calcite and aragonite supercells. In this chapter we give a brief review of the theory behind this software package. Because DFT evolved in the process of many years of research on quantum many body/electronic structure calculations, we also briefly review some of those relevant topics here as a background for DFT.

2.1 Quantum Many-Body Hamiltonian

In quantum mechanics one of the main quantities of interest is the wavefunction of a system in its current state. To get the wavefunction we need to solve the Schrödinger equation

$$\widehat{H}\Psi(\{\mathbf{r}\}_i,t) = i\hbar\frac{\partial}{\partial t}\Psi(\{\mathbf{r}\}_i,t) \tag{2.1}$$

where $\widehat{H}$ is the N particle (body) Hamiltonian interacting with each other via Coulomb interaction, and $\Psi(\{\mathbf{r}\}_i,t)$ is the abbreviated form of the N-body wave function $\psi(r_1,r_2,,r_N,t)$. r_i is the position vector of the i^{th} particle. The Hamiltonian [67] $\hat{H}$ for such a system can explicitly be written as following:

$$\widehat{H} = -\frac{\hbar^2}{2m_e}\sum_{i=1}^{N}\nabla_i^2 - \sum_{i,I=1}^{N}\frac{Z_I e^2}{|\mathbf{r}_i-\mathbf{R}_i|} + \frac{1}{2}\sum_{i\neq j}\frac{e^2}{|\mathbf{r}_i-\mathbf{r}_j|} - \frac{\hbar^2}{2M_I}\sum_{I=1}^{N}\nabla_I^2 + \frac{1}{2}\sum_{I\neq J}\frac{Z_I Z_J e^2}{|\mathbf{R}_I-\mathbf{R}_J|} \tag{2.2}$$

where the electronic and nuclear terms are denoted by lower case and upper case subscripts respectively. In equation (2.2) 1^{st} and 4^{th} terms are the electronic and nuclear kinetic energy (K.E.) of the system, the 3^{rd} and 5^{th} terms are the electron-electron and

nucleus-nucleus interaction terms and 2^{nd} term is the electron-nucleus interaction term. Later in this chapter we will use a short hand notations for all the above terms instead of their explicit form, in equation (2.2) sequentially these are $\hat{T}, \hat{V}_{ext}, \hat{V}_{int}, \hat{T}_I$ and $\hat{E}_{II}$. Adopting Hartree atomic units i.e. taking $\hbar = m_e = e = 4\pi/\varepsilon_0$=1, we can write the many-body Hamiltonian in equation (2.2) as

$$\widehat{H} = \widehat{T} + \widehat{V}_{ext} + \widehat{V}_{int} + \widehat{T}_I + E_{II} \tag{2.3}$$

Where, $\widehat{T} = \sum_i -\frac{1}{2}\nabla_i^2$, $\widehat{V}_{int} = \frac{1}{2}\sum_{i \neq j} \frac{1}{|\mathbf{r}_i - \mathbf{r}_j|}$, etc.

It is important to realize that most physical problems of interest consist of a number of interacting electrons and ions. For a realistic system the total number of particles N is usually so large that an exact solution is almost impossible to find, even with the best of today's computing facility. Generally approximations are sought to reduce the complexity to a tractable level. Once the equations are solved, a large number of properties may be calculated from the wavefunction. Errors or approximations made in obtaining the wavefunction will be manifested in any property derived from the wavefunction. Where high accuracy is required, considerable attention must be paid to the derivation of the wavefunction and any approximations made.

2.2 Born-Oppenheimer Approximation

In a system of interacting electrons and nuclei there will be very little momentum transfer between the two types of particles due to their huge difference in masses (m_e:$M_I \sim$ 1:10,000). Hence in equation 2.2 we can see that the terms containing $1/M_I$ namely T_I is much smaller compared to the others. Ignoring the nuclear K.E, the Hamiltonian in equation 2.2 or 2.3 then becomes,

$$\widehat{H} = \widehat{T} + \widehat{V}_{ext} + \widehat{V}_{int} + E_{II} \tag{2.4}$$

Physically this means that the time-scale of nuclear motion is much greater than the electronic motion due to their greater mass differences but similar magnitude of Coulomb forces, hence one can therefore consider the electrons to relax to a ground-state given by the Hamiltonian (equation 2.4) with the nuclei at fixed locations. This separation of the electronic and nuclear motion (degrees of freedom) is known as the Born-Oppenheimer or adiabatic approximation [68]. It is important to note that this approximation does not limit us to the systems with only fixed ions, because in principle once the electronic configuration is known, the nuclear degrees of freedom could also be determined, giving rise to nuclear motion. This is an excellent approximation for many purposes, e.g. the calculation of vibration modes in most solids [69, 70]. However, even with this approximation, the resultant Hamiltonian in equation 2.4 remains very difficult to solve mainly because of the correlated electronic term $\widehat{V}_{int}$. Because of that, no analytic solutions exist to date for general systems with more than one electron.

2.3 Hartree Theory

In 1928 D. R. Hartree proposed [71] a 'mean-field' or 'non-interacting' theory to handle the correlated electronic motion described by the Hamiltonian in equation 2.4. He suggested that electrons inside a material move independently of other electrons, under the influence of an effective potential $\widehat{V}^{\sigma}_{eff}$ created by all the other electrons and nuclei. This $\widehat{V}^{\sigma}_{eff}$ is spin-dependent because of the fact that electrons, being fermions, have to obey the Pauli exclusion principle. Hence the Hartree equation for the electrons can be written as:

$$\widehat{H}_{eff}\psi_i^{\sigma}(\mathbf{r}) = \left[-\frac{\hbar^2}{2m_e}\nabla^2 + V^{\sigma}_{eff}(\mathbf{r})\right]\psi_i^{\sigma}(\mathbf{r}) = \varepsilon_i^{\sigma}(\mathbf{r})\,\psi_i^{\sigma}(\mathbf{r}). \tag{2.5}$$

Not surprisingly the main problem with Hartree theory is that it misses the effect of exchange and correlation of in electronic motion. Hartree's $\widehat{V}^{\sigma}_{eff}$ also contains an unphysical self-energy term for an electron under consideration. Though not very successful

this non-interacting approach was the pioneering work in the field of electronic structure calculation as it laid the ground work for the remarkably successful DFT which will be discussed later in this chapter.

2.4 Hartree-Fock Theory

In 1930 V. Fock introduced [72] his 'Hartree-Fock' theory which was a big improvement over Hartree theory. Unlike Hartree theory, Hartree-Fock tries to minimize the total energy of the full interacting Hamiltonian 2.4, starting from a properly anti-symmetrized wavefunction (Slater determinant) Φ for N electrons,

$$\Phi = \frac{1}{(N!)^{1/2}} \begin{vmatrix} \phi_1(\mathbf{r}_1,\sigma_1)\,\phi_1(\mathbf{r}_2,\sigma_2)\ldots\phi_1(\mathbf{r}_N,\sigma_N) \\ \phi_2(\mathbf{r}_1,\sigma_1)\,\phi_2(\mathbf{r}_2,\sigma_2)\cdots\phi_2(\mathbf{r}_N,\sigma_N) \\ \vdots \qquad\qquad \vdots \qquad\qquad \vdots \\ \phi_N(\mathbf{r}_1,\sigma_1)\,\phi_N(\mathbf{r}_2,\sigma_2)\cdots\phi_N(\mathbf{r}_N,\sigma_N) \end{vmatrix} \tag{2.6}$$

where $\phi_i(r_j,\sigma_j)$ are the single particle 'spin-orbitals' each of which is the product of a function of the position $\Psi_i^{\sigma}(r_j)$ and a function if the spin variable $\chi_i(\sigma_j)$. Using this wave function the expectation value of the Hamiltonain 2.4 become

$$\begin{aligned} \langle\Phi|\,\widehat{H}\,|\Phi\rangle &= \sum_{i,\sigma}\int d\mathbf{r}\,\psi_i^{\sigma*}(\mathbf{r})\left[-\frac{1}{2}\nabla^2 + V_{ext}(\mathbf{r})\right]\psi_i^{\sigma}(\mathbf{r}) \\ &+\frac{1}{2}\sum_{i,j,\sigma_i,\sigma_j}\int d\mathbf{r}d\mathbf{r}'\,\psi_i^{\sigma_i*}(\mathbf{r})\,\psi_j^{\sigma_j*}(\mathbf{r}')\,\frac{1}{|\mathbf{r}-\mathbf{r}'|}\,\psi_i^{\sigma_i}(\mathbf{r})\,\psi_j^{\sigma_j}(\mathbf{r}') \\ &-\frac{1}{2}\sum_{i,j,\sigma}\int d\mathbf{r}d\mathbf{r}'\,\psi_i^{\sigma*}(\mathbf{r})\,\psi_j^{\sigma*}(\mathbf{r}')\,\frac{1}{|\mathbf{r}-\mathbf{r}'|}\,\psi_j^{\sigma}(\mathbf{r})\,\psi_i^{\sigma}(\mathbf{r}')\,. \end{aligned} \tag{2.7}$$

The first term in equation 2.7 groups together the single-body expectation values. The second and third terms are called the direct (or Hartree) and exchange interactions respectively. The '$i=j$' term or the "self-interaction", which was a problem in Hartree theory (Section 2.3), cancels in the direct and exchange terms. The exchange term,

which acts only between electrons with the same spin, is a completely new concept which results from the inclusion of the Pauli principle and the assumed determinant form of the wavefunction (equation 2.6). Due to the exchange term the like-spin electrons can avoid each other in Hartree-Fock theory. Each electron of a given spin is consequently surrounded by an "exchange hole", a small volume around the electron which like-spin electrons avoid.

In spite of some success [73, 74, 75, 76, 77] and the fact that it is still in use [78, 79], Hartree-Fock theory, by assuming a single-determinant form for the wavefunction, neglects "correlation" between electrons. Here the electrons are subject to an average non-local potential arising from the other electrons, which can lead to a poor description of the electronic structure. Although qualitatively correct in many materials and compounds, except in the case of strongly correlated materials such as NiO, Hartree-Fock theory is insufficiently accurate to make accurate quantitative predictions. Also unlike the case for the independent particle Hartree-theory, the Hartree-Fock integrals in equation 2.7 can only be solved directly in special cases e.g. spherically symmetric atoms and the homogeneous electron gas. In general these are very difficult to compute and the difficulty grows with the size and accuracy since one must evaluate N^4 integrals [80].

2.5 Density Functional Theory (DFT)

DFT is a powerful, formally exact theory [81, 82, 83] for ground state electronic structure calculations. Unlike Hartree-Fock theory it is a non-interacting theory and does not yield a correlated *N*-body wavefunction. The Kohn-Sham [84] formulation of DFT is an independent-particle theory and shares many similarities with Hartree theory. DFT has come to prominence over the last decade as a method potentially capable of very accurate results at low cost. In practice, approximations are required to implement the theory for real electronic systems. We shall present this section in few subsections,

namely the Hohenberg-Kohn theorem; the Kohn-Sham equations; the local density approximation and the generalized-gradient approximations.

2.5.1 The Hohenberg-Kohn Theorem

The approach of Hohenberg and Kohn is to formulate DFT as an exact theory of many-body interacting systems in an external potential V_{ext}, at least in principle. The statement of Hohenberg-Kohn theorem [85] is the following,

If a system of interacting particles moves in an external potential V_{ext} then the ground state particle density n_0(r) minimizes the energy functional

$$E[n] = F[n] + \int n(\mathbf{r}) V_{ext}(\mathbf{r}) d\mathbf{r} \tag{2.8}$$

where, F[n] is a universal functional of n and the minimum value of E[n] is the ground state energy E_0 of the system. A simple proof of this theorem due to Levy [86] is given below.

Let us define an operator,

$$\widehat{F} = \sum_i -\frac{1}{2}\nabla_i^2 + \frac{1}{2}\sum_{i\neq j}\frac{1}{|\mathbf{r}_i - \mathbf{r}_j|} \tag{2.9}$$

The expectation value of $\widehat{F}$ in the basis of all the trial wavefunction ψ which produces the density n(r) can be written as,

$$F[n(\mathbf{r})] = \langle\Psi|\widehat{F}|\Psi\rangle \tag{2.10}$$

The expectation value of the many-body Hamiltonian in equation 2.4 with respect to those Ψ is nothing but the total energy of the system which now can be written as,

$$E[n(\mathbf{r})] = F[n(\mathbf{r})] + \int n(\mathbf{r}) V_{ext}(\mathbf{r})\, d\mathbf{r} + E_{II} \tag{2.11}$$

Hence using the variation principle we can easily prove that the lower bound of $E[n(\mathrm{r})]$ is the ground state energy $E_0 = \langle \Psi_0 | H | \Psi_0 \rangle$, where the ground state wavefunction ψ_0 yields the ground state density n_0, or mathematically $E[n(\mathbf{r})] = E_0$.

This completes the proof of Hohenberg-Kohn theorem. Though in principle this theorem solves for the many-body ground state properties (i.e. E_0 and n_0) in practice it is of little use because the proper functional $F[n(\mathbf{r})]$ could never be found. Hence in addition we need the Kohn-Sham theory, which will be discussed next, before it could really be used.

2.5.2 The Kohn-Sham Ansatz

The Kohn-Sham approach [84] is to replace the difficult interacting many-body system obeying the Hamiltonian 2.4 with a different auxiliary system that can be solved more easily. Because in the previous section we saw that the main quantity of importance is the ground state particle density n_0, the ansatz of Kohn-Sham assumes that the n_0 of the original interacting system is equal to that of some chosen non-interacting system. This leads to a set of exactly soluble independent-particle equations for the non-interacting-system, with all the difficult many-body terms incorporated into an "exchange-correlation" functional of density. By solving the equations one finds the ground state density and energy of the original interacting system with the accuracy limited only by the approximations in the exchange-correlation functional. E.g. in Kohn-Sham ansatz the energy functional can be written as,

$$E[n(\mathbf{r})] = T_s[n(\mathbf{r})] + \frac{1}{2}\int \frac{n(\mathbf{r})\, n(\mathbf{r}')}{|\mathbf{r}-\mathbf{r}'|} d\mathbf{r} d\mathbf{r}' + \int n(\mathbf{r})\, V_{ext}(\mathbf{r})\, d\mathbf{r} + E_{XC}[n(\mathbf{r})] + E_{II} \tag{2.12}$$

Where T_S[n(r)] is the kinetic energy of a non-interacting system (not that of the real interacting system) and can be expressed by,

$$T_s[n(\mathbf{r})] = -\frac{1}{2}\sum_{i=1}^{N} \psi_i^*(\mathbf{r})\nabla^2\psi_i(\mathbf{r})\,d\mathbf{r} \tag{2.13}$$

Equation 2.12 also defines the exchange-correlation energy function E_{XC}[n(r)] which is nothing but all the many-body contribution to the total energy. To solve for the energy of this non-interacting system we want to solve a Schrdinger like equation. Hence if we define an effective potential V_{eff} (r) as,

$$V_{eff}(\mathbf{r}) = V_{ext}(\mathbf{r}) + \int \frac{n(\mathbf{r}')}{|\mathbf{r}-\mathbf{r}'|}d\mathbf{r}' + V_{XC}(\mathbf{r}) \tag{2.14}$$

where the exchange-correlation potential is given by,

$$V_{XC} = \frac{\delta E_{XC}[n(r)]}{\delta n(r)} \tag{2.15}$$

Then to find the ground state energy E_0 and particle density n_0 we need to solve the following Schrdinger like equation.

$$\left(-\frac{1}{2}\nabla_i^2 + V_{eff}(\mathbf{r})\right)\psi_i(\mathbf{r}) = E\,\psi_i(\mathbf{r}) \tag{2.16}$$

Because the trial non-interacting particle solutions are not exact, the above equation 2.16 has to be solved self-consistently with $n(r) = \sum_{i=1}^{N} |\psi_i(r)|^2$ for the results to be meaningful. Unfortunately, the form of E_{XC} is in general unknown and its exact value has been calculated for only a few very simple systems [87] such as a homogeneous electron gas. In electronic structure calculations E_{XC} is most commonly approximated within the local density approximation (LDA) or generalised-gradient approximation (GGA). In our calculation we use LDA , hence we shall mostly discuss the LDA in the next section, though GGA will be touched upon in the context of improvement to LDA.

2.5.3 The Local Density Approximation

In the local density approximation (LDA), the value of $E_{XC}[n(\mathrm{r})]$ is approximated by the exchange-correlation energy of an electron in an homogeneous electron gas of the same density , i.e.

$$E_{XC}^{LDA}[n(\mathbf{r})] = \int \varepsilon_{XC}[n(\mathbf{r})]\, n[n(\mathbf{r})]\, d\mathbf{r} \tag{2.17}$$

where, ε_{XC} is the energy per electron at point r that depends only on electron density n(r). The most accurate data can be obtained from Quantum Monte Carlo (QMC) calculations [88]. The LDA generally gives good results for systems with slowly varying charge densities. But not surprisingly, it has a tendency to favor more homogeneous systems and over-binds molecules and solids. In weakly bonded systems these errors are exaggerated and bond lengths are too short. In systems where the LDA works well, often those mostly consisting of *sp* bonds, calculated geometries closely resemble the experimentally determined structures and bond lengths and angles are accurate to within a few percent. Quantities such as the dielectric and piezoelectric constant are approximately 10% large. Despite the remarkable success of the LDA, which was again being confirmed by QMC calculations [89, 90], it is well-known that LDA does not work for strongly-correlated system e.g. transition-metal oxide i.e. XO (where, X = Fe, Mn, Ni) which are all Mott insulators which LDA predicts to be either semiconductors or metals [91]. This result is not surprising because the independent particle picture, which is at the heart of LDA, breaks down completely for these strongly interacting systems. An obvious approach to improve LDA is to include a gradient correction, by making E_{XC} a function of density and its gradient, i.e.

$$E_{XC}^{GGA}[n(\mathbf{r})] = \int \varepsilon_{XC}[n(\mathbf{r})]\, n(\mathbf{r})\, d\mathbf{r} + \int F_{XC}[n(\mathbf{r}), |\nabla n(\mathbf{r})|]\, d\mathbf{r} \tag{2.18}$$

where the correction F_{XC} is chosen to satisfy one or several known limits of E_{XC}.

2.5.4 Working principle of VASP

VASP is a versatile DFT software which uses plane-waves as the trial wavefunctions. Pseudo-potentials are used to smooth out the effect of core-electrons. It can use either LDA and GGA. For our relaxation of atomic positions in supercells we use a plane wave basis in LDA mode. The initial atomic coordinates and supercell information is stored in an ASCII file called POSCAR which is given as one of the inputs to VASP. Below, the working principle of VASP is shown in figure 2.1 in the form of a flowchart.

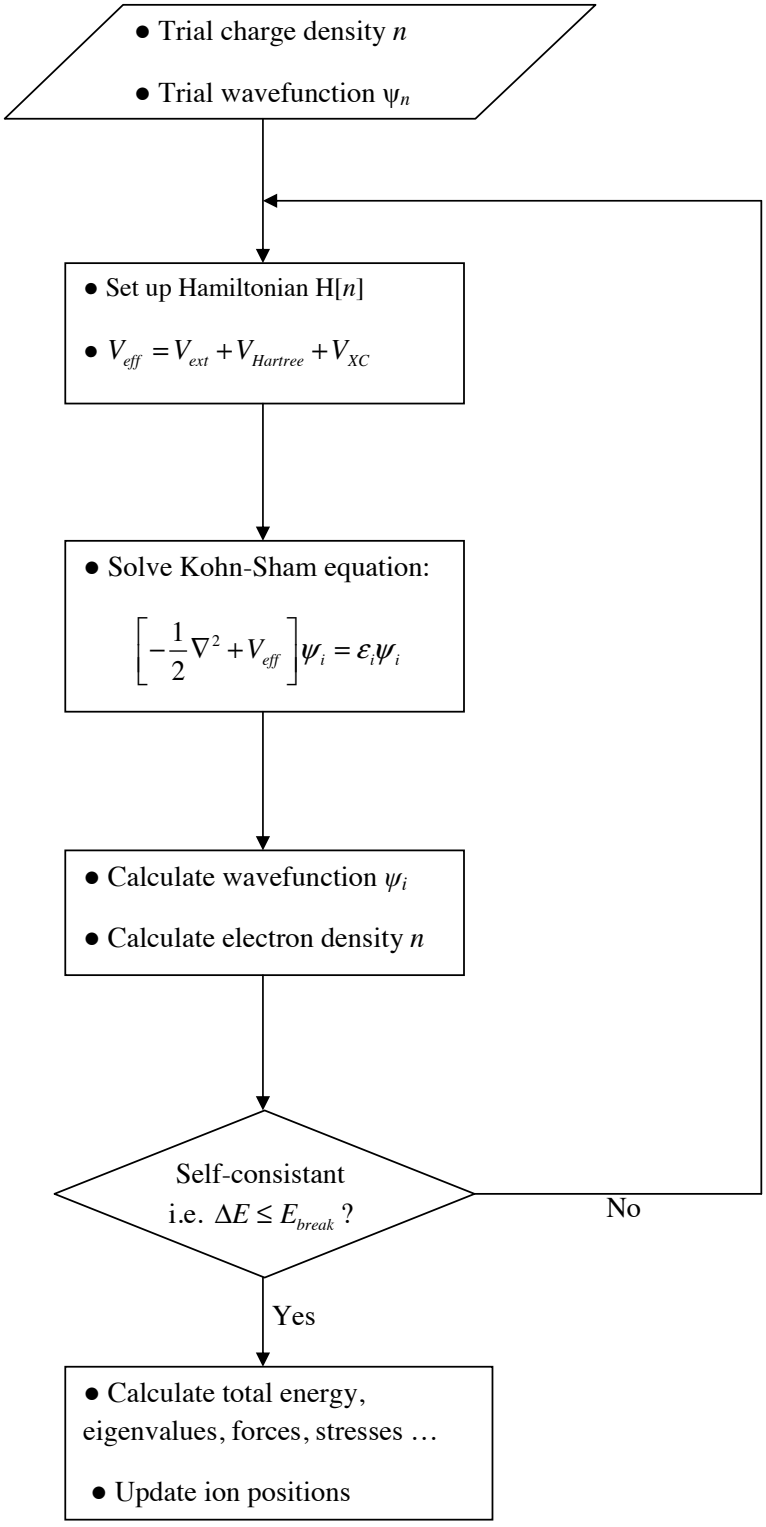

Figure 2.1: Flowchart of the working principle of DFT-code VASP

Chapter 3

THEORY OF DIFFRACTION AND CODE ARCHITECTURE

In this chapter we shall review some important topics of diffraction theory that were used in developing our indigenous diffraction code to analyze amorphous calcium carbonate (ACC). Then we shall present the code in the form of a flow chart. The whole code can be found in appendix A.

3.1 Reciprocal Lattice

The diffraction pattern of any material is the map of its Fourier space also known as reciprocal space because it has the dimension of reciprocal of length. Geometrically a crystal is a large three dimensional array of lattice points. If we denote the primitive vectors of the crystal lattice by **a**, **b** and **c** then any crystal lattice vector **R** can be represented by:

$$\mathbf{R} = x\mathbf{a} + y\mathbf{b} + z\mathbf{c} \tag{3.1}$$

Where x, y and z are the respective components of lattice vector **R**. The axis vectors **A**, **B** and **C** of the reciprocal lattice corresponding to the above crystal lattice can be constructed by:

$$\mathbf{A}=2\pi\frac{\mathbf{b}\times\mathbf{c}}{\mathbf{a}\cdot\mathbf{b}\times\mathbf{c}};\mathbf{B}=2\pi\frac{\mathbf{c}\times\mathbf{a}}{\mathbf{a}\cdot\mathbf{b}\times\mathbf{c}};\mathbf{C}=2\pi\frac{\mathbf{a}\times\mathbf{b}}{\mathbf{a}\cdot\mathbf{b}\times\mathbf{c}}\cdot \tag{3.2}$$

Hence, any lattice point in the reciprocal space can be given by a reciprocal lattice vector **G**.

$$\mathbf{G}=h\mathbf{A}+k\mathbf{B}+l\mathbf{C} \tag{3.3}$$

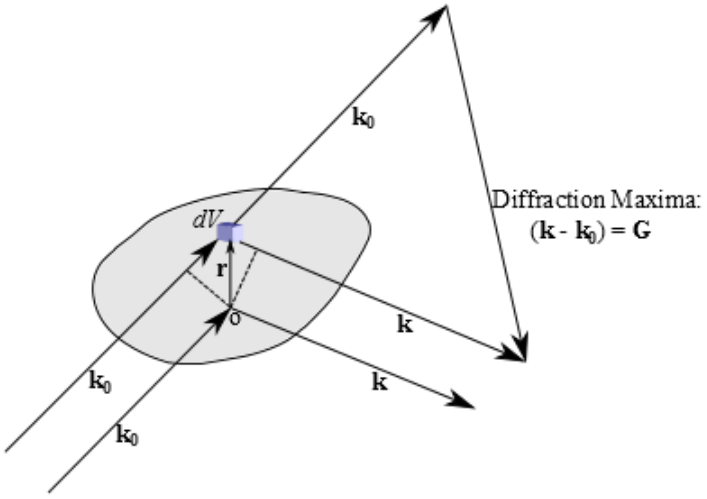

Figure 3.1: Schematics of elastic scattering from a sample

In other words if there is a set of parallel planes denoted by the Miller indices $\{h,k,l\}$ then **G** corresponds to the normal to those planes as shown in figure 3.2. If the planes are separated from each other by a distance d then it can be shown [92, 93] that,

$$d_{\{h,k,l\}} = \frac{2\pi}{|\mathbf{G}|} \tag{3.4}$$

3.2 Diffraction Condition Bragg Equation

Crystal diffraction is nothing but a phenomenon of elastic scattering of light or particles from the atoms making up the crystal lattice. Figure (3.1) shows a schematic diagram of such an event. An incident plane wave $(e^{-i\mathbf{k_0}\cdot r})$ with wave vector $\mathbf{k_0}$ scatters off a small portion of the specimen dV. The scattered beam $(e^{-i\mathbf{k}\cdot r})$ has a wave-vector $\mathbf{k}$. If the electron density at dV is $n(\mathbf{r})$, where $\mathbf{r}$ is measured from an arbitrary origin O, the total amplitude of the scattered beam or the scattering amplitude [92, 93] is:

$$f_{\mathbf{k}} = \int dV n(\mathbf{r}) e^{-i(\mathbf{k}-\mathbf{k}_0)\cdot\mathbf{r}} = \int dV n(\mathbf{r}) e^{-i\Delta\mathbf{k}\cdot\mathbf{r}} \tag{3.5}$$

Where, $\Delta\mathbf{k} = (\mathbf{k} - \mathbf{k_0})$. Introducing the Fourier components of $n(\mathbf{r})$ in terms of reciprocal lattice vectors $\mathbf{G}$ in equation 3.5 we obtain,

$$f_k = \sum_{\mathbf{G}} \int dV n_{\mathbf{G}} e^{-i(\mathbf{G}-\Delta\mathbf{k})\cdot\mathbf{r}} \tag{3.6}$$

It is easy to show[92, 95] that in equation 3.6 f_k is maximum when $\Delta\mathbf{k} = \mathbf{G}$ and it becomes negligible when $\Delta\mathbf{k}$ is far from $\mathbf{G}$. Hence this gives the diffraction condition:

$$\Delta\mathbf{k} = \mathbf{G} \text{ or, } \mathbf{k} = \mathbf{k}_0 + \mathbf{G} \tag{3.7}$$

We can also write the above vector equation 3.7 in scalar form in the following way.

$$(\mathbf{k_0}+\mathbf{G}) \cdot (\mathbf{k_0}+\mathbf{G}) = |\mathbf{k}|^2 \tag{3.8}$$

Since it is an elastic scattering process thus $|k_0| = |k|$. Hence from equation 3.8 we see,

$$2\mathbf{k}_0 \cdot \mathbf{G} = |\mathbf{G}|^2 \tag{3.9}$$

Using equation 3.4 and the fact that $|k_0| = 2\pi/\lambda$ in equation 3.9, we can obtain famous Bragg reflection condition from crystal planes:

$$2d_{\{h,k,l\}} \sin\theta = \lambda \tag{3.10}$$

Where θ is the angle between incident beam and the crystal planes $\{h,k,l\}$ (because $\mathbf{G}$ is normal to the planes, figure 3.2) with the shortest distance between two consecutive planes being $\mathrm{d}_{\{h,k,l\}}$. It is customary to express the diffraction profile as a function of scattering angle 2θ that can easily be obtained from the Bragg condition. For electron diffraction, the wavelength of electrons (e.g in a TEM is $0.025\mathring{A}$ for 200 keV electrons)

is small compared to an interplanar spacing, unlike X-ray diffraction where typical wavelengths are comparable to interplanar spacings. Hence in electron diffraction, all the important Bragg peaks occur at very small Bragg angles ($2\theta < 1^{\circ}$). Since for small Bragg angles $\sin\theta \sim \theta$, we can write, from equation 3.10,

$$2\theta \sim \lambda / d_{\{h,k,l\}} = \frac{\lambda |\mathrm{G}|}{2\pi} \tag{3.11}$$

3.3 Ewald Sphere Construction

The diffraction condition in equation 3.9 and in figure 3.1 can be visualized by a simple geometric construction due to Ewald [96]. The Ewald sphere construction for a two dimensional reciprocal lattice is shown in figure 3.2. Here the wave vectors $\mathbf{k_0}$ and $\mathbf{k}$ corresponds to the incident wave (electron beam) and the scattered wave respectively and the scattering angle is 2θ. To find the connection between Bragg picture and Ewald construction we should notice that θ is the same angle used in Bragg condition i.e. equation 3.10. In figure 3.2 we have shown the Ewald construction. Here a sphere of radius $2\pi/\lambda$, λ being the wave length of the incident wave, drawn about an arbitrary point O that passes through the origin of reciprocal space O$'$. The line connecting the center of the sphere O to the reciprocal space origin O$'$ represents the incident direction. Lines connecting O to other reciprocal lattice points e.g. A, give the direction of corresponding diffracted rays. It should be noticed from figure 3.2 that in the case of diffraction, the scattering vector $(\mathbf{k} - \mathbf{k_0}) = \Delta\mathbf{k}$ is equal to a reciprocal lattice vector $\mathbf{G}$ corresponding to planes $\{h,k,l\}$ with inter-planar separation $\mathrm{d}_{\{h,k,l\}}$. This observation is consistent with the results of the Bragg picture presented in section 3.2. Hence O$'$, which is also taken as the origin of the reciprocal space, would represent the direction of unscattered beam and A would represent the direction of peak reflected (Bragg picture) from the set of $\{h,k,l\}$ planes.

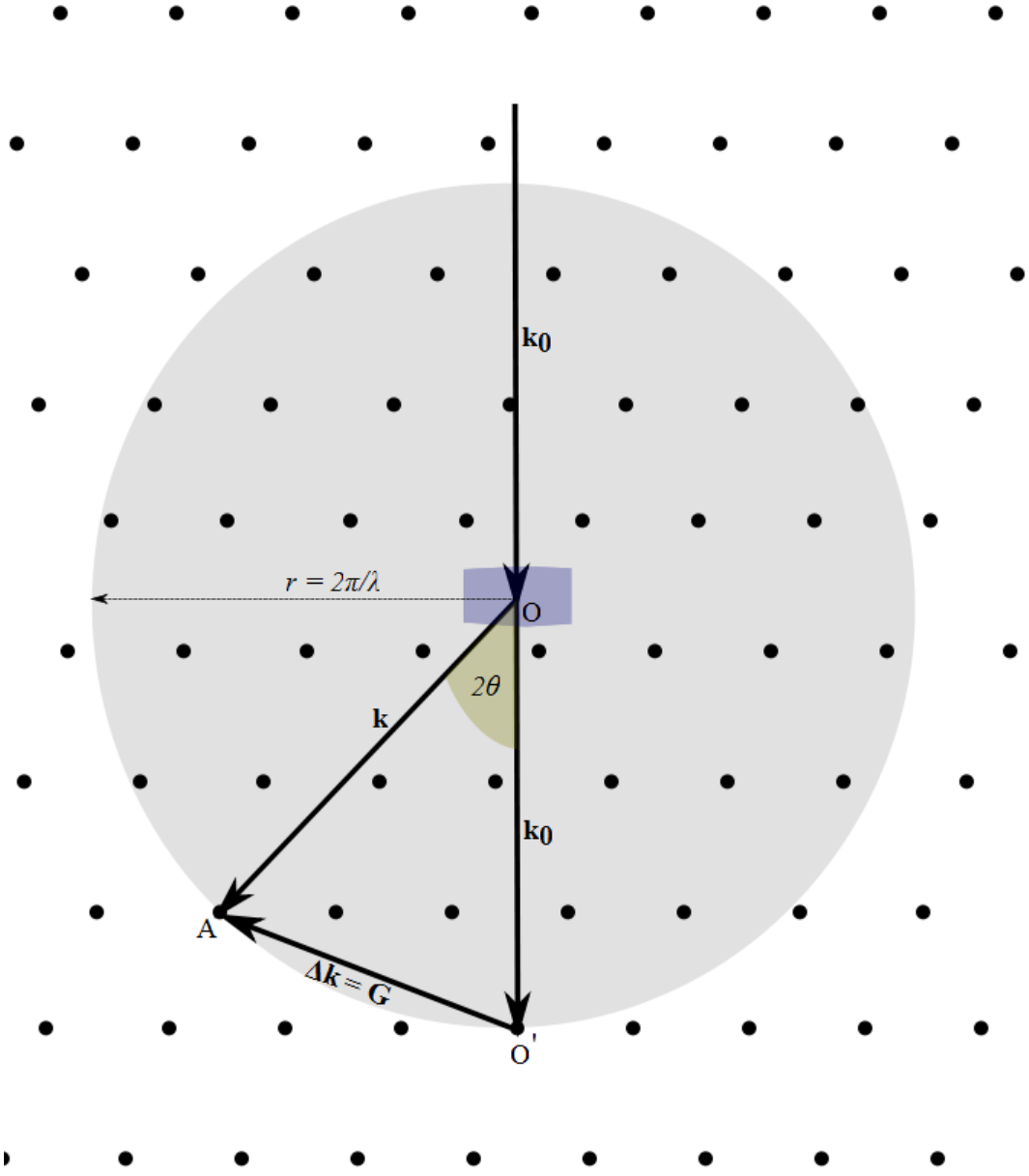

Figure 3.2: Ewald sphere construction of a two dimensional lattice

We are interested in electon diffraction (TEM) where the electron beam has an energy 200 keV and the corresponding wavelength $\lambda = 0.025$ $\mathring{A}$. Hence the radius of the Ewald sphere is large compared to a reciprocal lattice vector. And because we are concerned with small scattering angles ($2\theta \sim 1^\circ$), since all the important Bragg peaks occur in that range, we can approximate the Ewald sphere as a plane through O$'$. It should be noticed from equation (3.11) that $|\mathbf{G}| \sim 5(\mathring{A})^{-1}$ for $2\theta \sim 1^\circ$, which suggests that the maximum length of scattering vector we should be interested is $\sim 5\ (\mathring{A})^{-1}$ about the origin. Hence to determine all the relevant diffraction directions we have to take into account all the appropriate reciprocal-space points (i.e. points that lie near the Ewald sphere surface) which fall within a radius of 5 $(\mathring{A})^{-1}$ about O$'$.

Another important aspect is the broadening of diffraction peaks due to shape transform, the Fourier transform (FT) of the finite crystal. As will be shown in section 3.5 below, reducing the crystal size broadens its diffraction peaks. Hence while sampling the reciprocal lattice points from the Ewald construction we must remember that the reciprocal lattice points are broadened by the finite-crystal shape transform and should sample from a shell of appropriate thickness around the surface of Ewald sphere rather than the lattice points exactly on the surface. To cover the range of crystal sizes we choose 0.8 $(\mathring{A})^{-1}$ as this is equivalent to a length of ~ 4 $\mathring{A}$ in real space, which is around half the size of the smallest crystallite we shall ever use.

3.4 Scattering Factors

In section 3.2, we saw (equation 3.5) that the elastic-scattering or diffracted amplitude from an atom, also called the atomic scattering factor, $f(\mathbf{k})$ can be given by,

$$f_j(\mathbf{G}) = \int dV n_j(\mathbf{r})\, e^{-i\mathbf{G}\cdot\mathbf{r}} \tag{3.12}$$

where the subscript j labels different atomic species in a polyatomic crystal like $CaCO_3$. Hence the total scattering amplitude or the structure factor can be calculated by,

$$F(\mathbf{G}) = \sum_j f_j(\mathbf{G})\, e^{-(x_j \mathrm{G}_x + \mathrm{y}_j \mathrm{G}_y + z_j \mathrm{G}_z)} \tag{3.13}$$

Since intensity is proportional to the square of the amplitude, the total diffracted intensity is simply $\propto |F(G)|^2$ or explicitly,

$$I(\mathbf{G}) = \left| \sum_j f_j(\mathbf{G})\, e^{-i(x_j \mathrm{G}_x + \mathrm{y}_j \mathrm{G}_y + z_j \mathrm{G}_z)} \right|^2 \tag{3.14}$$

which can be trivially rewritten for Bragg reflection from $\{h,k,l\}$ planes as,

$$I_{\{h,k,l\}} = \left| \sum_j f_j(\theta)\, e^{-2\pi i(x_j h + \mathrm{y}_j k + z_j l)} \right|^2 \tag{3.15}$$

In equation 3.14 or 3.15 $\{x_j, y_j, z_j\}$ are the position coordinates of individual atoms in the crystal which we know well. We find the diffraction directions using the Ewald technique discussed in the section 3.3. Hence all that is necessary to calculate the diffracted intensity is the appropriate factors f_j for each species as a function of scattering angle 2θ. Calculating scattering factors for diffraction purposes is a field of research and luckily some studies [96, 97, 98] have been done. The electron scattering factors (f_e) can be obtained by using the Mott formula [99],

$$f_e(s) = \left(\frac{me^2}{2h^2}\right) \left\{ \frac{[Z - f_X(s)]}{s} \right\} \tag{3.16}$$

on the X-ray scattering factors [100] (f_X). The directional or scattering vector dependence of f_e can be obtained by parameterizing it as a sum of several Gaussians [101, 102, 103, 104]. We use the results of Doyle and Turner [96] who used 4 Gaussians

or 8 parameters for each species. Hence for our purpose we can obtain the scattering vector dependence of f_e as,

$$f_e(s) = \sum_{i=1}^{4} a_i e^{-b_i S^2} \tag{3.17}$$

where $s = (sin(\theta)/\lambda)(\mathring{A})^{-1}$. The parameters used in equation 3.17 for the species of interest namely C, O, Ca are given in table (3.1). It should be mentioned that these values of $f_e(s)$ were parameterized [96] up to S = 6.0 $(\mathring{A})^{-1}$ excluding S = 0 and tabulated in table (3.1).

Z	Symbol	a_1	b_1	a_2	b_2	a_3	b_3	a_4	b_4
6	C	0.73	37.00	1.2	11.3	0.46	2.81	0.13	0.35
8	O	0.46	23.78	0.92	7.62	0.47	2.14	0.14	0.30
20	Ca	4.47	99.52	2.97	22.7	1.97	4.20	0.48	0.42

Table 3.1: Parametrized electron scattering factors for C, O, Ca

3.5 Relationship between Diffracted Peak Width and Crystal Size

In the previous section we discussed diffraction from an infinite crystal. In reality all crystals have finite size which is especially important for nano-crystallites, one of our main area of interest. In this section we shall present the effect of finite crystal size on the diffraction pattern. To emulate the finite size we shall assume a simple rectangular aperture in one dimension rather than any complicated one for our argument, as this result holds generally true with slight modification for arbitrary size and shape. Notice that this one-dimension result can easily be generalized for three-dimension rectangular prism geometry by simply taking the product of shape-functions in each direction.

The idea explained above is shown schematically in figure 3.3 where a finite crystal can be viewed as an infinite crystal convoluted with a rectangular aperture which has the same size as the finite crystal. Hence using the convolution theorem we can

evaluate the diffraction pattern from a finite crystal as a product of the FT of infinite crystal and the FT of the rectangular box. The FT of the infinite crystal gives the amplitude at a reciprocal lattice point satisfying the diffraction condition, which was discussed in section 3.3 but it does not give the width of the diffracted peaks. The peak-width which is also called the shape transformation function that can be obtained [105, 106, 107] by taking the FT of finite shape of the crystal (rectangular box in this case). Below we present a brief mathematical treatment to show how the peak width varies as a function of box size.

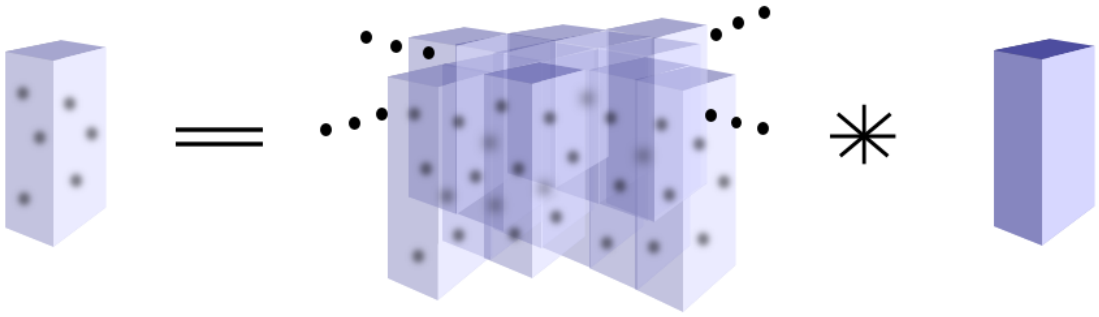

Figure 3.3: The schematic shows a finite crystal is equivalent to the convolution of an infinite crystal with a finite aparture

Diffraction intensity at **G**: $\mathrm{FT}\{\text{inf crystal} * \text{rect box}\}$

$$= \mathrm{FT}\{\text{inf crystal}\} \cdot \mathrm{FT}\{\text{rect box}\} \quad \text{[convolution theorem]}$$

$$= I_0 \delta(k-G) \cdot \mathrm{FT}\left\{\mathrm{rect}\left(\frac{x}{a}\right)\right\} \tag{3.18}$$

Rectangular box of side a:

$$f(x) = \mathrm{rect}\left(\frac{x}{a}\right) = \begin{cases} 1, & |x| < \frac{1}{2}a \\ 0, & |x| > \frac{1}{2}a \end{cases} \tag{3.19}$$

FT of $f(x)$ is:

$$F(k) = \frac{1}{\sqrt{2\pi}} \int_{-\frac{a}{2}}^{\frac{a}{2}} e^{-ikx} dx = \sqrt{\frac{2}{\pi}} \frac{\sin\left(ka/2\right)}{k} \tag{3.20}$$

Diffraction intensity profile is:

$$I \sim I_0 \frac{\sin^2(Ga/2)}{G^2} \tag{3.21}$$

The diffraction peak width is:

$$\Delta G \sim \frac{\pi}{a} \tag{3.22}$$

From equation 3.22 we can see that diffraction peak width is inversely proportional to the size. Due to the generality of this result we shall use it in later section to evaluate our diffraction code.

3.6 Diffraction Code Construction (Flowchart)

The diffraction code architecture is described here in the form of a flowchart in following figure 3.4.

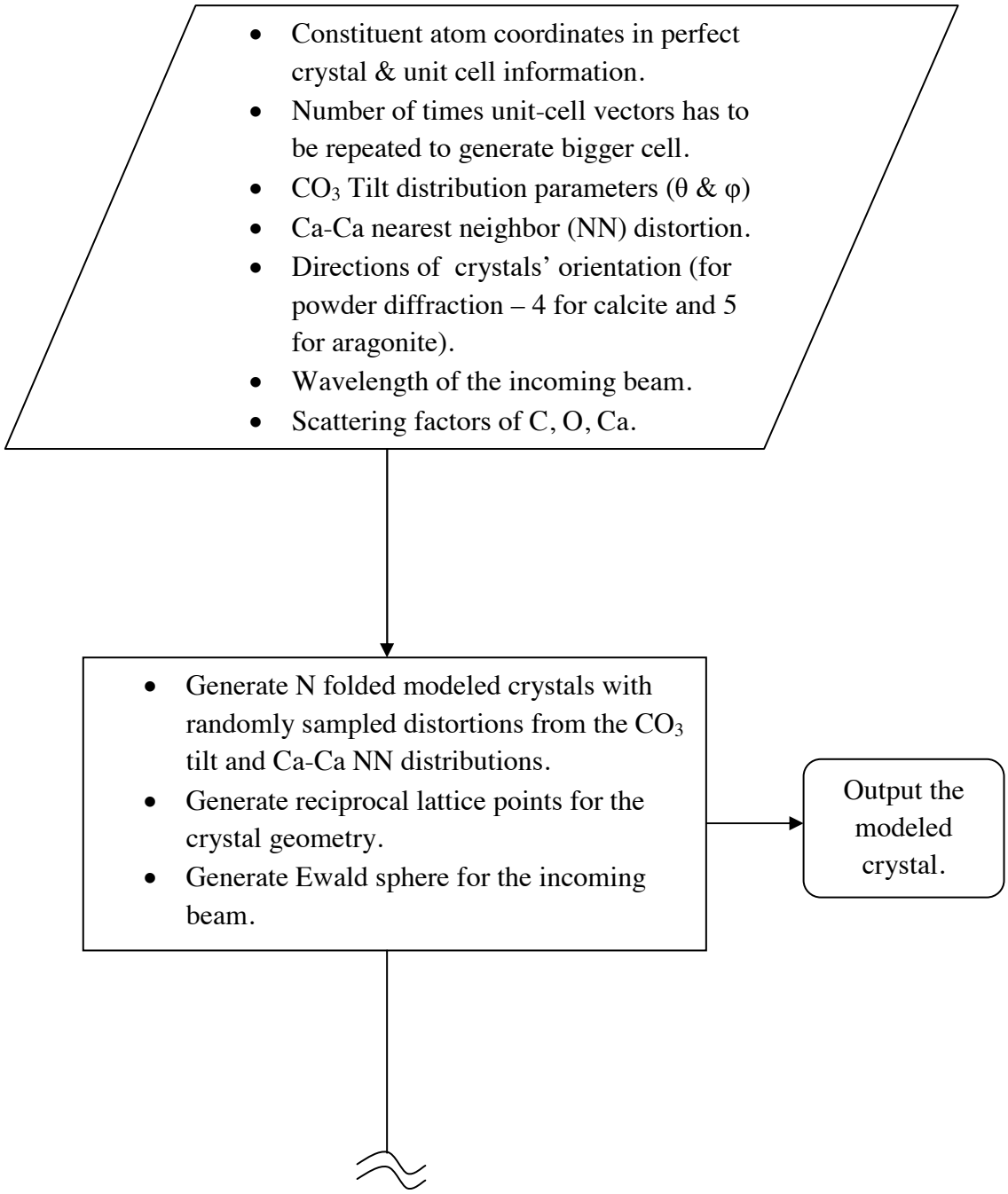
Constituent atom coordinates in perfect crystal & unit cell information.
Number of times unit-cell vectors has to be repeated to generate bigger cell.
CO_3 Tilt distribution parameters (θ & φ)
Ca-Ca nearest neighbor (NN) distortion.
Directions of crystals' orientation (for powder diffraction – 4 for calcite and 5 for aragonite).
Wavelength of the incoming beam.
Scattering factors of C, O, Ca.
Generate N folded modeled crystals with randomly sampled distortions from the CO_3 tilt and Ca-Ca NN distributions.
Generate reciprocal lattice points for the crystal geometry.
Generate Ewald sphere for the incoming beam.
Output the modeled crystal.

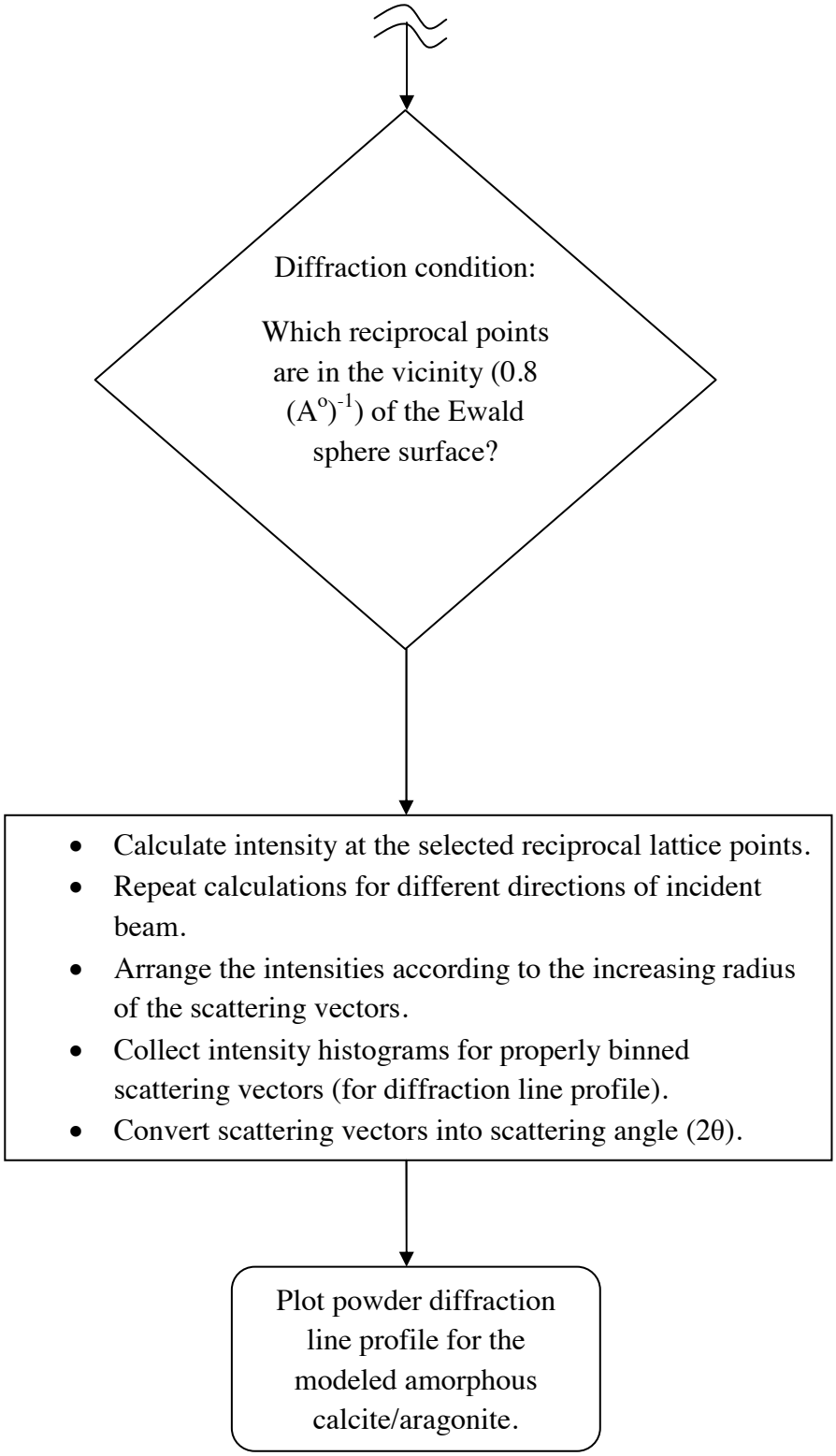

Figure 3.4: Architecture of the diffraction code

3.7 Evaluation of the diffraction code

In this section we shall put our diffraction code to test to make sure that we do not obtain erroneous results from it. In section 3.6 we showed how our indigenous diffraction code can generate a powder diffraction line profile. It is worth mentioning here that given a crystal structure we mainly expect the code to return us the correct positions of its diffraction peaks and the broadening of those peaks. However, in electron diffraction the multiple scattering or the dynamical diffraction [108, 109] can be significant and can alter values of diffracted peak intensities, hence we do not expect the code to accurately predict the peak heights.

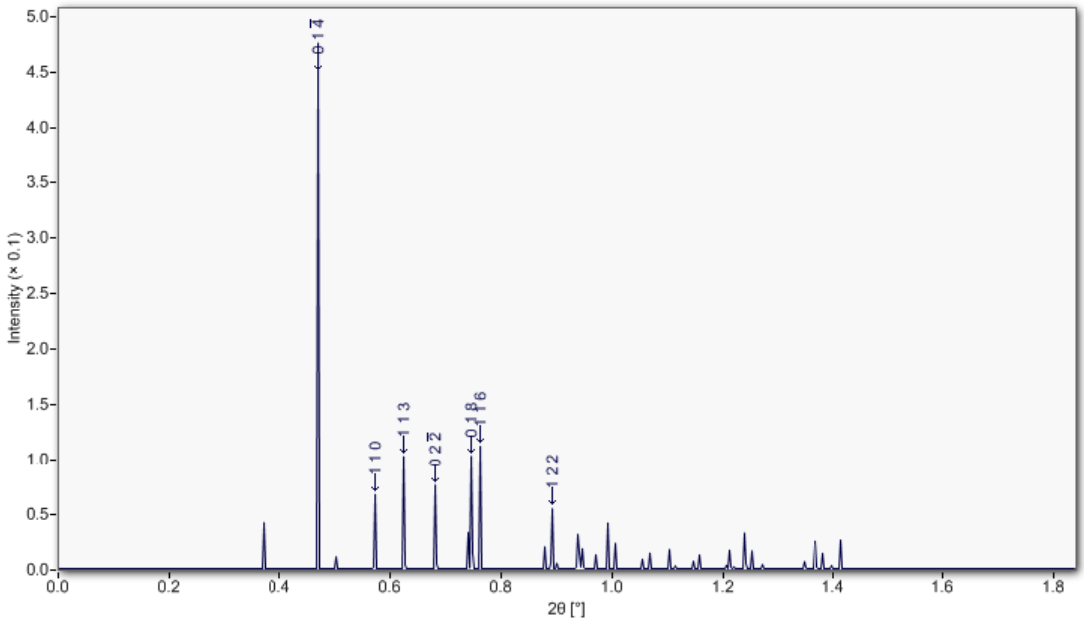

Figure 3.5: Calcite powder diffraction line profile from database (CrystalMaker software library)

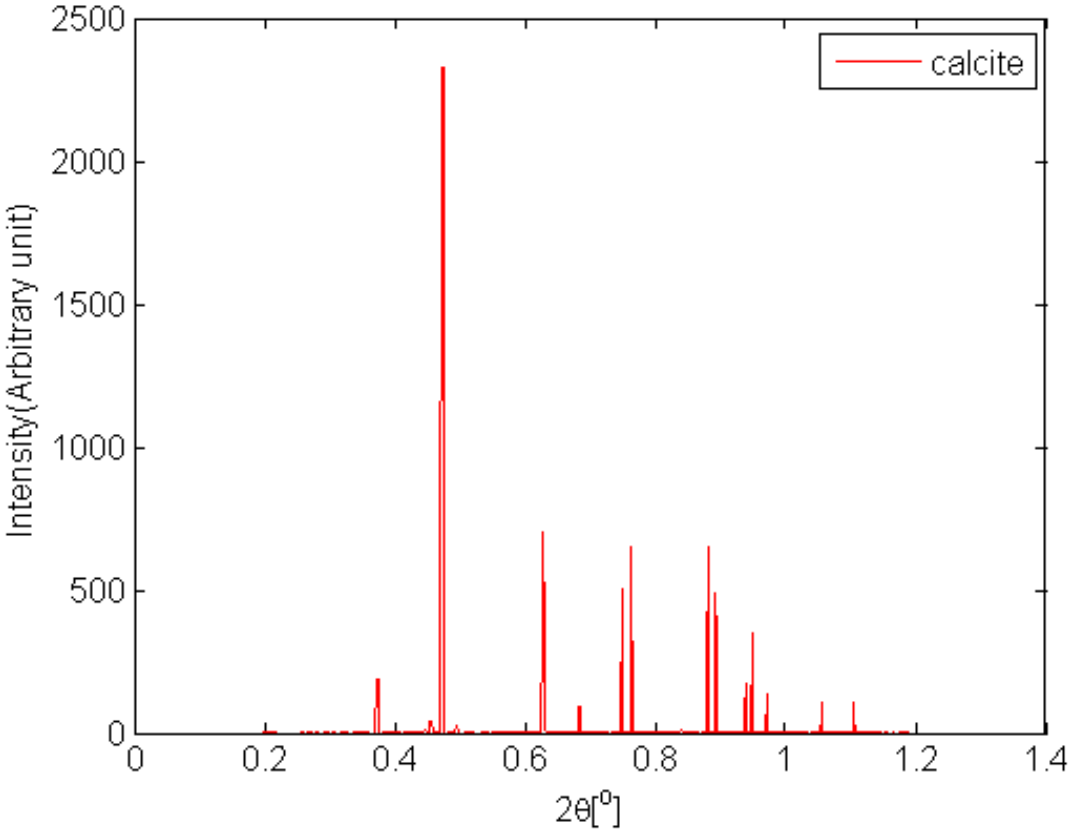

Figure 3.6: Calcite powder diffraction line profile from our diffraction software

Another important point is that we are trying to simulate the powder diffraction profile and for that we should average over many different orientations of the crystal. To expedite our calculation we restricted ourselves to 4 directions ([1,0,0], [0,1,0], [0,0,1], [2,-1,0]) for calcite and 5 directions ([1,0,0], [0,1,0], [0,0,1], [1,1,0], [1,0,1]) for aragonite, as we obtained most of the important peaks in our diffraction profile. But there is a big possibility that this might lead to errors in the calculated diffracted intensity. Regarding the peak position we have tested our code by comparing the diffraction profile with that calculated using CrystalDiffract software [110]. We will also present an analysis based on the argument given in section 3.5 to compare the calcite peak width while varying the crystal size. Since most of our work related to structures derived from

calcite we chose it as a test case. All these tests were done for the wavelength of 0.025 $\mathring{A}$ which corresponds to an electon energy of 200 keV.

Figure 3.5 shows a calcite diffraction line profile from CrystalDiffract. Labels show the Miller indices of the planes from which Bragg reflection occurs Figure 3.6 is the line profile generated for calcite using our code. Comparing the two figures we see our code can generate most of the significant peaks with the exception of the (110) peak. We believe this is due to the fact that we are sampling too few orientation for a powder diffraction, and currently we are working on this. Regarding the relative height of the peaks, we can see that they are comparable though differences are to be expected because we are calculating electron diffraction intensities where CrystalDiffract gives X-ray diffraction intensities. Most importantly it shows that the scattering angle is correct as the locations of the significant peaks match. The dominant (01-4) peak occurs exactly at $2\theta = 0.47^{\circ}$ as one would expect in calcite.

Figure 3.7 shows a comparison between the peak-widths of two perfect nano-crystals, one of size $\sim 10 \times 10 \times 17\ \mathring{A}^3$ and the other $\sim 20 \times 20 \times 34\ \mathring{A}^3$. We would just concentrate on the main $(01\bar{4})$ peak which is fairly broad and distinct. In section 3.5 we have shown (equation 3.22) that doubling the crystal size reduces the peak-width by a factor of half. Hence we should expect the $20 \times 20 \times 34\ \mathring{A}^3$ crystal to have a peak-width half of that of $10 \times 10 \times 17\ \mathring{A}^3$ one. Figure 3.7 shows exactly that, where $10 \times 10 \times 17\ \mathring{A}^3$ has peak width of 0.08° where as for $20 \times 20 \times 34\ \mathring{A}^3$ crystal it is 0.04°.

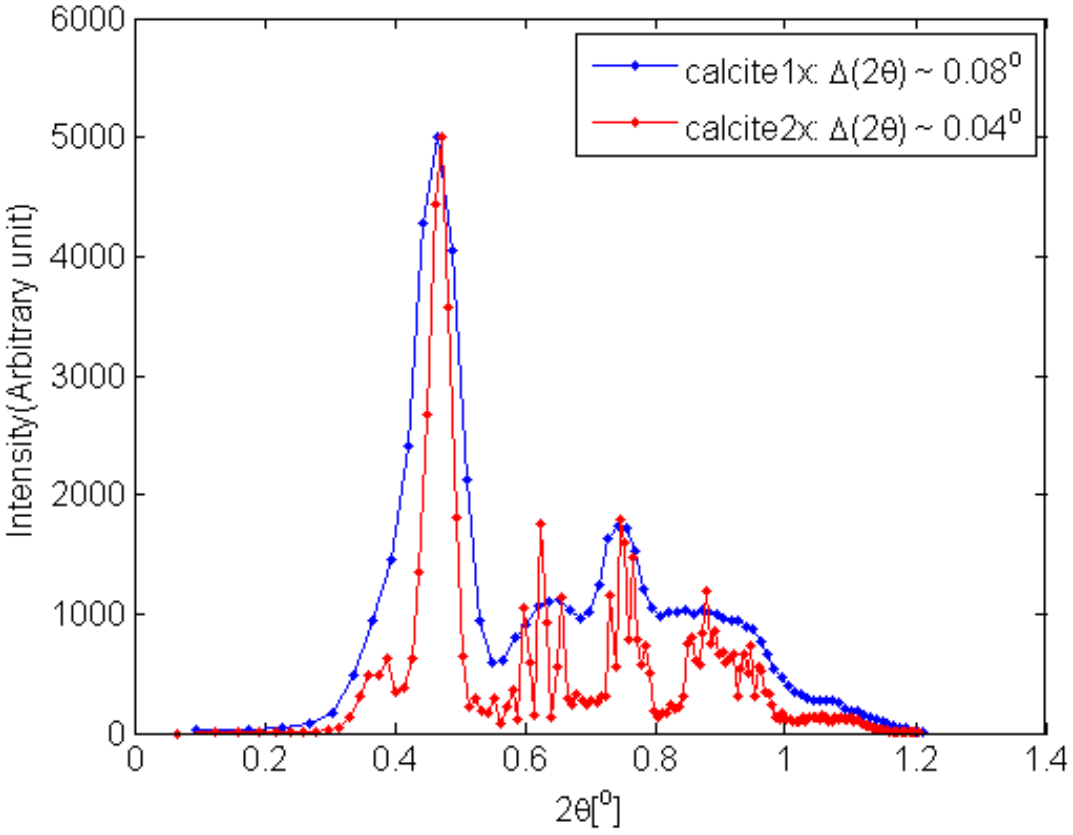

Figure 3.7: Comparison between peak-widths of $10\times10\times17(\text{Å})^3$ and $20\times20\times34\text{Å}^3$ calcite crystals. $\lambda = 0.025$Å.

Chapter 4

DENSITY FUNCTIONAL CALCULATIONS

We started from the hypothesis that disorder in either calcite or aragonite could come about from either Mg substitution for Ca or from interstitial water. Models were generated for various configurations of Mg in a calcite or aragonite supercell and for different distributions of water. The VASP DFT code was used to relax atomic positions to generate a minimum energy structure for that particular configuration. Using an ensemble of different configurations we were able to derive distributions of distortions in the perfect crystal structure. The most prominent of these were tilts of the carbonate planes and a distribution in inter ionic distance in the Ca sub lattice. The distributions were then used in a larger model system to calculate diffraction patterns. In addition the total energies of the different configurations could be used to estimate free energy. This is the first stage in finding the free energy of transformation from candidate structures to the perfect crystal.

4.1 Simulation Systems for VASP

To study the effect of impurities like H_2O and Mg, calcite and aragonite supercells were relaxed with VASP. Here we shall present the systems under consideration.

4.1.1 Calcite

A calcite supercell with 24 formula units was constructed by doubling the hexagonal cell along the '**a**' (length 9.98 $\AA$) and '**b**' (length 9.98 $\AA$) unit cell vectors while keeping '**c**' axis (17.06 $\AA$) the same. Various configurations with 3-5 H_2O molecules and 6 Mg atoms substituting for Ca were relaxed using the VASP plane wave pseudopotential code. On the SAGUARO supercomputing cluster at ASU, each of our systems took approximately 90 hours to relax on 36 parallel nodes. The main reason behind

not choosing a bigger supercell was computation time, as we know for this kind of calculation computation time scales as $\sim N^3$ where N is the number of atoms.

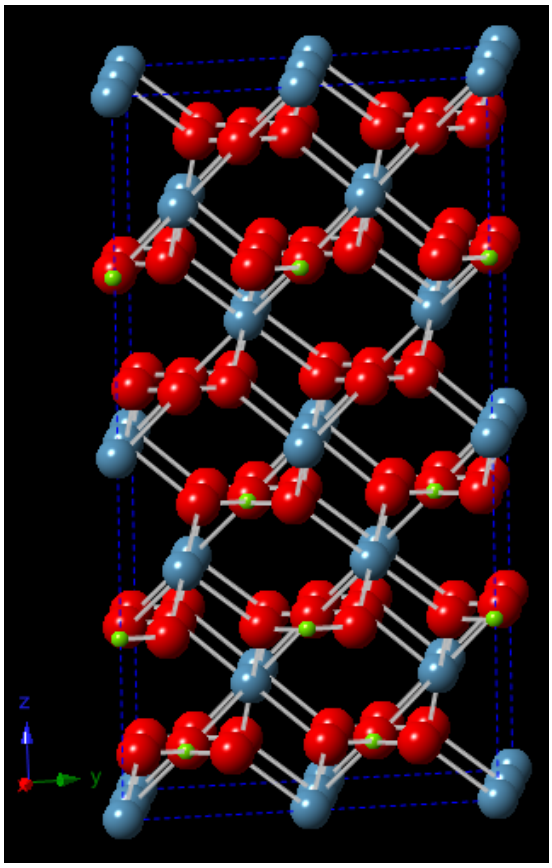

Figure 4.1: A pure calcite supercell viewed down the [100] direction. Color code: Blue = Ca, Red = O, Green = C

As stated before, amorphous $CaCO_3$ can have up to 3.0% (by weight) of water and more than 10% (by wt.) of Mg. We inserted from 3 clustered H_2O molecules (corresponding to 2.25%) to 5 clustered H_2O molecule (3.75%) in the interstitial positions. To observe the differences between clustered impurities and scattered impurities we also simulated calcite supercells with 4 clustered H_2O molecules (3.00%) and 4 scattered H_2O molecules. Regarding Mg as an impurity, we replaced 6 Ca atoms by Mg, corresponding to 6.0 wt%, in the calcite super-cell, keeping the supercell charge neutral. Since Mg and Ca have the same charge one can substitute an arbitrary number

of Mg for Ca. Once again we relaxed two Ca/$MgCO_3$ supercells, one with clustered Mg atoms and the other with scattered Mg atoms. Our expectation is that clustered impurities will have a more dramatic effect on distortion of the pure calcite crystal. Figure (4.1) shows the atomic structure of the perfect calcite supercell. The polyhedral view of the same supercell is shown in figure (4.2) for better visualization of the orientations of the constituent atomic groups i.e. CO_3 groups and the Ca sub-lattice.

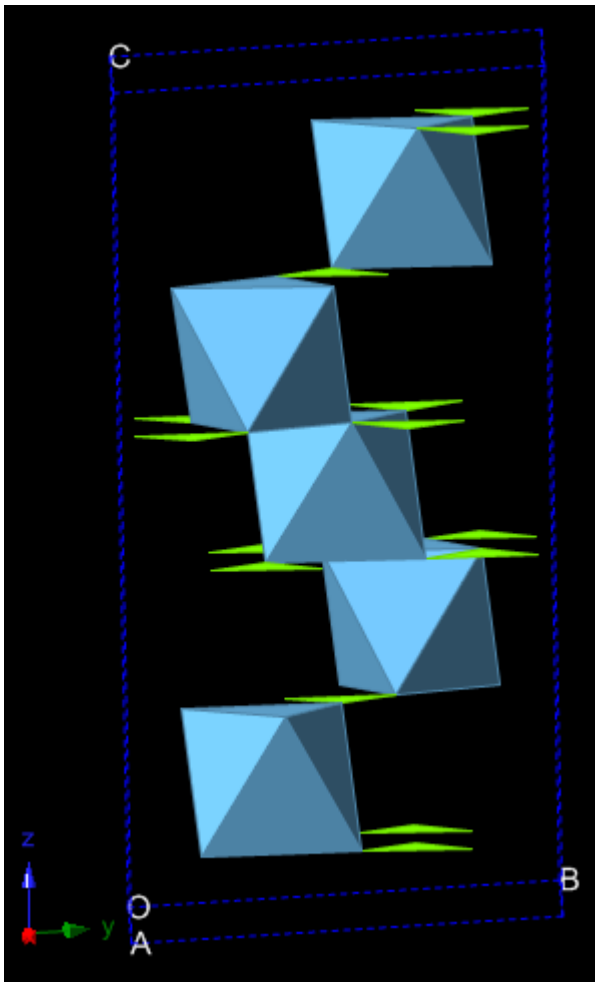

Figure 4.2: Polyhedral view of a pure calcite crystal. Notice, the orientation of triangular carbonate planes and the Ca coordination polyhedral (regular octahedron).

4.1.2 Aragonite

An aragonite supercell with 24 formula units was constructed by doubling the orthorhombic cell along the '**a**' axis (length 9.92 $\AA$) , keeping the '**b**' axis unchanged (length 7.98 $\AA$) and tripling the '**c**' axis (17.22 $\AA$). Once again computation time was the limiting factor behind the choice of the supercell size.

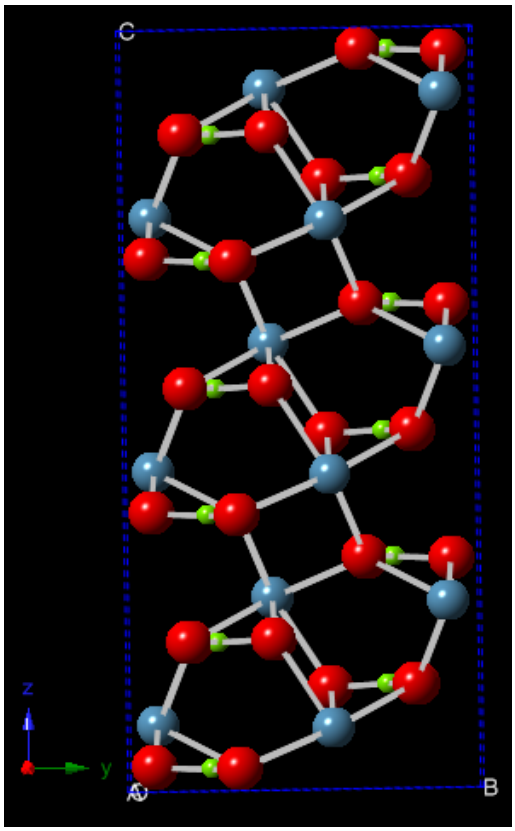

Figure 4.3: A pure aragonite supercell when viewed from (100) direction. Color code: Blue = Ca, Red = O, Green = C

Like calcite we also chose the same impurity configurations i.e. insertion of 3 to 5 H_2O molecules, corresponding to 2.25% to 3.75% by weight and substitution of 6 Ca atoms by Mg corresponding to 6 wt.%. To observe the effect of clustered impurities, we simulated 4 scattered H_2O molecules and 6 scattered Mg atoms. Figure 4.3 shows the

atomic structure of the prefect aragonite supercell, and figure 4.4 depicts its constituent carbonate groups' orientations.

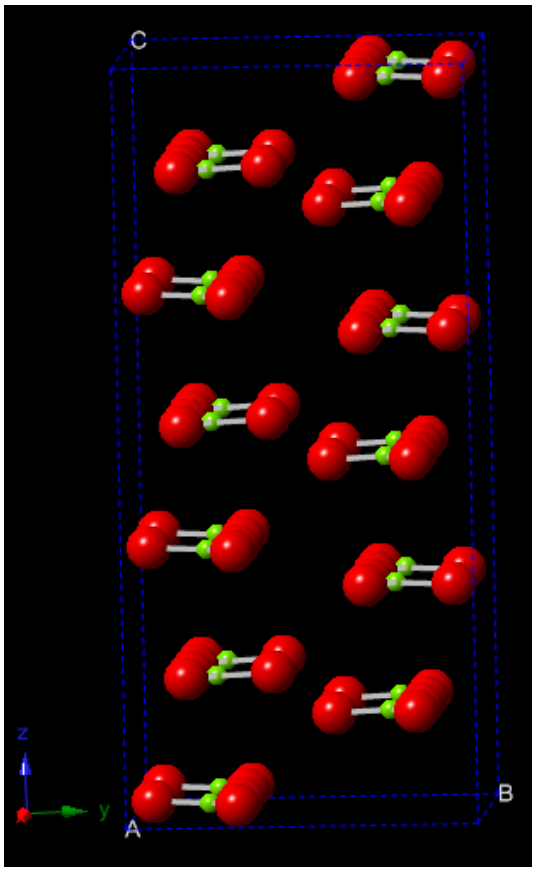

Figure 4.4: Orientation of carbonate groups in a pure aragonite crystal. Like in calcite, they are also oriented parallel to the basal plane (001)

4.2 Free Energy Calculation of the Relaxed Structures

We want to investigate whether it is energetically favorable for impurities to be scattered around the supercell or clustered together. We therefore calculated the free energy for both clustered and scattered cases. The free energy of a system is defined as:

$$F = E - TS \tag{4.1}$$

Where, 'E' is the total energy of the system, 'T' is the temperature (room temperature in our case) and 'S' is entropy.

The entropy can be obtained using Boltzmann's famous formula,

$$S = k_B \ln(\Omega) \tag{4.2}$$

where 'Ω' is the number of arrangements of the impurities distributed among the available interstitial (for H_2O) or substitutional (for Mg) positions. For scattered impurities, calculation of Ω_{Sc} is straight forward and can be given by,

$$\Omega_{Sc} = \frac{N!}{(N-n)!n!} - \Omega_{Cl} \tag{4.3}$$

where 'k_B' is Boltzmann constant = 8.6173324×10^5 eV/°K, 'N' is the number of interstitial or substitutional positions and 'n' corresponds to number of impurity atoms or molecules, i.e. in our case there are 6 Mg and 3-5 H_2O molecules. Since the total number of configurations include the clustered cases we have to substract Ω_{Cl} to obtain Ω_{Sc}. However it should be noticed that the number of clustered combinations is so small compared to the total number of configurations, the substraction does not make much difference. It should be mentioned that among hydrated systems we only considered the scattered case for 4 H_2O molecules.

The calculation of Ω_{Cl} for clustered configurations is not straight forward, and careful enumeration of the available positions inside a supercell is necessary for its determination. The criteria for this search should be the proximity of the impurities and the non-equivalence of the available sites. Non-equivalent sites are a necessary condition because of the symmetry in a crystalline environment. Ω_{Cl} for the clustered impurity configurations considered above are tabulated below.

Impurity	Crystal System	Range ($\AA$)	Non-equivalent Sites (Ω_{Cl})
4 H_2O	calcite	8.0	15
4 H_2O	aragonite	7.0	70
6 Mg	calcite	10.0	1
6 Mg	aragonite	8.0	22

Table 4.1: Ω_{cl} for clustered impurity configurations

From equation 4.1 the free energy difference between scattered and clustered impurity systems can be written as,

$$\Delta F_{Sc-Cl} = \Delta E_{Sc-Cl} - T\Delta S_{Sc-Cl} \tag{4.4}$$

Below we tabulate free energy differences between clustered and scattered impurity systems for both calcite and aragonite using equation 4.1 through 4.4 and table 4.1.

Impurity	N	n	$T\Delta S_{Sc-Cl}$ (eV)	$E_{Clustered}$ (eV)	$E_{Scattered}$ (eV)	ΔF_{Sc-Cl} (eV)
H_2O	24	4	0.17	-958.27	-953.60	4.50
Mg	24	6	0.31	-900.33	-899.65	0.37

Table 4.2: Free energy calculations for calcite

Impurity	N	n	$T\Delta_{Sc-Cl}S$ (eV)	$E_{Clustered}$ (eV)	$E_{Scattered}$ (eV)	ΔF_{Sc-Cl} (eV)
H_2O	24	4	0.13	-954.92	-953.60	1.19
Mg	24	6	0.22	-891.32	-891.10	0.00

Table 4.3: Free energy calculations for aragonite

In the above calculations T was considered to be 300 $^{\circ}$K. Observing ΔF_{Sc-Cl} in table 4.2 and 4.3 it can be concluded that for the hydrated case, in both calcite and aragonite supercells, the clustered impurity configuration is clearly favored over the

scattered configuration. For the magnesium case, clustered configuration is slightly preferred over the scattered configuration in calcite but not so much in aragonite.

4.3 CO_3 Tilt and Ca-Ca Nearest Neighbor Distance (NND) Distributions

The two main effects which were observed after the relaxation of Calcite and Aragonite supercell in the presence of impurities (H_2O and Mg) are the tilt of the carbonate planes and a distortion of the calcium sub-lattice. To observe the characteristics of these distortions we shall study their frequency distributions collected from the relaxed structures.

4.3.1 Tilt of the Carbonate Planes for Calcite

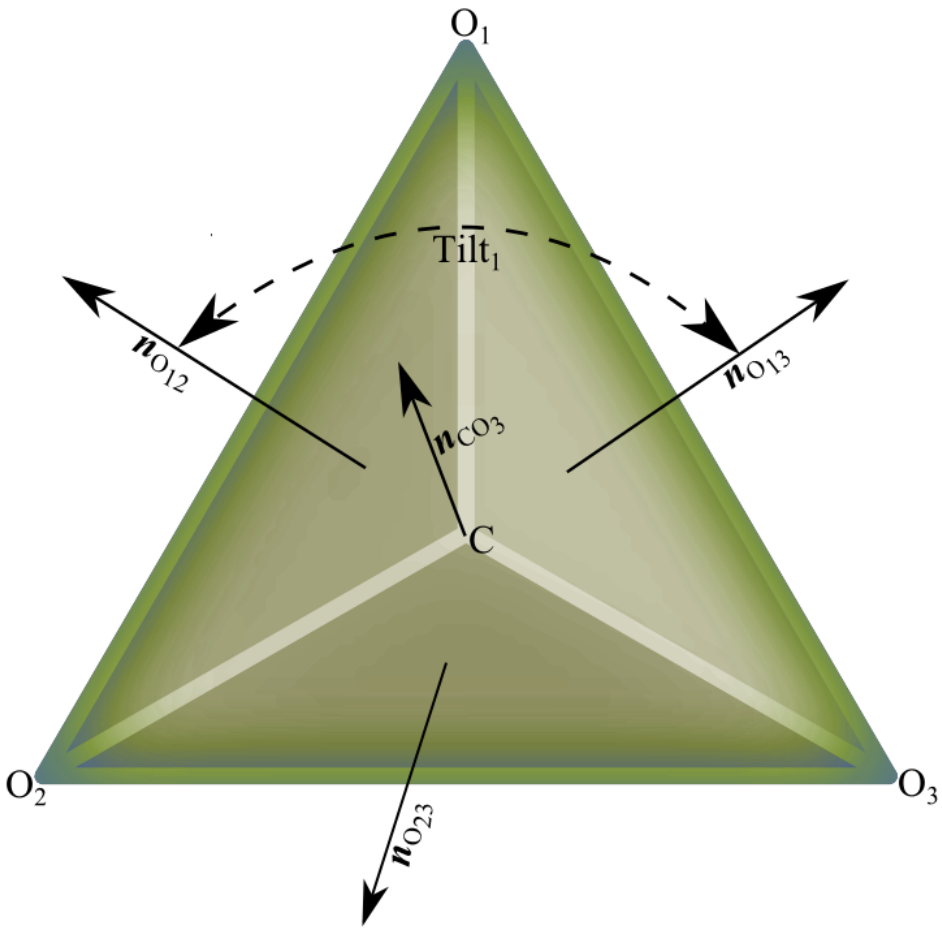

Figure 4.5: Schematics of carbonate tilt

In figure (4.1) and (4.2) we saw that in calcite, the carbonate (CO_3) groups are arranged in the shape of equilateral triangles, stacked between the Ca planes. The normal vectors to those triangular carbonate planes are parallel to the '**c**' axis of the crystal. During relaxation it is possible that the carbonate planes get distorted due to the interaction between crystal atoms and impurities. The cartoon in figure (4.5) shows a hypothetical distorted carbonate group, where the C atom is at the middle and three O atoms (denoted by O_1, O_2 and O_3) reside at the other three vertices. The normal to the basal triangular plane, passing through C, is denoted by $\mathbf{n}_{CO_3}$ which is equivalent to the '**c**' axis in a perfect crystal. Normal to the triangular plane O_1-C-O_2 in figure (4.5) is shown by $n_{O_{12}}$. Similarly $\mathbf{n}_{O_{23}}$ and $\mathbf{n}_{O_{31}}$ represents the normal to the other CO_3 sub-planes. We denote the angle between $\mathbf{n}_{O_{12}}$ and $\mathbf{n}_{O_{13}}$ as 'tilt_1'. Similarly the angle between $\mathbf{n}_{O_{12}}$ and $\mathbf{n}_{O_{23}}$ is called 'tilt_2' and angle between $\mathbf{n}_{O_{23}}$ and $\mathbf{n}_{O13}$ as 'tilt_3'. It is important to realize that if the carbonate plane just tilts as a whole but maintains its planarity, as can be seen in figure (4.8), then one should expect all the $\text{tilt}_{1,2,3}$ angles to be very close 0. However, since the carbonate planes can tilt as a whole, the tilt of the whole carbonate plane i.e. tilt_{CO_3} which is the angle between $\mathbf{n}_{CO_3}$ and crystrallographic '**c**' axis, can be big. We should also expect that the individual C-O bond length in each CO_3 group should not change much. The angles between sub-carbonate groups i.e. $\text{tilt}_{1,2,3}$-s for each of 24 (supercell contains 24 formula units of $CaCO_3$) CO_3 groups in one of the simulated (4 clustered H_2O system) calcite systems are tabulated in table (4.4). Table (4.5) gives the change of C-O bond length in each CO_3 group for the same system. Other simulations show very similar results. These tables clearly show how little the CO_3 planes distort during the relaxation. Figure (4.6) though (4.10) are some examples of calcite supercells before and after relaxation in the presence of impurities i.e. H_2O and Mg. The tilt of the whole carbonate groups i.e. tilt_{CO_3}-s will be discussed in details in chapter 5.

CO_3 Group Number	Angle Between $\mathbf{n}_{O_{12}}$ and $\mathbf{n}_{O_{23}}$ (Degrees)	Angle Between $\mathbf{n}_{O_{23}}$ and $\mathbf{n}_{O_{31}}$ (Degrees)	Angle Between $\mathbf{n}_{O_{31}}$ and $\mathbf{n}_{O_{12}}$ (Degrees)
1	1.07	1.04	1.06
2	0.33	0.33	0.31
3	0.25	0.25	0.25
4	0.50	0.51	0.49
5	0.26	0.26	0.26
6	2.61	2.62	2.61
7	0.40	0.34	0.36
8	2.58	2.66	2.58
9	0.02	0.02	0.02
10	0.23	0.24	0.24
11	0.24	0.24	0.24
12	1.59	1.69	1.72
13	1.06	1.07	1.04
14	0.24	0.24	0.23
15	0.49	0.48	0.48
16	0.40	0.41	0.41
17	0.42	0.42	0.42
18	2.80	2.81	2.81
19	0.40	0.39	0.38
20	2.67	2.76	2.66
21	0.05	0.04	0.04
22	0.82	0.80	0.81
23	0.15	0.15	0.15
24	1.63	1.71	1.76

Table 4.4: Angle between normals of O-subgroup in CO_3 groups for 4 clustered water calcite relaxed structure.

CO_3 Group Number	Δ_{frac}(C-O_1) (%)	Δ_{frac}(C-O_2) (%)	Δ_{frac}(C-O_3) (%)
1	0.54	0.52	0.02
2	0.94	1.50	0.56
3	0.05	0.07	0.02
4	0.05	0.45	0.50
5	0.10	0.14	0.24
6	1.31	0.29	1.01
7	0.03	0.30	0.27
8	0.34	0.25	0.09
9	0.10	0.20	0.11
10	0.08	0.06	0.14
11	0.01	0.04	0.05
12	0.98	2.05	1.07
13	0.08	0.55	0.47
14	0.96	1.32	0.36
15	0.09	0.07	0.02
16	0.44	0.02	0.42
17	0.09	0.13	0.22
18	1.25	0.32	0.93
19	0.20	0.03	0.23
20	0.28	0.25	0.02
21	0.11	0.18	0.07
22	0.33	0.11	0.22
23	0.01	0.08	0.10
24	1.22	1.91	0.69

Table 4.5: Fractional percentage change in individual C-O distance in CO_3 groups for four clustered water calcite relaxed structure. Original C-O bond length in perfect Calcite is 1.292 $\AA$.

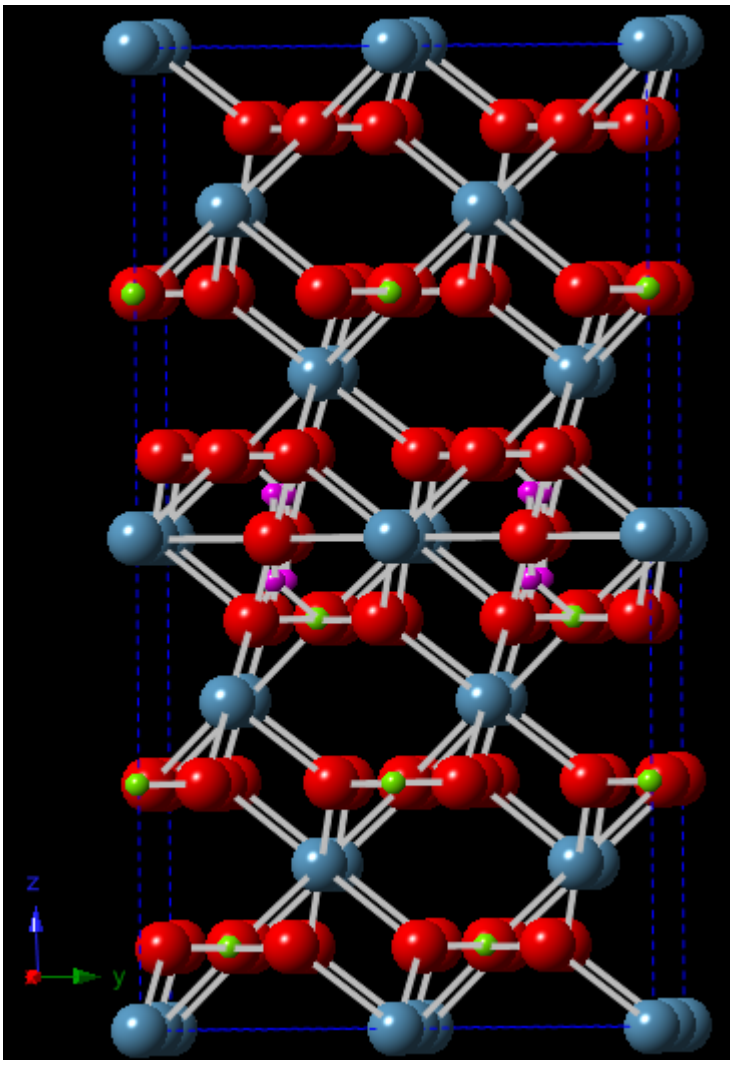

Figure 4.6: Before relaxation, 4 clustered H_2O molecules inserted in a pure calcite. H atoms are shown in pink

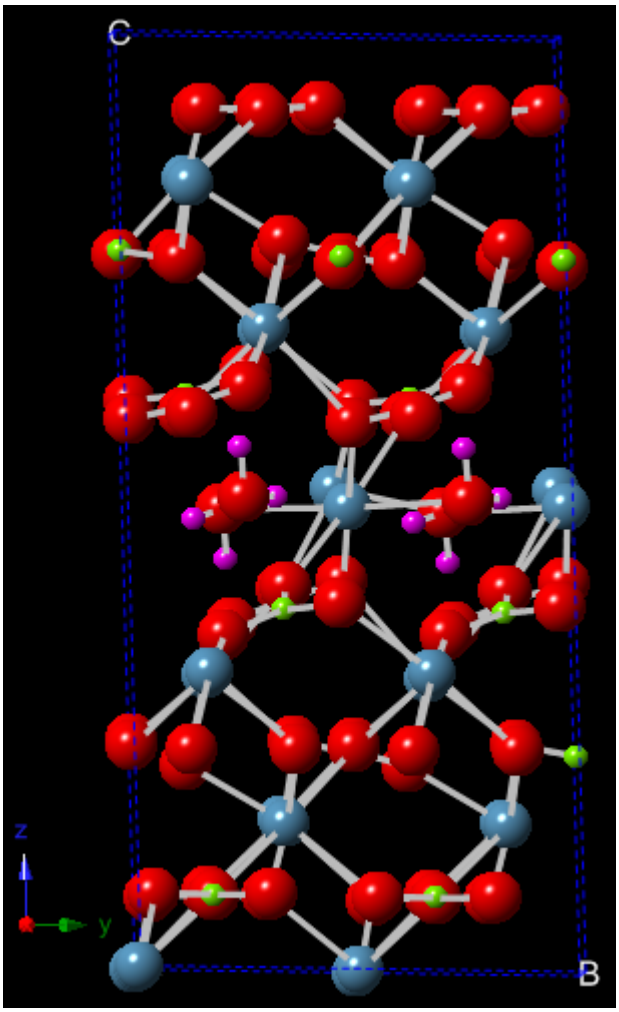

Figure 4.7: After relaxation, 4 clustered H_2O molecules + calcite system. Notice the tilting of the carbonate planes in the vicinity of H_2O molecule

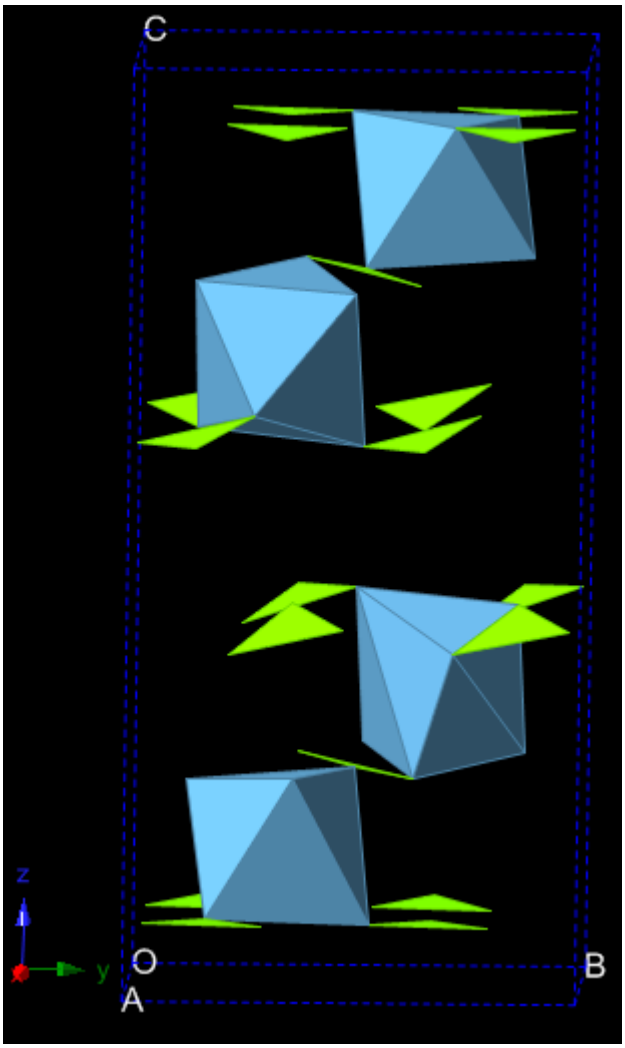

Figure 4.8: Polyhedral view of 4 clustered H_2O molecules + calcite system after relaxation. Notice the carbonate plane tilts and distortion of the polyhedron shapes when compared with figure 4.2

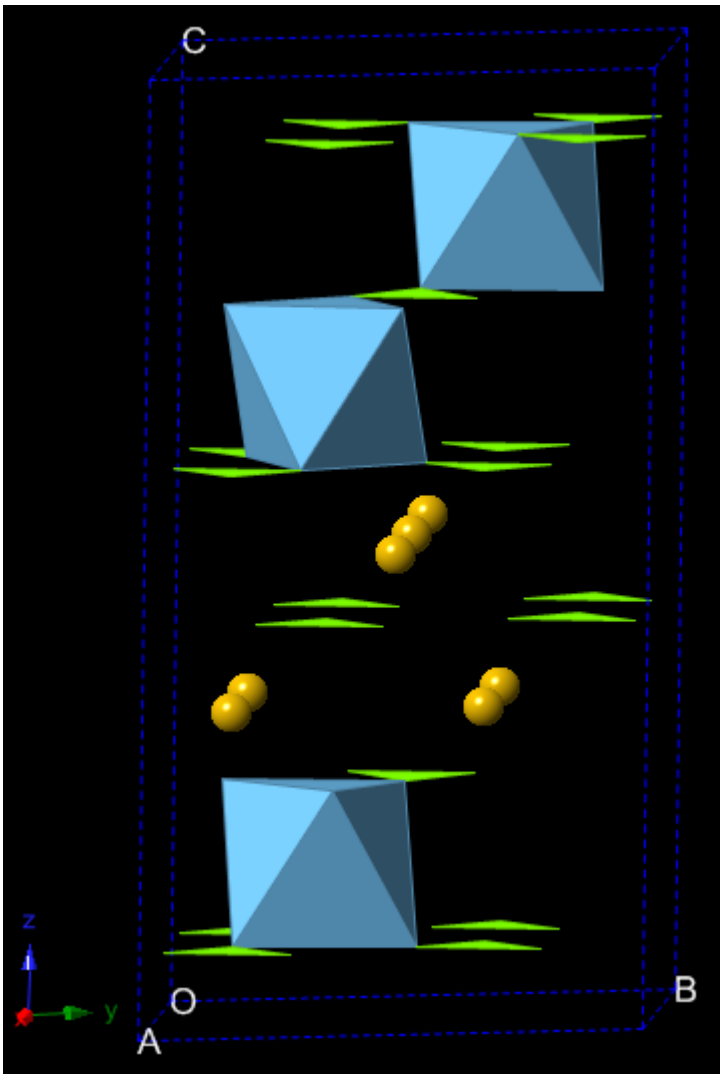

Figure 4.9: Before relaxation, polyhedral view of 6 clustered Mg atoms replacing 6 Ca atoms in a pure calcite. Notice the orderliness of the carbonate planes in the vicinity of impurities and the shapes of the polyhedra formed by Ca atoms. Notice that the carbonate planes are all parallel to the basal plane (001)

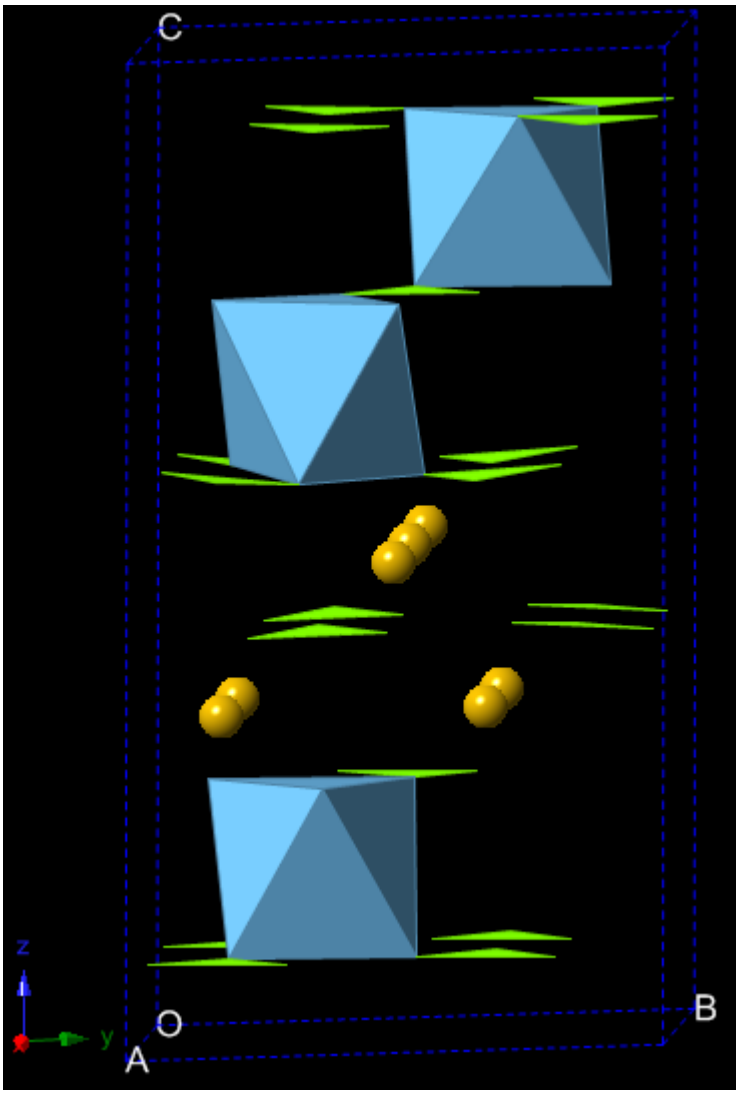

Figure 4.10: Polyhedral view of 6 clustered Mg atoms replacing 6 Ca atoms in a pure calcite after relaxation. Comparing it with figure (4.8) reveals that the tilts of the carbonate planes in the vicinity of impurities but the shapes of the Ca coordination polyhedra are almost unchanged, suggesting there was not much distortion of the Ca sub-lattice

Observation of table (4.4) and (4.5), and Figure (4.8) through (4.10) clearly reveals that the CO_3 planes of the calcite crystal have not distorted much due to the introduction of impurities like H_2O and Mg, but maintain their planer triangular shape. The actual range of $tilt_{1,2,3}$ angle distributions for all the simulated systems are tabulated in table (4.6). The sub-carbonate tilt distributions for the calcite system with 5 clustered H_2O molecules, a typical distribution noticed in all the simulations, are shown in figure (4.11) through (4.13). It should be mentioned that the largest distortions ($\sim 4^\circ$) in the carbonate groups occur near the impurities for all configurations.

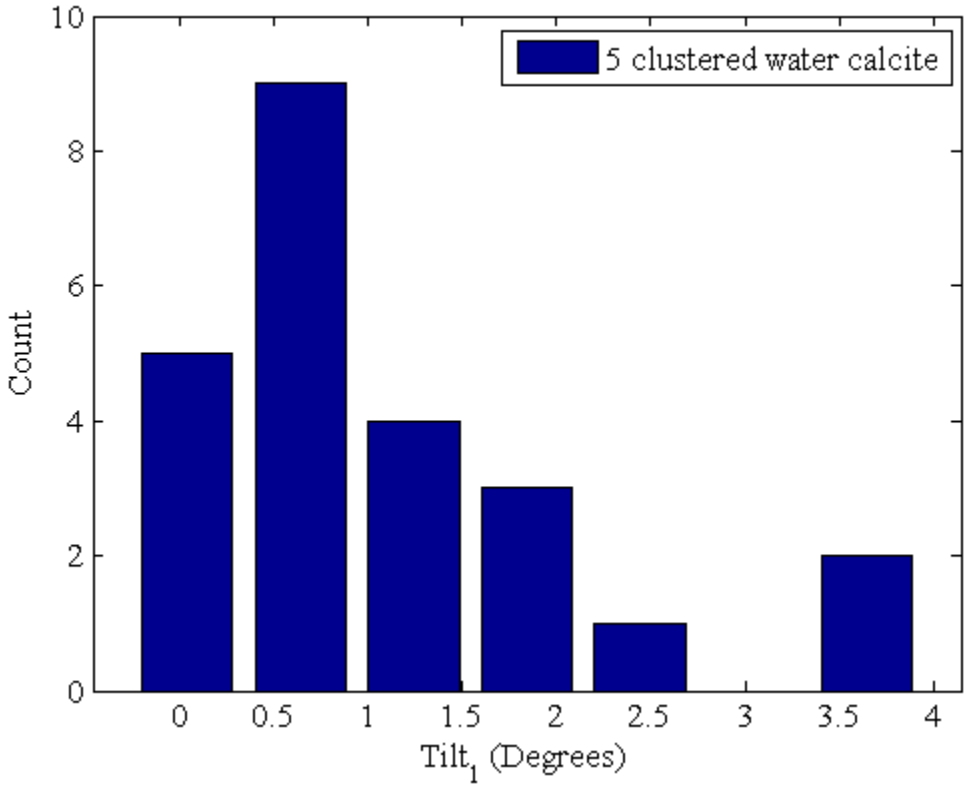

Figure 4.11: Carbonate $tilt_1$ histogram in 5 clustered H_2O molecules impurities in the calcite system after relaxation. Refer to figure (4.5) for definition of $tilt_1$.

Configuration	$Tilt_1$ Range (Degree)	$Tilt_2$ Range (Degree)	$Tilt_3$ Range (Degree)
3 clustered H_2O	0.03 - 3.97	0.02 - 4.10	0.03 - 3.99
4 clustered H_2O	0.02 - 2.80	0.02 - 2.81	0.02 - 2.81
4 scattered H_2O	0.03 - 5.65	0.03 - 5.67	0.03 - 5.62
5 clustered H_2O	0.04 - 3.64	0.04 - 3.78	0.05 - 3.70
6 clustered Mg	0.00 - 2.70	0.02 - 2.71	0.00 - 2.70
6 scattered Mg	0.02 - 3.23	0.03 - 3.21	0.02 - 3.19

Table 4.6: Range of tilt angle distributions for simulated calcite supercell with impurities.

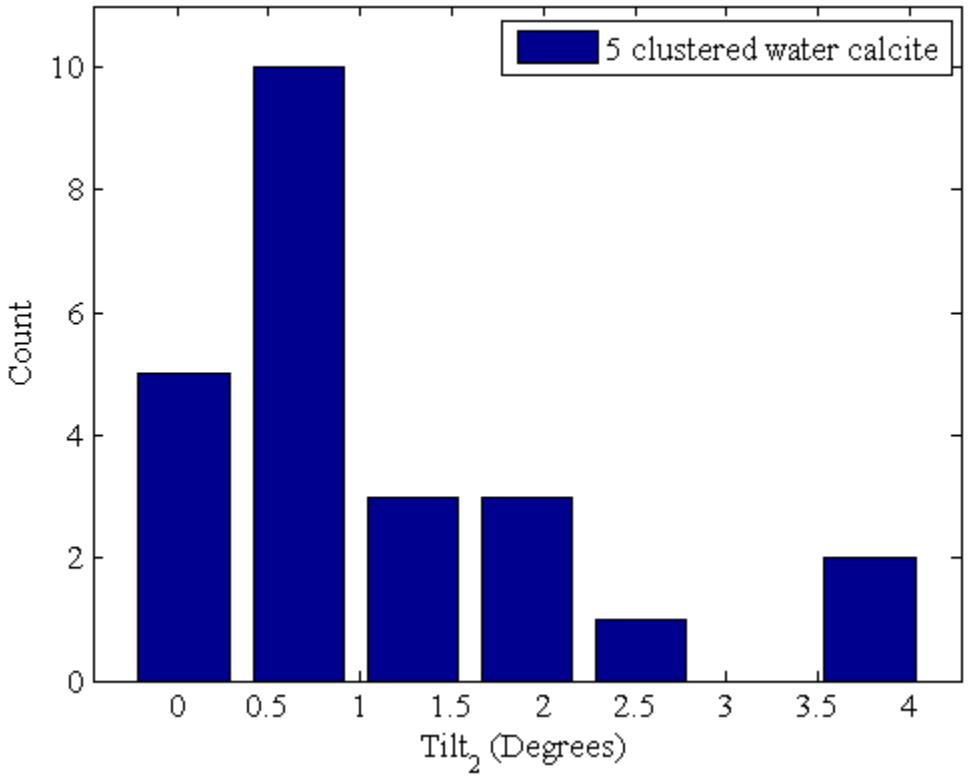

Figure 4.12: Carbonate $tilt_2$ histogram in 5 clustered H_2O molecules impurities in the calcite system after relaxation. Refer to figure (4.5) for definition of $tilt_2$.

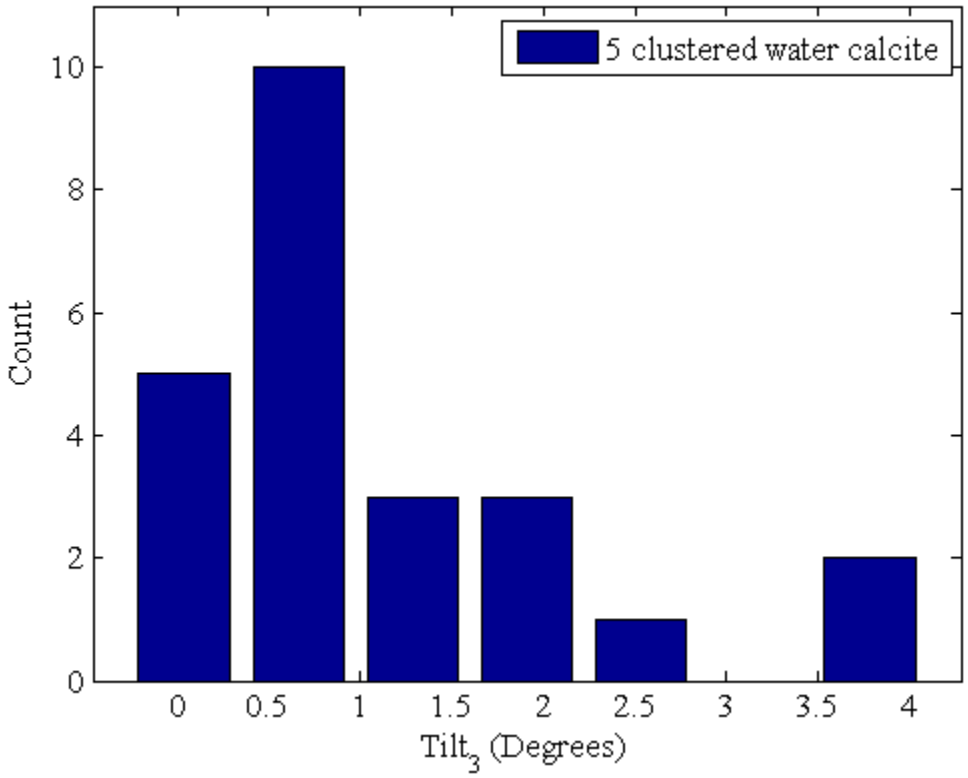

Figure 4.13: Carbonate $tilt_3$ histogram in 5 clustered H_2O molecules impurities in the calcite system after relaxation. Refer to figure (4.5) for definition of $tilt_3$.

Though we have not calculated the tilt of the whole-carbonate groups i.e. $tilt_{CO_3}$ angles yet, but observing figures (4.8) and (4.10), it can easily be noticed that the magnitude of whole-carbonate plane tilts in hydrated systems are much larger than the magnesium systems. This is true in general and can be confirmed from table (5.1) and (5.2). This is because in the hydrated case we are trying to shove a H_2O molecule in the existing free space or interstices in the calcite supercell where as in the Mg case we are doing a substitution with an isovalent ion (Ca), hence probably the only expected effect would be slight changes in bond length.

4.3.2 Distortion of calcium sub-lattice for Calcite

The second kind of distortion introduced in the Calcite supercell due to the introduction of impurities was a Ca sub-lattice distortion. This can be seen clearly in figure (4.14) where the 'blue' and yellow color represents the unrelaxed and relaxed Ca atoms respectively. Comparison of the polyhedral view in figure (4.15) with figure (4.2) gives a better stereoscopic picture of the Ca-sublattice distortion in calcite.

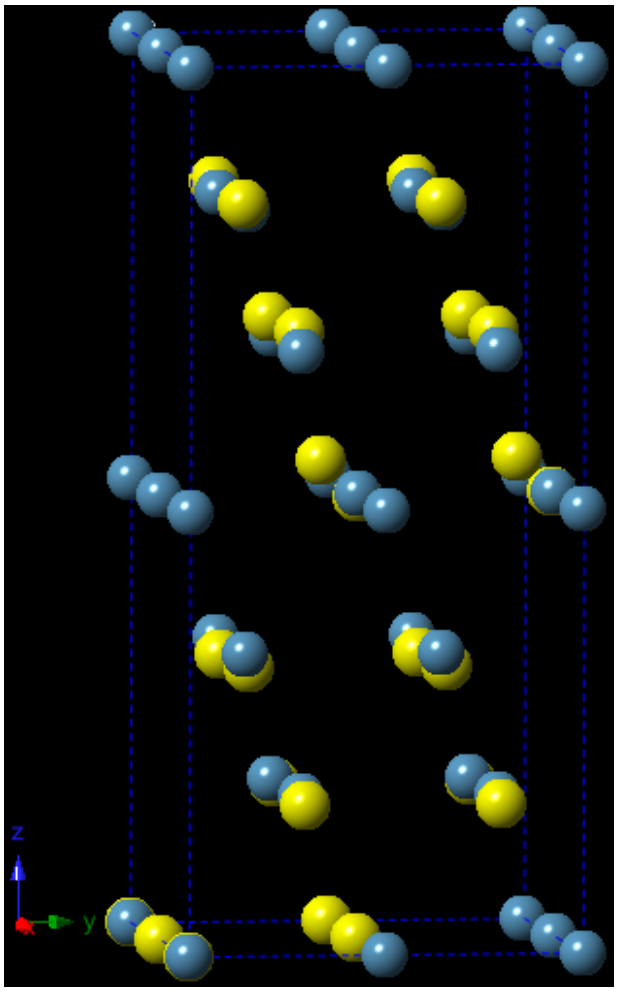

Figure 4.14: Ca sub-lattice with 4 clustered H_2O molecules as impurities in calcite system. The color blue and yellow represents the Ca ion positions before and after relaxation. Notice greater distortion (compare with figure (4.7)) near the middle of the cell where H_2O molecules were inserted

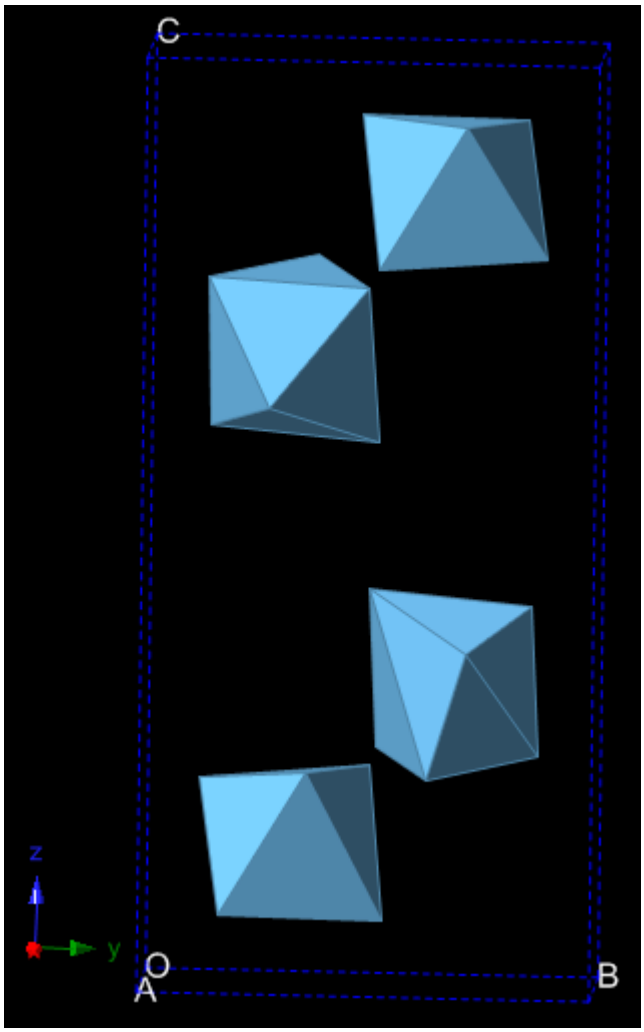

Figure 4.15: Polyhedra formed by Ca atoms in 4 clustered H_2O molecules + calcite system after relaxation. Notice the change of polyhedron shapes (compare with figure (4.2)) which suggests distortion of Ca sub-lattice

A typical Ca-Ca nearest neighbor distance distribution is shown in figure (4.16). In table (4.7) we tabulate the maximum, minimum, mean and standard deviation of the Ca-Ca nearest neighbor distance for each configuration. Here the Ca-Ca nearest neighbor distance (NND) was defined by the shortest distance between two Ca ions in the Ca sub-lattice.

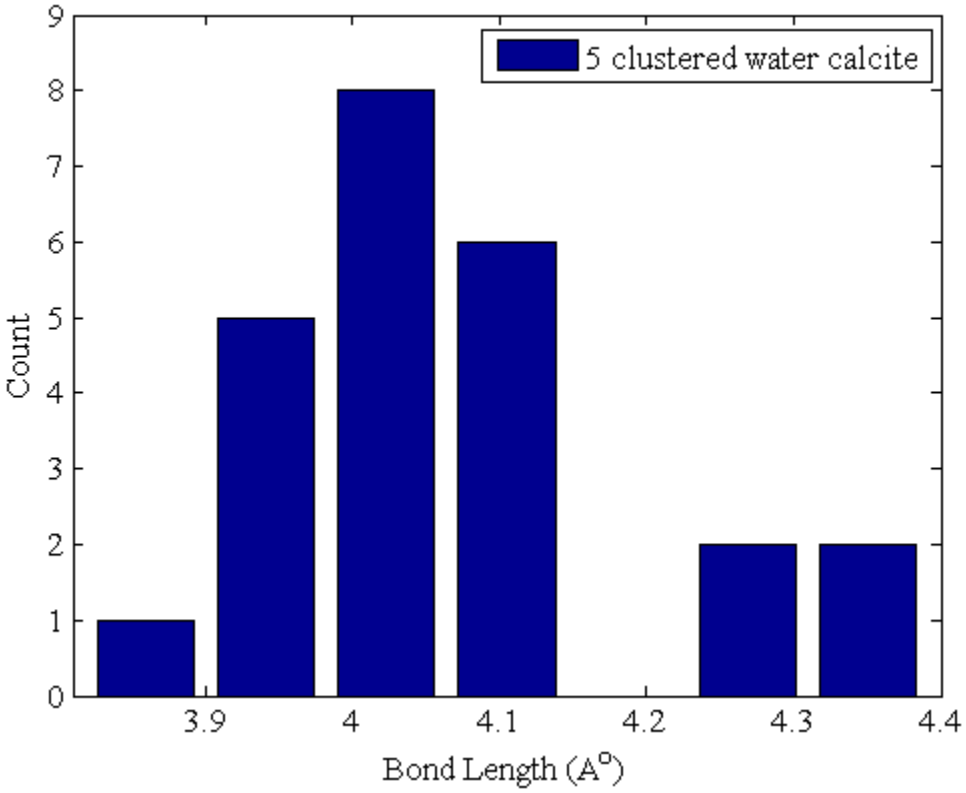

Figure 4.16: Ca-Ca nearest neighbor distance distribution in 5 clustered H_2O molecules impurities in calcite system after relaxation.

Configuration	Max NND ($\AA$)	Min NND ($\AA$)	Mean NND ($\AA$)	Std. Dev NND ($\AA$)
3 clustered H_2O	4.47	3.83	4.06	0.17
4 clustered H_2O	4.45	3.85	4.06	0.15
4 scattered H_2O	4.38	3.79	4.07	0.15
5 clustered H_2O	4.35	3.86	4.06	0.13
6 clustered Mg	4.00	3.94	3.98	0.03
6 scattered Mg	4.01	3.87	3.93	0.05

Table 4.7: Ca-Ca nearest neighbor distance in calcite for all the simulation systems.

It should be noted that for a perfect calcite crystal the Ca-Ca nearest neighbor distance is 4.05 $\AA$. As expected, we observed larger distortions occur in the vicinity

of the impurity atoms or molecules. Once again generally the Ca sub-lattice distortion was less for Mg substitution than H_2O insertion.

4.3.3 Tilt of the Carbonate Planes for Aragonite

Like calcite similar effects were observed in aragonite with both insertion of water molecules into interstices and substitution of Ca ions by Mg. Figure (4.17) and (4.20) shows the aragonite supercells with 4 clustered H_2O molecules and 6 clustered Mg atoms as impurities before relaxation. Figures (4.18) and (4.21) depict the same systems after relaxation. Figure (4.19) shows the CO_3 groups' tilts in the relaxed structure. Table (4.8) shows the angle between vectors $n_{O_{1,2,3}}$ for each CO_3 group in the relaxed 4 clustered H_2O Aragonite system. In a perfect Aragonite cell these angles should be 0° (refer to figure 4.4 and 4.5). Observing table (4.8) we can see that the CO_3 groups' deformation is small enough to maintain their planarity. It should be mentioned that for aragonite the CO_3 groups' distortions are larger than calcite. The fractional change of C-O bond lengths for each CO_3 group for the same system is tabulated in table (4.9), which shows that the C-O bond lengths remain almost unchanged for all the CO_3 groups. Very similar results are noticed for all the other relaxed systems. The sub-carbonate tilt angles i.e. $tilt_{1,2,3}$ distributions for 4 H_2O clustered molecules in the aragonite supercell are presented in figure (4.22) through (4.24). The range of the tilt angles for all the impurity configurations are presented in table (4.10). Regarding the tilt of the whole-carbonate groups i.e. $tilt_{CO_3}$-s, exactly like calcite, the carbonate plane tilts here are much less for Mg substitution than the H_2O insertion, which is expected for the reason mentioned in section (4.3.1). Though there are not many tilt angles for statistical analysis, from table (5.1) and (5.2) it seems that in general (though not always true) the carbonate tilt angles' magnitude increases as the number of impurity atoms or molecules increase in the supercell. Also the local environment around the impurity plays an important role in its determination.

CO_3 Group Number	Angle Between $\mathbf{n}_{O12}$ and $\mathbf{n}_{O23}$ (Degrees)	Angle Between $\mathbf{n}_{O23}$ and $\mathbf{n}_{O31}$ (Degrees)	Angle Between $\mathbf{n}_{O31}$ and $\mathbf{n}_{O12}$ (Degrees)
1	3.98	4.08	4.11
2	4.81	4.80	4.80
3	4.17	4.18	4.21
4	4.05	4.11	4.10
5	4.08	3.98	4.06
6	4.32	4.31	4.38
7	4.30	4.36	4.38
8	3.73	3.87	3.88
9	4.44	4.46	4.44
10	3.05	3.03	3.14
11	0.22	0.22	0.22
12	6.38	6.37	6.55
13	4.34	4.39	4.47
14	1.65	1.62	1.63
15	2.03	2.05	1.94
16	0.96	0.91	0.98
17	4.33	4.34	4.38
18	4.60	4.55	4.61
19	4.05	4.10	4.13
20	4.68	4.74	4.76
21	4.34	4.36	4.37
22	3.92	3.96	3.98
23	4.04	4.11	4.24
24	4.65	4.61	4.67

Table 4.8: Angle between normals of O-subgroup in CO_3 groups for 4 clustered water aragonite relaxed structure.

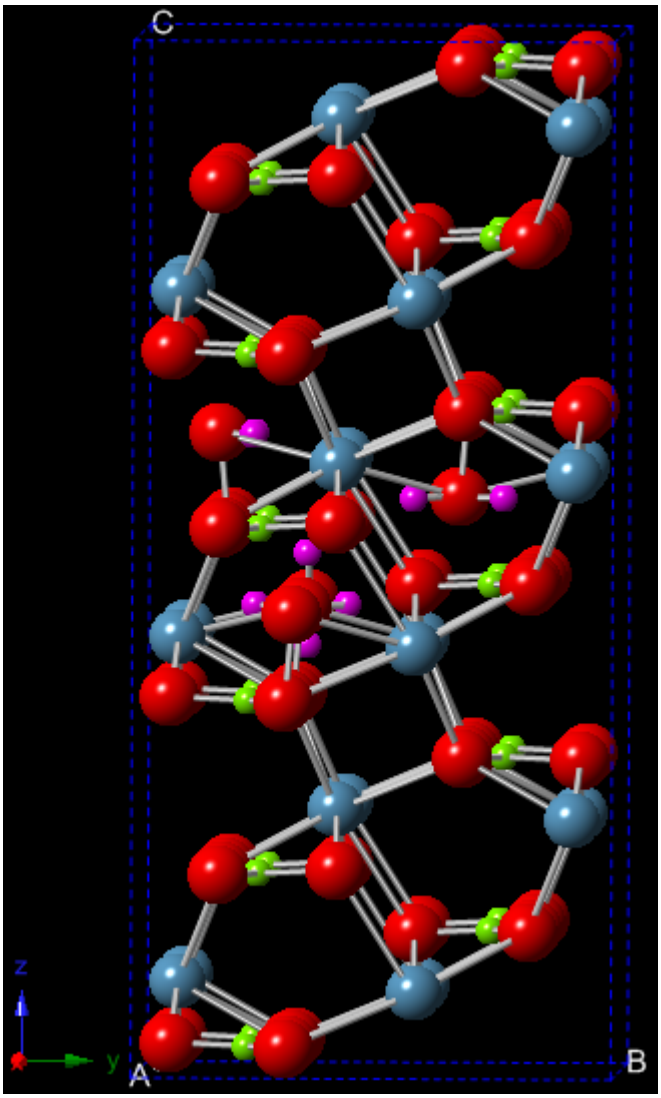

Figure 4.17: Before relaxation, 4 clustered H_2O molecules inserted in a pure aragonite. H atoms are shown in pink. Notice the order of the carbonate planes in the vicinity of H_2O molecules and that they are all parallel to the basal plane (001)

CO_3 Group Number	Δ_{frac}(C-O_1) (%)	Δ_{frac}(C-O_2) (%)	Δ_{frac}(C-O_3) (%)
1	0.62	0.82	0.20
2	0.23	0.07	0.15
3	0.44	0.32	0.12
4	0.39	0.62	0.23
5	0.35	0.40	0.75
6	0.65	0.36	0.29
7	0.53	0.56	0.03
8	0.75	1.51	0.76
9	0.30	0.61	0.31
10	0.77	0.32	0.45
11	0.99	0.12	0.87
12	0.06	1.15	1.09
13	1.39	1.80	0.41
14	0.92	0.61	1.53
15	0.91	1.37	2.28
16	0.39	0.21	0.17
17	0.55	0.29	0.27
18	0.56	0.11	0.67
19	0.36	0.48	0.84
20	0.23	0.43	0.20
21	0.39	0.33	0.06
22	0.80	0.47	0.33
23	0.66	0.85	0.20
24	0.63	0.14	0.49

Table 4.9: Fractional percentage change in individual C-O distance in CO_3 groups for four clustered water aragonite relaxed structure. Original C-O bond length in perfect Aragonite is 1.284 $\AA$.

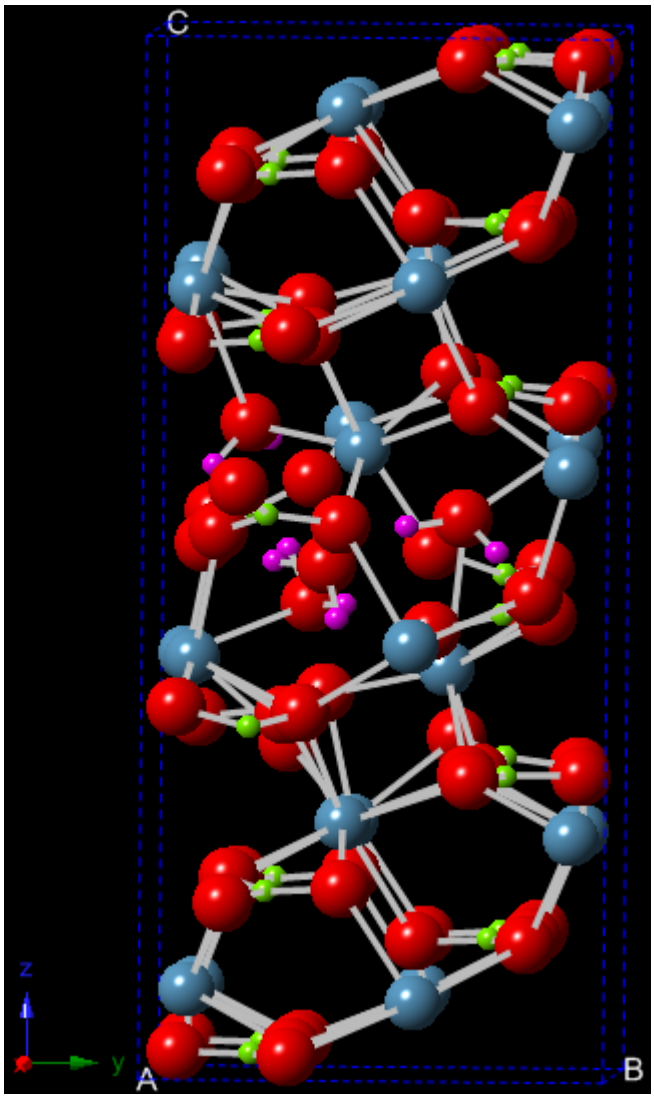

Figure 4.18: After relaxation, 4 clustered H_2O molecules + aragonite system. Notice the tilting of the carbonate planes and the distortion of bonds in the vicinity of H_2O molecules. Compare with figure (4.17) to notice the distortion especially in the middle of the cell where impurities were inserted

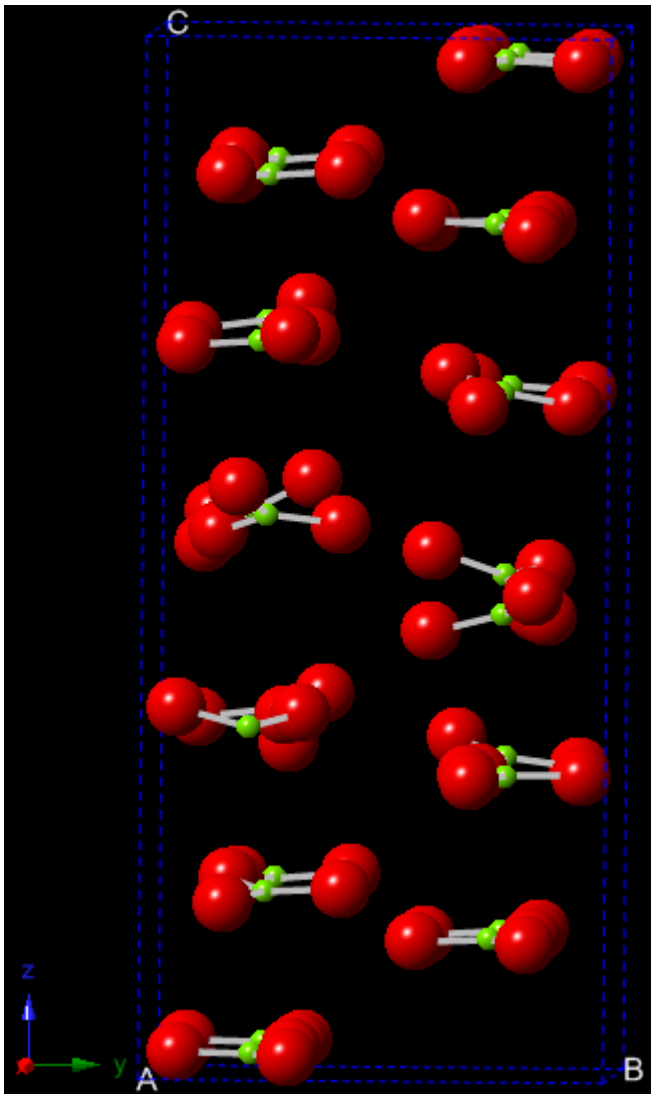

Figure 4.19: Carbonate group orientations after relaxation of 4 clustered H_2O molecules + aragonite system. Compare with figure (4.4) to notice the carbonate tilts.

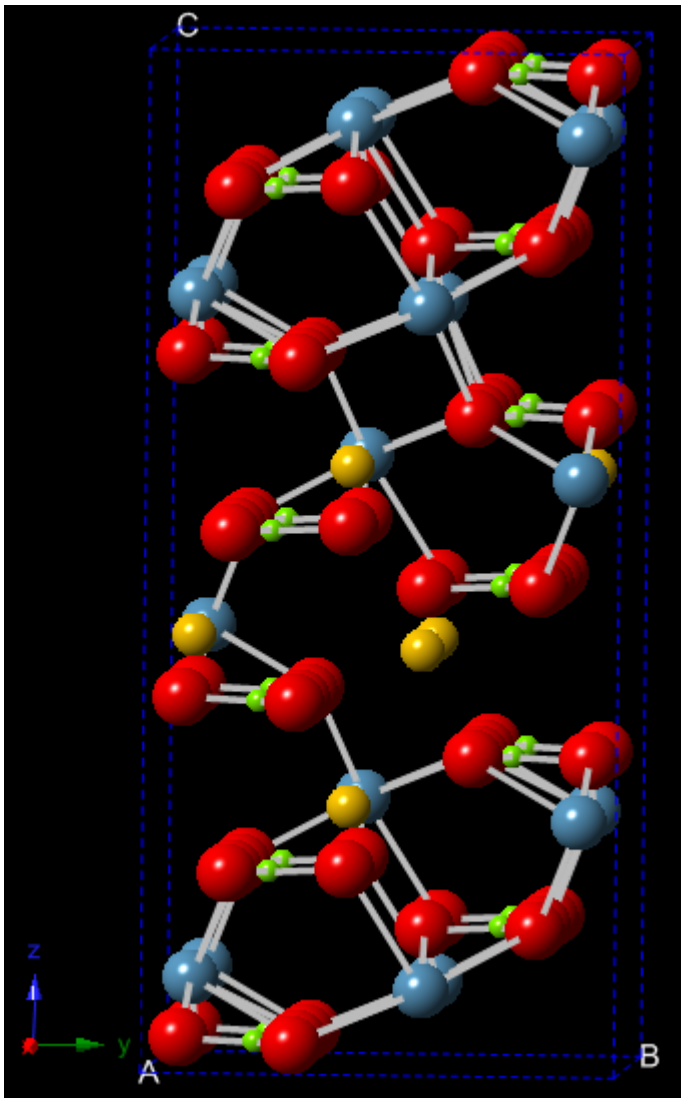

Figure 4.20: Before relaxation, 6 clustered Mg atoms replacing 6 Ca atoms in a pure aragonite. Notice that the carbonate planes in the vicinity of impurities are all parallel to the basal plane

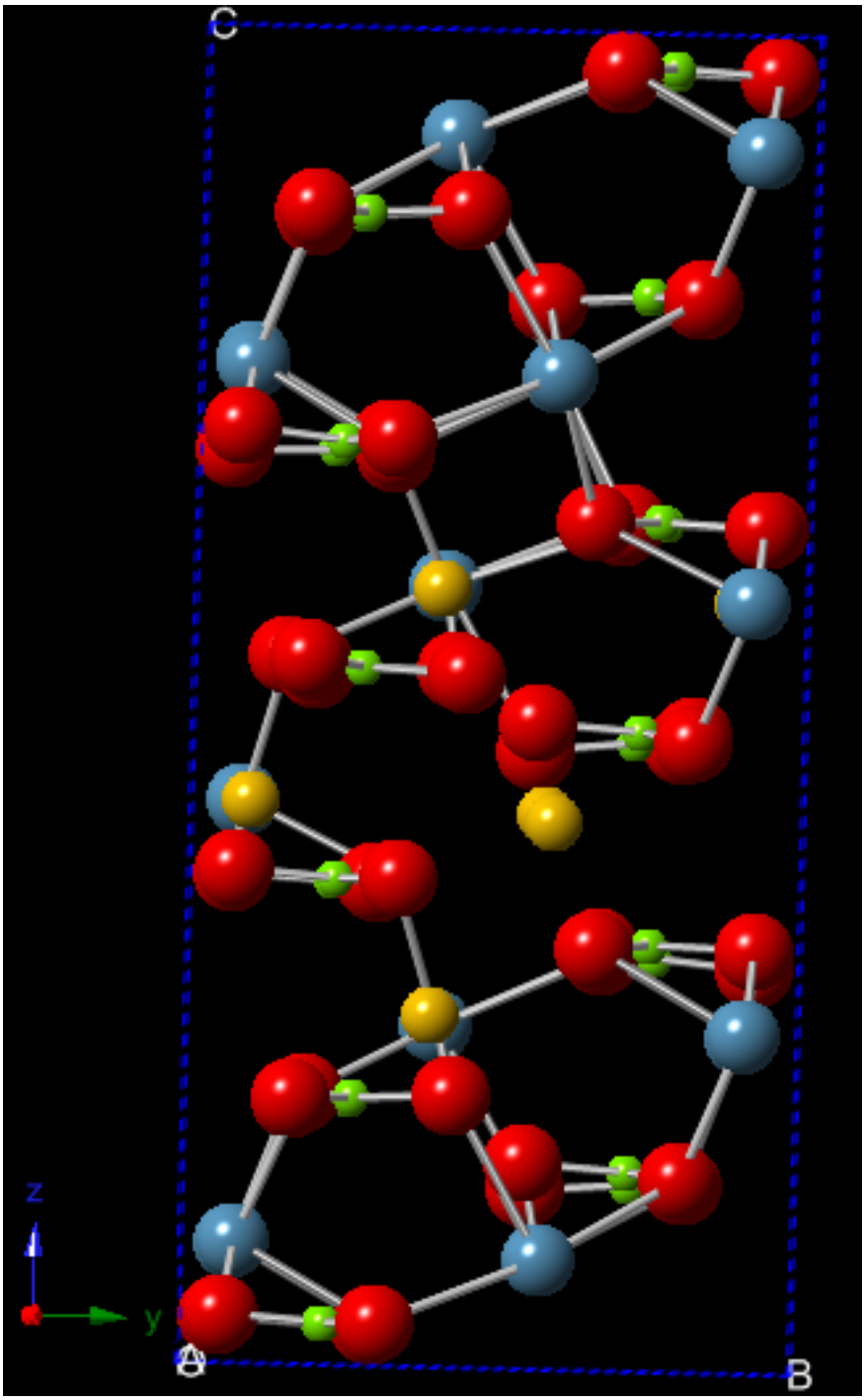

Figure 4.21: After relaxation, 6 clustered Mg atoms replacing 6 Ca atoms in a pure aragonite. Notice that there is not much distortion after relaxation (compare with figure (4.20))

Configuration	$Tilt_1$ Range (Degree)	$Tilt_2$ Range (Degree)	$Tilt_3$ Range (Degree)
3 clustered H_2O	1.73 - 5.10	1.69 - 5.26	1.71 - 5.25
4 clustered H_2O	0.22 - 6.38	0.23 - 6.37	0.22 - 6.55
4 scattered H_2O	0.34 - 5.31	0.34 - 5.14	0.35 - 5.37
5 clustered H_2O	1.94 - 6.43	2.00 - 6.41	1.94 - 6.38
6 clustered Mg	4.02 - 6.00	4.03 - 6.00	4.03 - 6.07
6 scattered Mg	3.97 - 5.83	4.01 - 5.85	4.09 - 5.91

Table 4.10: Range of tilt angle distributions for all the simulated aragonite systems.

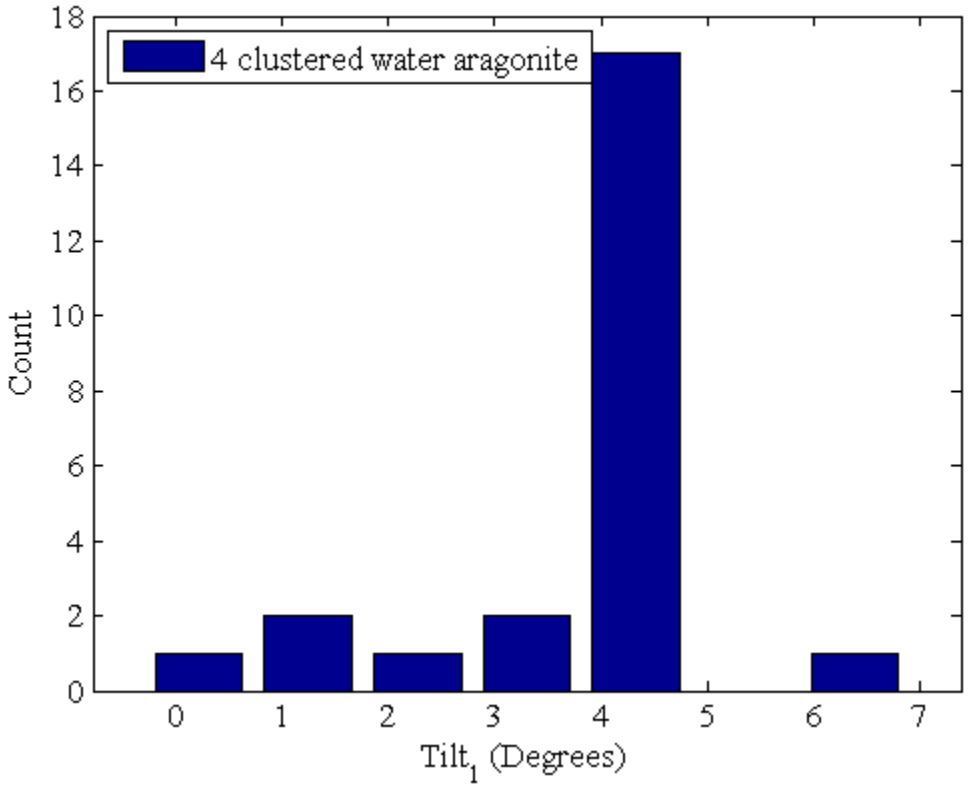

Figure 4.22: Carbonate $tilt_1$ histogram in 4 clustered H_2O molecules impurities in the aragonite system after relaxation. Refer to figure (4.5) for definition of $tilt_1$.

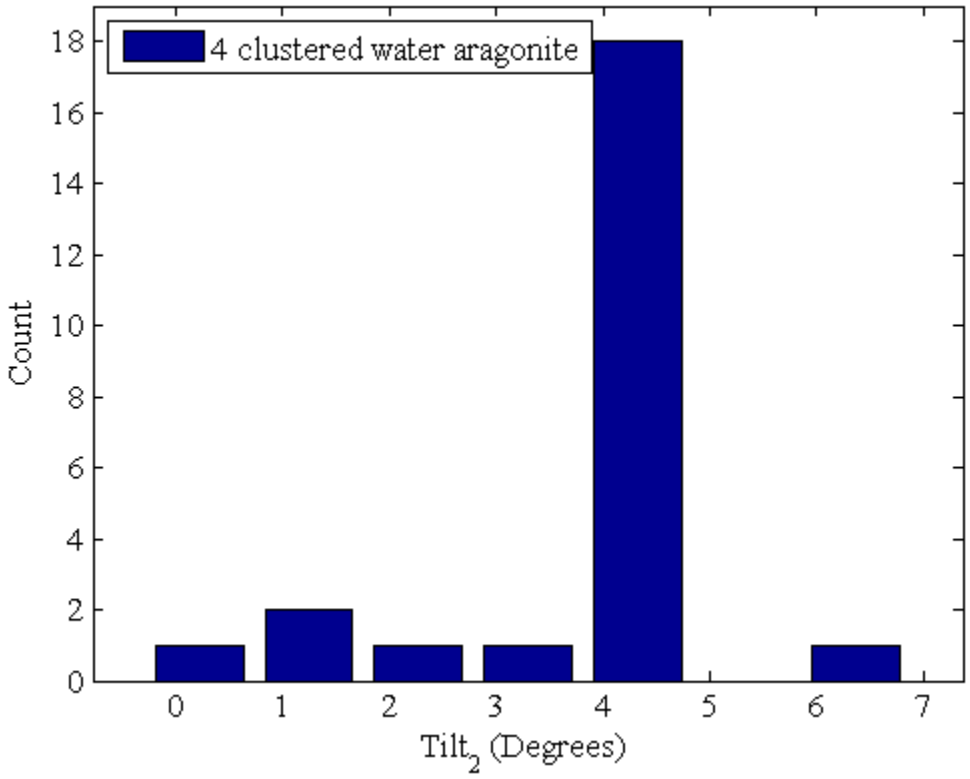

Figure 4.23: Carbonate tilt$_2$ histogram in 4 clustered H_2O molecules impurities in the aragonite system after relaxation. Refer to figure (4.5) for definition of tilt$_2$.

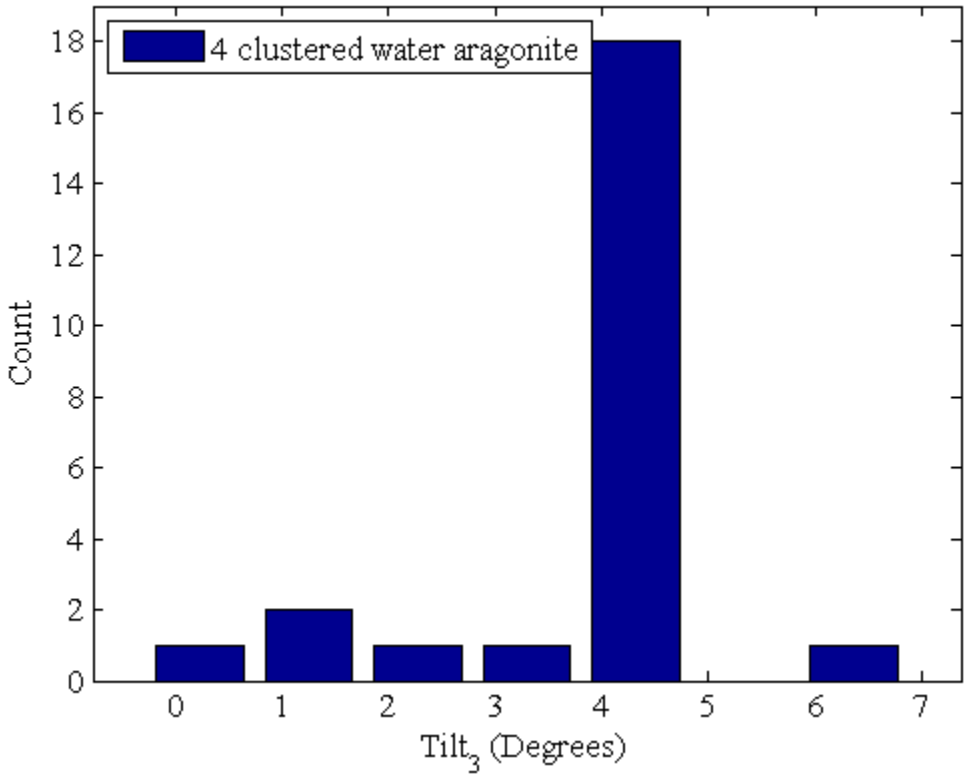

Figure 4.24: Carbonate $tilt_3$ histogram in 4 clustered H_2O molecules impurities in aragonite system after relaxation. Refer to figure (4.5) for definition of $tilt_3$.

4.3.4 Distortion of calcium sub-lattice for Aragonite

In the perfect aragonite crystal the Ca-Ca nearest neighbor distance is 3.89 $\AA$. Figure (4.25) shows the Ca sub-lattice distortion of an aragonite supercell with 4 clustered H_2O impurities after relaxation. In figure (4.26) the Ca-Ca nearest neighbor distance distribution is shown for the above mentioned system. Maximum, minimum, mean and the standard deviation of Ca-Ca nearest neighbor distances from all the configurations are presented in table (4.11). From the same table we observe that the Ca sub-lattice distortion is systematically less for Mg substitution than for H_2O insertion, exactly like in Calcite. In fact for Mg substitution the magnitude of distortion is very similar to that calculated for calcite, whereas for H_2O substitution calcite the supercells are more

distorted. Though this is the general trend observed here, we cannot be conclusive due to the limited amount of data.

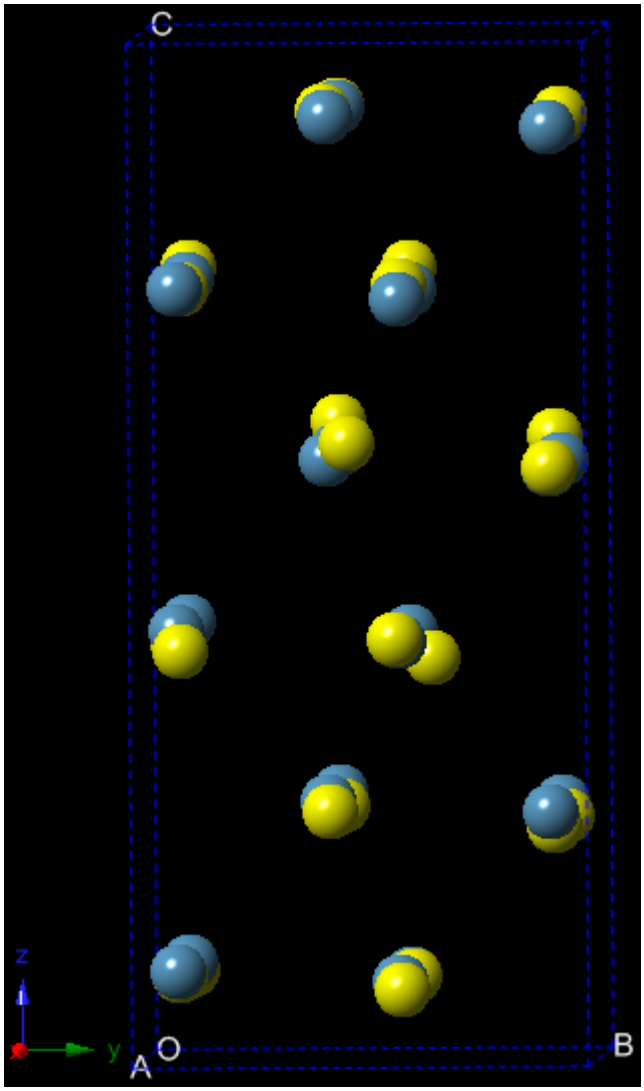

Figure 4.25: Ca sub-lattice in 4 clustered H_2O molecules as impurities in aragonite system. The color blue and yellow represents the Ca ion positions before and after relaxation. Notice more distortion (compare with figure (4.17)) near the middle of the cell where H_2O molecules were inserted.

Configuration	Max NND ($\AA$)	Min NND ($\AA$)	Mean NND ($\AA$)	Std. Dev NND ($\AA$)
3 clustered H_2O	4.19	3.85	3.98	0.12
4 clustered H_2O	4.18	3.62	3.97	0.18
4 scattered H_2O	4.19	3.77	3.98	0.12
5 scattered H_2O	4.20	3.70	3.91	0.16
6 clustered Mg	4.10	3.72	3.93	0.13
6 scattered Mg	4.10	3.72	3.92	0.12

Table 4.11: Ca-Ca nearest neighbor distance in aragonite.

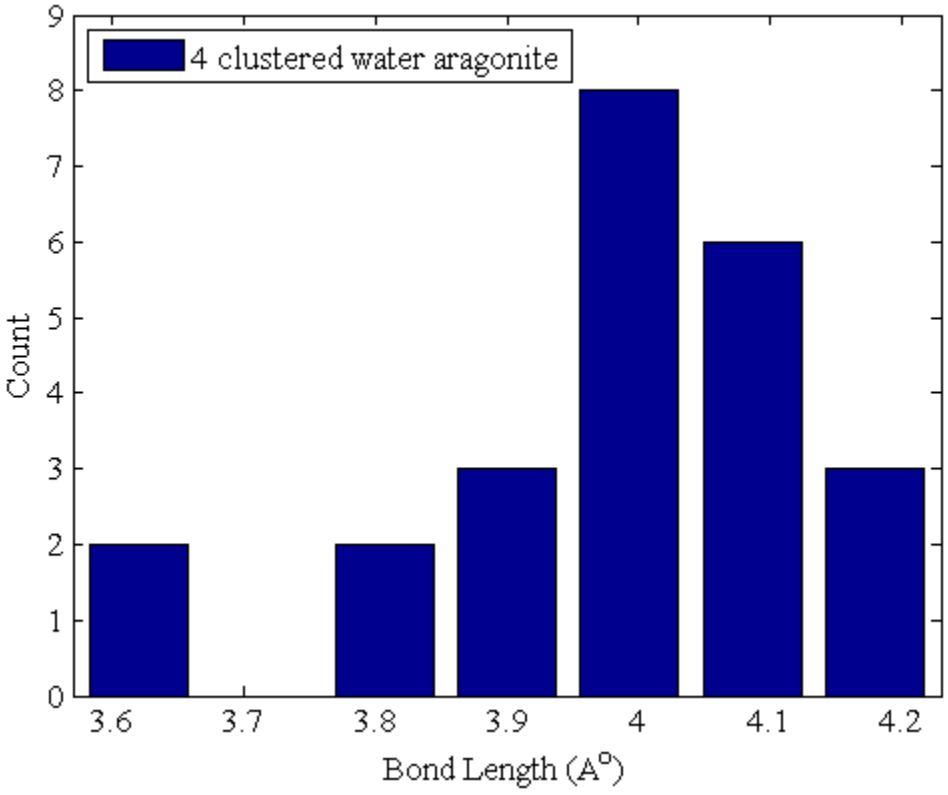

Figure 4.26: Ca-Ca nearest neighbor distance distribution in 4 clustered H_2O molecules impurities in aragonite system after relaxation.

Chapter 5

MODELING OF AMORPHOUS CALCIUM CARBONATE

5.1 Hypothesis Regarding Amorphization of $CaCO_3$

From the results in previous section we observe that the main effects of introducing impurities are carbonate plane tilts and Ca sub-lattice distortion. Another thing to notice is that there 3 times as many O atoms as Ca atoms. Hence one could argue that carbonate tilts alone should suffice to produce ACC. But it should be remembered that the Ca electron scattering factor is almost twice as high as the scattering factor for C [111, 112]. Hence both carbonate tilts and Ca sub-lattice distortion could have comparable effects on generating an amorphous diffraction pattern. One would expect that the effect of the carbonate tilts would be more prominent because the total number of O atoms is 3 times that of Ca atoms. These facts led us to hypothesize that, "Tilts and distortions in $CaCO_3$ crystal can lead to a diffraction pattern that appears to come from an amorphous material".

The above hypothesis is the basis of the work which will be presented in section 5.4 and 5.5 below. To model an ACC structure we use a multi-scale modeling scheme where carbonate tilts and Ca sub-lattice distortions mechanisms will be used to generate atomic positions in a much larger (limited by the computation ability $\sim 100 \times 100 \times 170\ (\mathring{A})^3$) supercell. It should be noted that we do not want to repeat the same distortion, because that will generate long range order in a big crystal which will lead to diffraction spots/peaks. Hence our approach will be to build the giant supercell by randomly sampling from the distortion distributions we obtained from the relaxed structures, rather than just repeating the relaxed structure in 3 dimensions.

5.2 Carbonate Tilts in Terms of Polar and Azimuthal Angles (θ, ϕ)

To build a model system with a larger cell with the distribution in whole-carbonate plane tilts, it was necessary to express the tilt_{CO_3} angles (refer section 4.3.1 for definition) in terms of θ, an angle with respect to '**c**' axis and ϕ, an angle with respect to '**a**' axis for mathematical convenience. Hence we converted the tilt angles to spherical-polar coordinates (i.e. θ and ϕ). The idea of this conversion is shown in the cartoon in figure (5.1). In this sketch **a**, **b** and **c** are the supercell lattice vectors and n is the normal vector to the carbonate planes ($\mathbf{n}_{CO_3}$ in figure (4.5)). θ represents the tilt of the CO_3 planes and ϕ is their azimuthal rotation. These θ and ϕ distributions were used for sampling the carbonate tilts in the diffraction code. The range of θ and ϕ for each configuration of calcite and aragonite systems are presented in table (5.1) and (5.2).

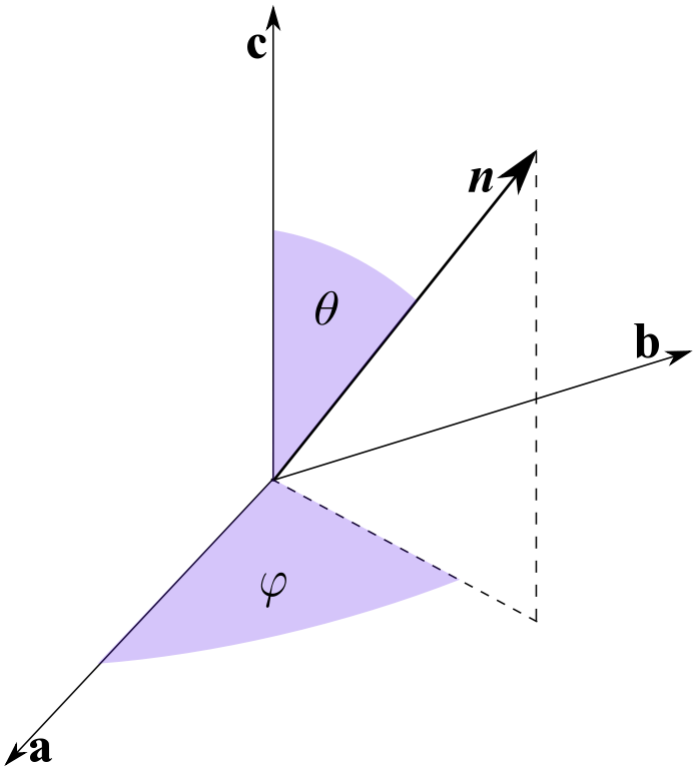

Figure 5.1: Conversion of tilt angles to the polar angle θ and azimuthal angle ϕ.

Configuration	θ Range (Degree)	ϕ Range (Degree)
3 clustered H_2O	0.92 - 24.93	-81.10 - 80.82
4 clustered H_2O	0.63 - 23.97	-77.24 - 77.29
4 scattered H_2O	2.41 - 26.24	-89.60 - 83.40
5 clustered H_2O	1.34 - 38.42	-76.69 - 85.82
6 clustered Mg	0.03 - 5.00	-85.05 - 70.65
6 scattered Mg	0.78 - 7.69	-88.69 - 86.97

Table 5.1: Range of θ and ϕ distributions for simulated calcite supercell with impurities.

Configuration	θ Range (Degree)	ϕ Range (Degree)
3 clustered H_2O	0.09 - 33.69	-88.87 - 84.90
4 clustered H_2O	0.54 - 29.29	-80.91 - 67.02
4 scattered H_2O	0.10 - 32.99	-75.21 - 88.24
5 clustered H_2O	1.05 - 67.88	-65.67 - 89.68
6 clustered Mg	0.56 - 6.14	-89.76 - 86.38
6 scattered Mg	0.94 - 6.95	-88.47 - 86.14

Table 5.2: Range of θ and ϕ distributions for simulated aragonite supercell with impurities.

The range of θ from table (5.1) and (5.2) suggest that carbonate planes tilt can be as big as $\sim 40^\circ$ for calcite and $\sim 70^\circ$ for aragonite, due to the introduction of impurities. Regarding the ϕ range it should be mentioned that we have not resolved the sense of the normal vector **n** along the '**c**' axis. This degeneracy restricts ϕ to -90° to +90°. Resolving the degeneracy one would expect that ϕ will span the whole range of $0^\circ - 360^\circ$ because in both the calcite and aragonite supercells the CO_3 planes are stacked between Ca-planes along the '**c**' axis (refer to figure (4.2) and (4.4)) hence should be free to rotate azimuthally about '**c**'. For this reason we have used the full circular range for ϕ (both for calcite and aragonite) in our indigenous diffraction code. We have used

the maximum value of the θ range (different for calcite and aragonite) to model the tilt angle distribution in our code.

5.3 Modeling of Amorphous Calcium Carbonate (ACC)

We used a multi-scale modeling scheme1 to develop the ACC structure using the distributions of θ, ϕ and Ca-Ca nearest neighbor distance (NND). The Ca-Ca NND distributions for calcite and aragonite were shown in figure (4.16) and (4.26) respectively. Figures (5.3) and (5.4) show the θ distributions for selected calcite and aragonite systems. We used the best linear fit to this distribution for sampling θ in our diffraction code. Distributions for ϕ for the same selected systems are presented in figure (5.5) and (5.6). Because the CO_3 planes are free to rotate in the azimuthal direction we used a uniform distribution for sampling ϕ in the diffraction code. Below we shall explain the concept of random sampling of a quantity weighted by its probability distribution function, as this technique will be used to sample θ and ϕ for modeling ACC.

5.3.1 Random Sampling from a Distribution

Let us assume that we want to randomly sample a quantity x between x_{min} and x_{max} weighted by its probability distribution function (PDF) $f(x)$. Figure (5.2) depicts the idea behind this sampling [112]. First the PDF should be normalized to 1 by using equation (5.1),

$$C' \int_{x_{\min}}^{x_{\max}} f(x)dx = 1. \tag{5.1}$$

The normalized PDF is shown as the blue curve in figure (5.2). Next the cumulative distribution function (CDF) of this normalized PDF has to be generated by using equation (5.2),

$$CDF = C' \int_{x_{\min}}^{x'} f(x)dx \tag{5.2}$$

The red curve in figure (5.2) represents the CDF. Now equating a random number R, drawn uniformly between 0 and 1, to the CDF will correspond to a unique value of x′ through the upper limit in CDF integral i.e.,

$$R = C' \int_{x_{\min}}^{x'} f(x)dx \tag{5.3}$$

Hence using equation (5.3) we can obtain x=x′, depending on the value of R. In next few sections this idea will be exploited to sample θ and ϕ (i.e. carbonate tilts) from their respective distributions to develop our model for ACC

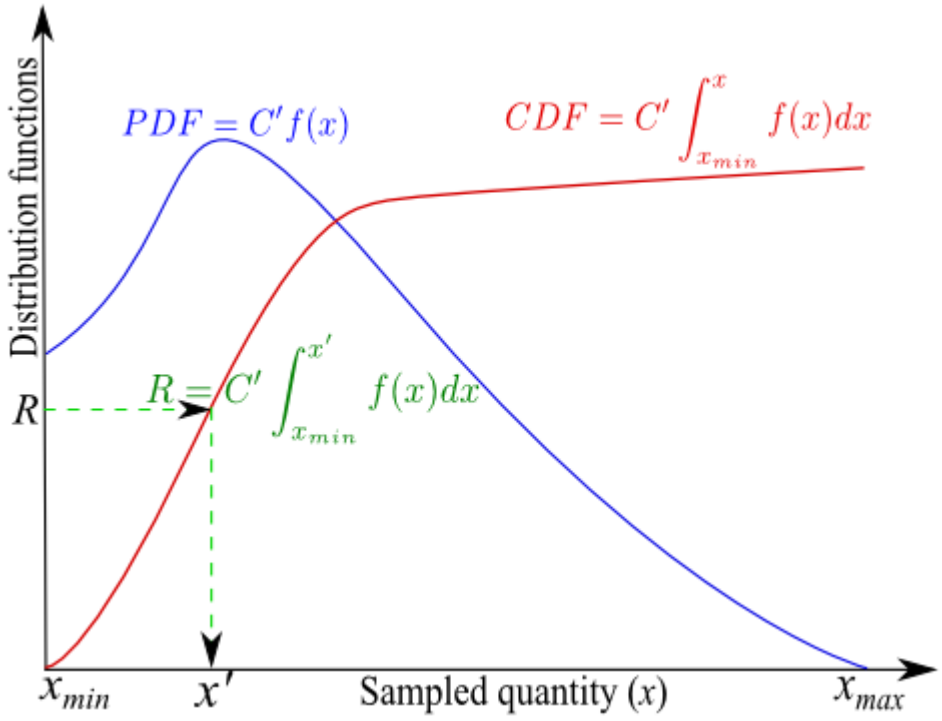

Figure 5.2: Schematics of randomly sampling from a distribution $f(x)$. The blue curve is the normalized PDF of x and red curve is the corresponding CDF. R is a random number drawn from the uniform distribution between 0 to 1.

5.3.2 Random Sampling from the θ Distribution

In the diffraction code we extract θ by equating a random number (R), drawn uniformly between 0 to 1, to the normalized cumulative distribution of the straight line fits (i.e. model distribution function for tilts). Distributions of θ and best linear fits for the 5 clustered H_2O calcite and 4 clustered H_2O aragonite systems are shown in Figure (5.3) and (5.4) respectively.

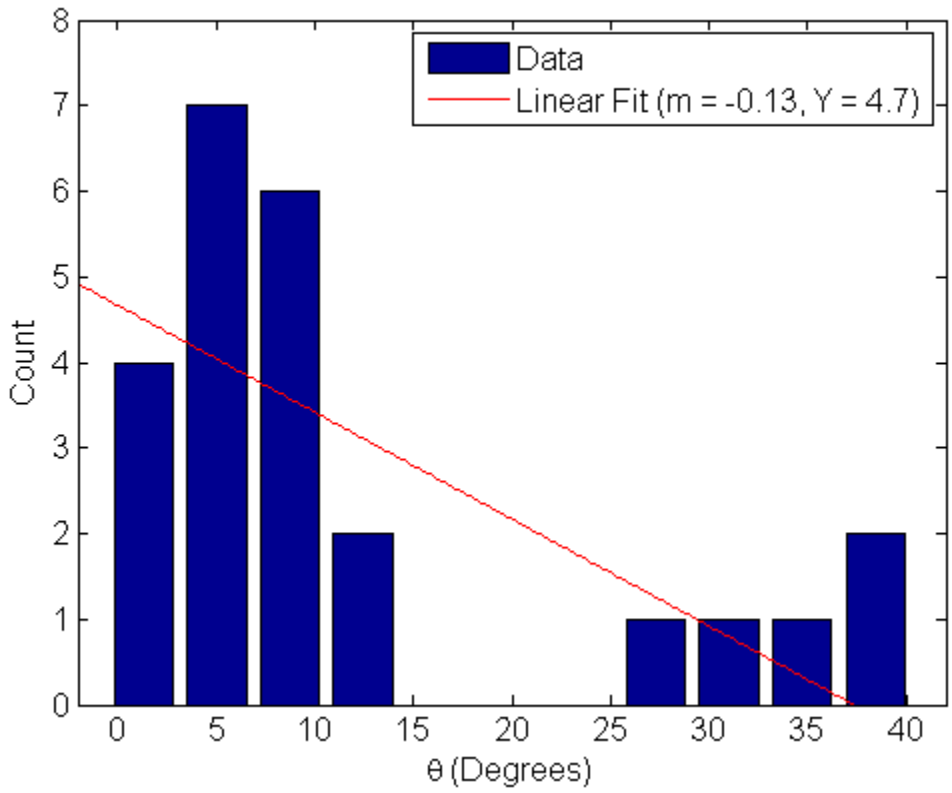

Figure 5.3: θ distribution and its best linear fit for 5 clustered H_2O molecules as impurities in calcite system after relaxation.

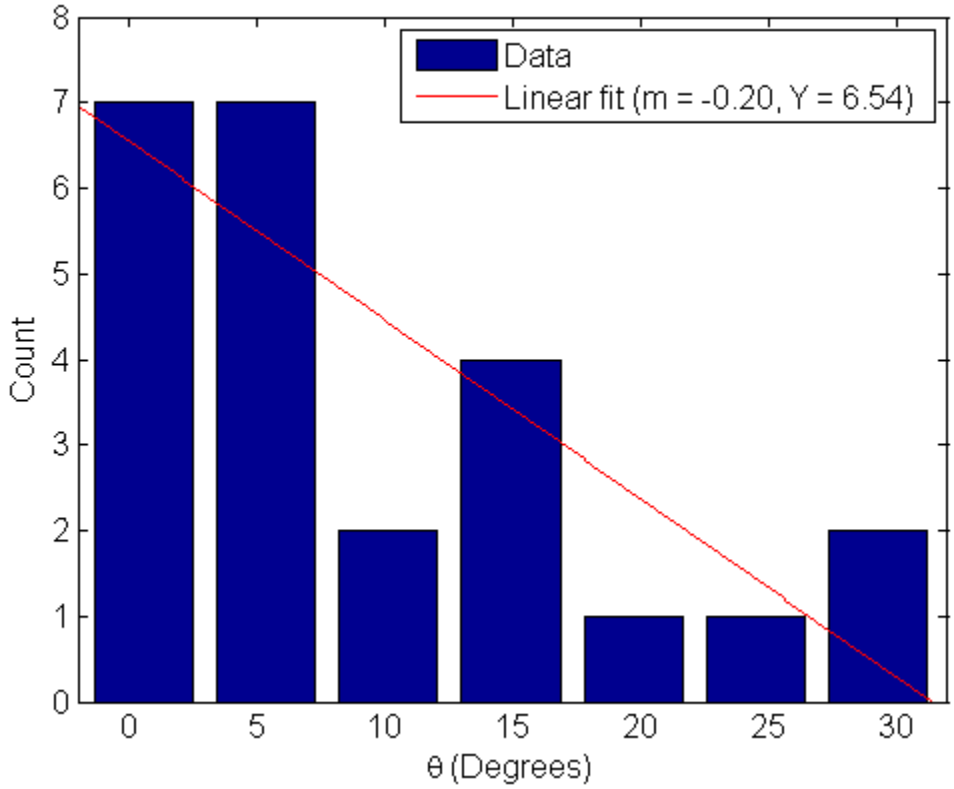

Figure 5.4: θ distribution and its best linear fit for 4 clustered H_2O molecules as impurities in aragonite system after relaxation.

It should be noted that θ is the polar angle which is measured from the '**c**' axis of the crystal lattice. Given that higher θ means bigger tilts one should expect that the distribution should fall off with increasing θ . This can also be seen in figures (5.3) and (5.4). We certainly do not have enough data or any theoretical estimate to predict how the distribution should vary as a function of θ; hence we chose the simplest straight line fit through the data and use its slope (m) and Y-intercept (Y) as two parameters of our model for the variation of θ. The parameter values used in our diffraction code are tabulated in table (5.3).

The mathematical steps for sampling from the linear distributions in figure (5.3) and (5.4) are presented below.

θ - Distribution function:

$$f(\theta) = m\theta + \mathrm{Y};\ \text{where}\ \ 0 \leq \theta \leq \theta_{\max} \tag{5.4}$$

Normalization:

$$C' \int_0^{\theta_{\max}} f(\theta)\, d\theta = 1 \rightarrow C' = \frac{1}{\left[\frac{1}{2} m\theta_{\max}^2 + \mathrm{Y}\theta_{\max}\right]}. \tag{5.5}$$

We equate R to the CDF of the model function for θ (i.e. straight line) i.e,

$$C' \int_0^{\theta'} [m\theta + \mathrm{Y}] d\theta = R \tag{5.6}$$

Integrating equation (5.6) yields a quadratic equation in θ,

$$\frac{1}{2} m\left(\theta'\right)^2 + \mathrm{Y}\theta' - \frac{R}{C'} = 0. \tag{5.7}$$

Solving the quadratic equation (5.7) we get,

$$\theta' = \frac{-\mathrm{Y} \pm \sqrt{\mathrm{Y}^2 + 2m\left(R/C'\right)}}{m} \tag{5.8}$$

5.3.3 Random Sampling from the ϕ Distribution

If we observe CO_3 group orientations in the calcite or aragonite structures in figure (4.2) and (4.4) respectively, we should note that the carbonate planes are stacked along the '**c**' axis and Ca ions are symmetrically placed around that plane. This suggests that carbonate planes are free to rotate azimuthally (i.e. in the direction of ϕ). The ϕ distributions for calcite and aragonite respectively are shown in figure (5.5) and figure (5.6), where we can see this more clearly.

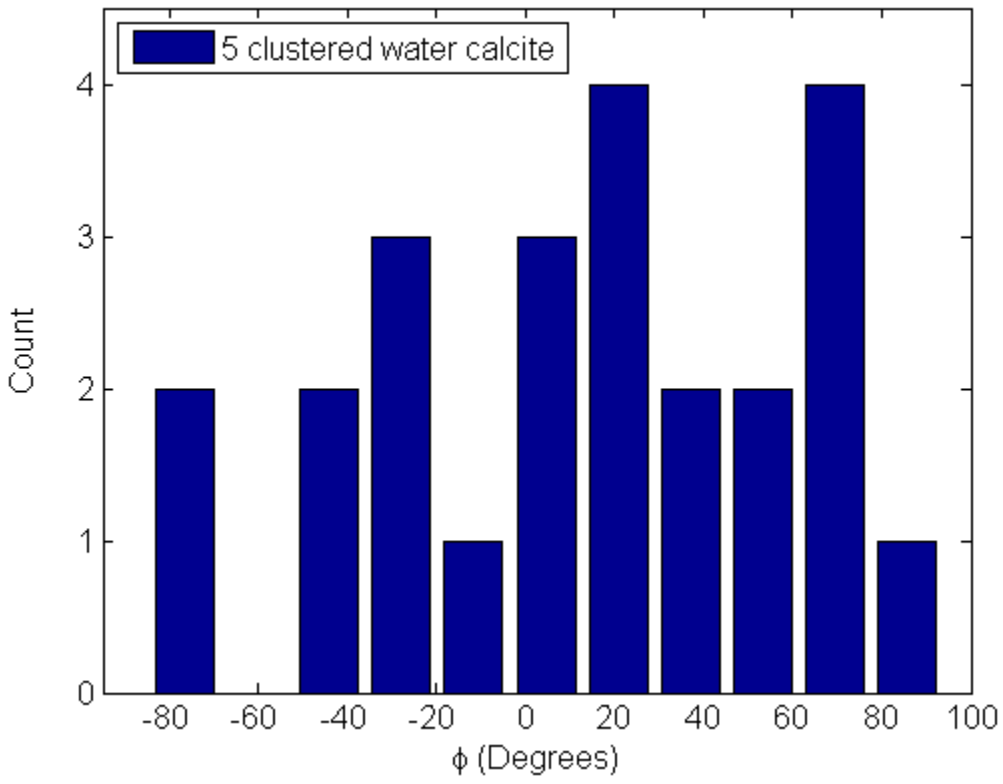

Figure 5.5: ϕ distribution for 5 clustered H_2O molecules + calcite system after relaxation.

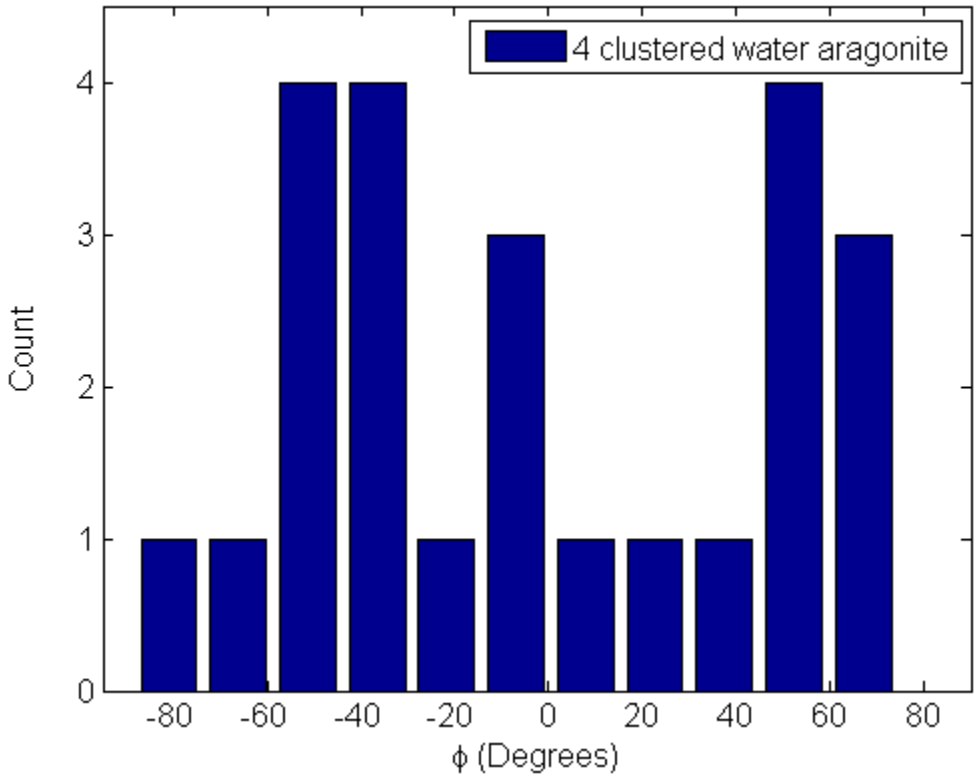

Figure 5.6: ϕ distribution for 4 clustered H_2O molecules + aragonite system after relaxation.

The ambiguity of semi-circular range (i.e. -90° to + 90°) rather than the whole 360° in these figures was explained in section 5.2. We took ϕ as a uniform distribution and the parameter values are tabulated in table (5.3). Because ϕ is a uniform distribution, sampling becomes trivial and shown in the following steps.

Normalized ϕ - Distribution function: $f(\phi)$=1; where $0^\circ \leq \phi \leq 360^\circ$. Hence,

$$\phi' = R \cdot 360^\circ \tag{5.9}$$

Crystal	$\theta_{max}(^\circ)$	$\theta_{min}(^\circ)$	$\phi_{max}(^\circ)$	$\phi_{min}(^\circ)$	Y	m
Calcite	38.42	0.0	360	0.00	3.00	-0.62
Aragonite	67.88	0.0	360	0.00	5.50	-0.17

Table 5.3: Model parameters for the carbonate tilts

We should mention here that the maximum value of θ_{max} among all the impurity configurations was chosen for both calcite and aragonite, to enhance the effect of carbonate tilts. The parameters for the θ distribution i.e. m and Y were chosen as the average of all impurity configurations in both calcite and aragonite system. For ϕ, as argued in section (5.2), we took the whole 360° range. It was assumed that ϕ was uniformly distributed over the whole range

5.3.4 Sampling from Ca-Ca Nearest Neighbor Distance (NND) Distribution

Table (4.7) and (4.11) shows the Ca-Ca nearest neighbor distance distribution for different impurity configurations in calcite and aragonite respectively. One would expect these distributions would peak in the vicinity of the actual nearest neighbor distances (for calcite it is 4.05 $\AA$, for aragonite 3.89 $\AA$) while large deviations from the peak occur near the impurity atoms or inserted water molecules. We observed this behavior in Ca-Ca NND distribution in figure (4.16) and (4.26) of chapter 4, for the systems selected above; 5 clustered H_2O in calcite and 4 clustered H_2O in aragonite. Once again we do not have enough data to conclusively determine the shape of the distribution but it is reasonable to assume that the distribution is peaked about the actual bond length. For this reason we chose a Gaussian with a cut-off. For calcite we set the cutoff at 0.81 $\AA$ which is 20% of the original Ca-Ca nearest neighbor distance, and for aragonite it was set at 27% (i.e. 1.05 $\AA$) of the original Ca-Ca nearest neighbor distance. Another reason for choosing a Gaussian is that it is well studied and there are plenty of scientific library routines available for randomly sampling from a Gaussian distribution, called Gaussian

deviate. In our code we used GNU Scientific Library (GSL) routine 'gsl_randist' [113] for this purpose. We do not present the mathematics as it is well documented in the literature [112], but the idea is simple and can be easily understood once again from figure (5.2) where the distribution function $f(x)$ is a bell shaped Gaussian curve with a hard cutoff.

We studied the Ca-Ca sub-lattice deformation separately from tilts. The way we model the system is following. We choose a Ca atom in the crystal and randomly sample a deviation for each crystal lattice direction from the characteristic Gaussian and move the atom accordingly from its original position. As we mentioned, the deviations can be as large as 0.81 $\AA$ in the case of calcite and 1.05 $\AA$ for aragonite. If these distortions can produce ACC, one would expect that a crystal $5\times5\times5$ times bigger than the original supercell prepared in this way would lose the correlation in Ca positions. Hence some signature of randomness should be expected for such a crystal. This argument is also valid for CO_3 tilts. However, so far we have assumed that the carbon atoms have not moved from their original positions which might lead to a small contribution to the original crystalline diffraction peaks. We chose the model supercell $10\times10\times10$ the original supercell ($9.98\times9.98\times17.06$ $\AA^3$). We shall discuss the effect of these distributions on powder diffraction pattern of calcite and aragonite in the following section.

Though the carbonate groups are not distorted much, there could still be a distribution in the positions of the C atoms, which we did not calculate. Just to see the effect of C sub-lattice distortion we prepared another system $10\times10\times10$ times the original supercell, where in addition to carbonate tilts and Ca sub-lattice distortions we also distorted C sub-lattice by the same amount as the Ca sublattice, i.e. 20% for calcite and 27% for aragonite. The diffraction profile of this system will also be discussed in the following section.

5.4 Effects of Distortions on Calcite Diffraction Line Profile

To see the effect of the above mentioned distortion mechanisms, individually as well as in combination, we compare the calculated diffraction profiles one by one with the perfect calcite or aragonite diffraction pattern. We superimposed perfect crystal diffraction peaks (red) on top of the modeled diffraction line profiles (blue) to directly compare possible amorphization in the modeled crystals. It should be mentioned that in all the cases below we matched the maximum peak heights for both (modeled and pure) to put them on same scale. This however should not matter since we are interested in the peak width rather than the peak height.

5.4.1 Carbonate Tilts Only

A $10\times10\times10$ replica of the original calcite supercell of volume $99.8\times99.8\times170.6\,\AA^3$, containing 120,000 atoms, was created with its C and Ca sub-lattice intact but the carbonate planes were tilted according to the tilt distributions described in section (5.3.2) and (5.3.3). The powder diffraction line profile (blue) of such a crystal is presented along with perfect calcite diffraction peaks (red) in figure (5.7). It can be seen here that there are not many differences between both the two plots except some peaks (e.g. 0.63°) are missing in crystal modeled with carbonate tilts. Two additional tiny peaks appear near the main peak at 0.47°. To see the effect of tilts in more details we plot the same data on semi-log (y axis as log scale) plot in figure (5.8).

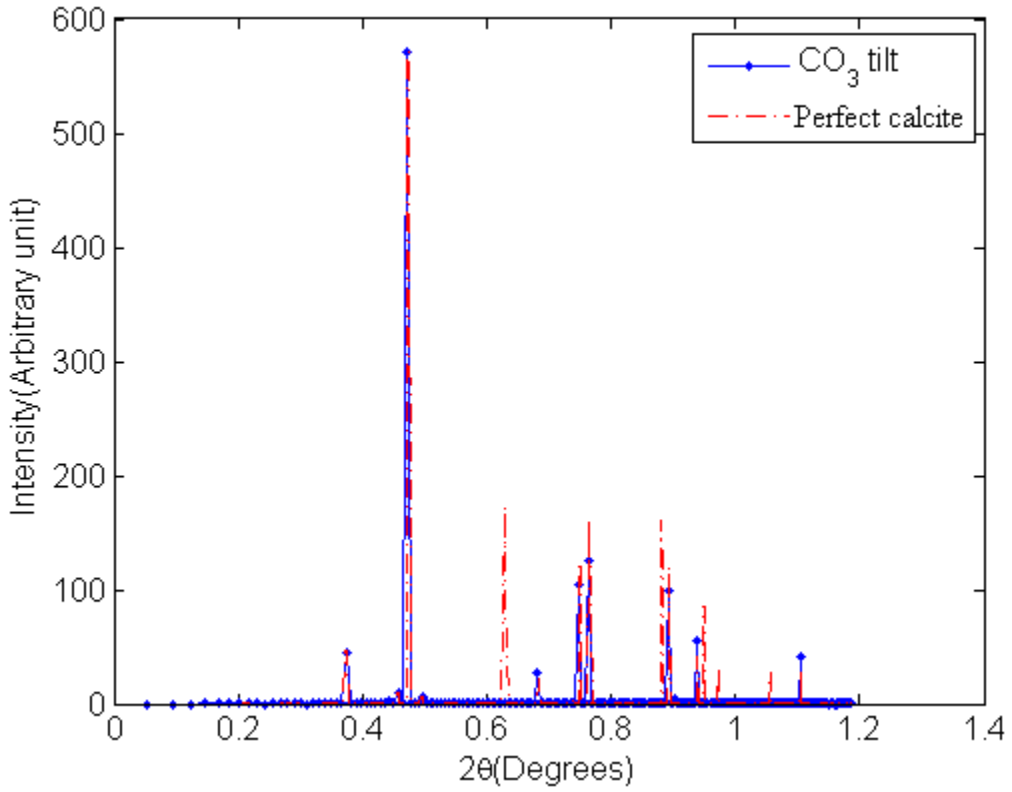

Figure 5.7: Powder diffraction line profile of a $\sim 100 \times 100 \times 170$ $\mathring{A}^3$ calcite crystal containing only carbonate tilts.

We can clearly see here that there are many more data points for the crystal with carbonate tilts than for the perfect crystal. However their magnitude is so small that it is simply not sufficient to produce broad diffraction peaks that would be expected for an amorphous material. Hence we can conclusively rule out the possibility that the carbonate tilt mechanism in calcite alone makes the crystal appear amorphous as far as diffraction is concerned.

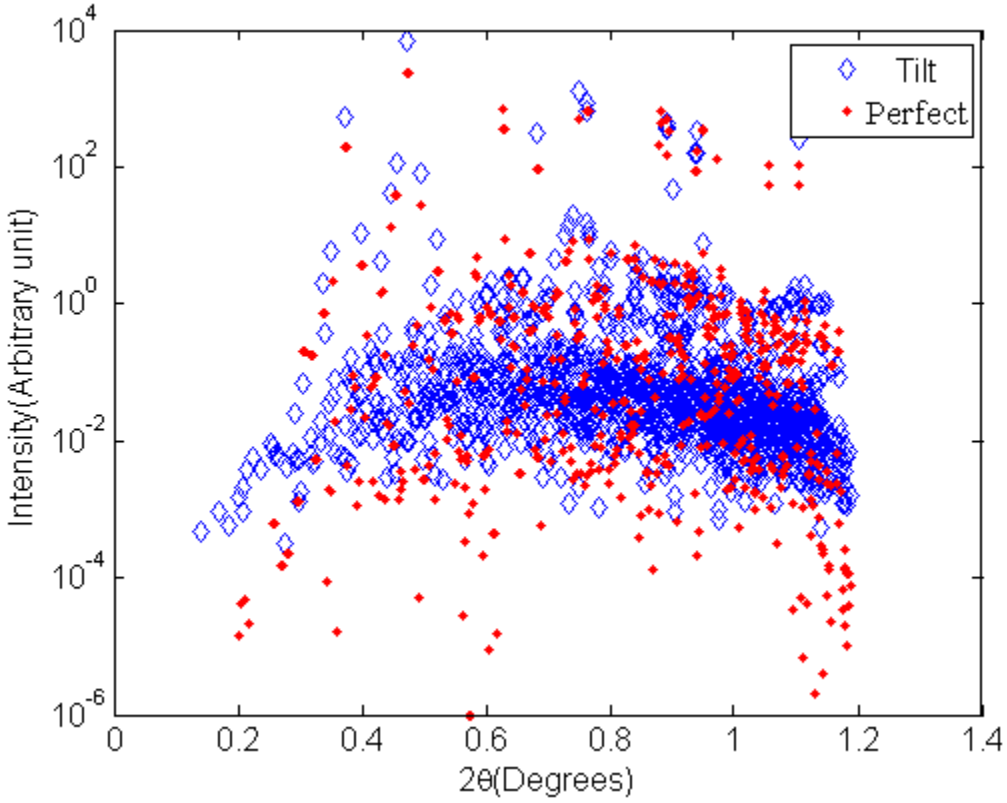

Figure 5.8: Semi-log plot of figure (5.7) to show the small diffraction peaks.

5.4.2 Ca-Ca Sub-lattice Distortion Only

Here a $99.8 \times 99.8 \times 170.6\ \AA^3$ calcite crystal containing 120,000 atoms was created, now with its all the carbonate group positions intact but with the Ca sub-lattice distorted according to the distribution discussed in section 5.3.4. The powder diffraction profile of this system is presented in figure (5.9). Once again we can see here that there is not much effect from the introduction of a Ca sub-lattice distortion. In fact the effect of this disturbance is smaller than CO_3 tilts which is expected because the combined O scattering factor is actually a little greater than the Ca scattering factor [96, 97]. We plot the same data in a semi-log plot in figure (5.10) to observe if there is any effect at all. We indeed see there are many more tiny peaks appearing like in the case of CO_3 tilt but

again they are not sufficient to produce an amorphous diffraction pattern. So here too we can conclusively rule out the possibility that the Ca sub-lattice distortion mechanism can alone make a perfect calcite crystal appear amorphous. Both the above results raises serious questions as to whether these mechanisms actually can ever produce a model for ACC.

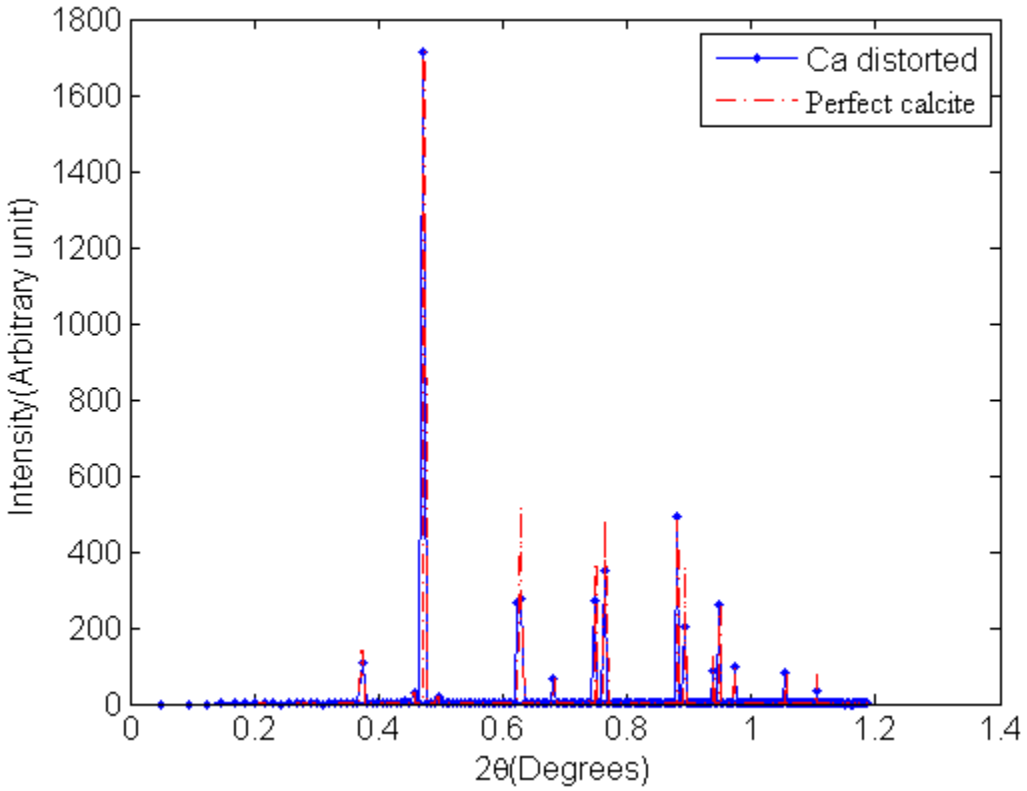

Figure 5.9: Powder diffraction line profile of a $\sim 100 \times 100 \times 170$ $\mathring{A}^3$ Calcite crystal containing only Ca sub-lattice distortion.

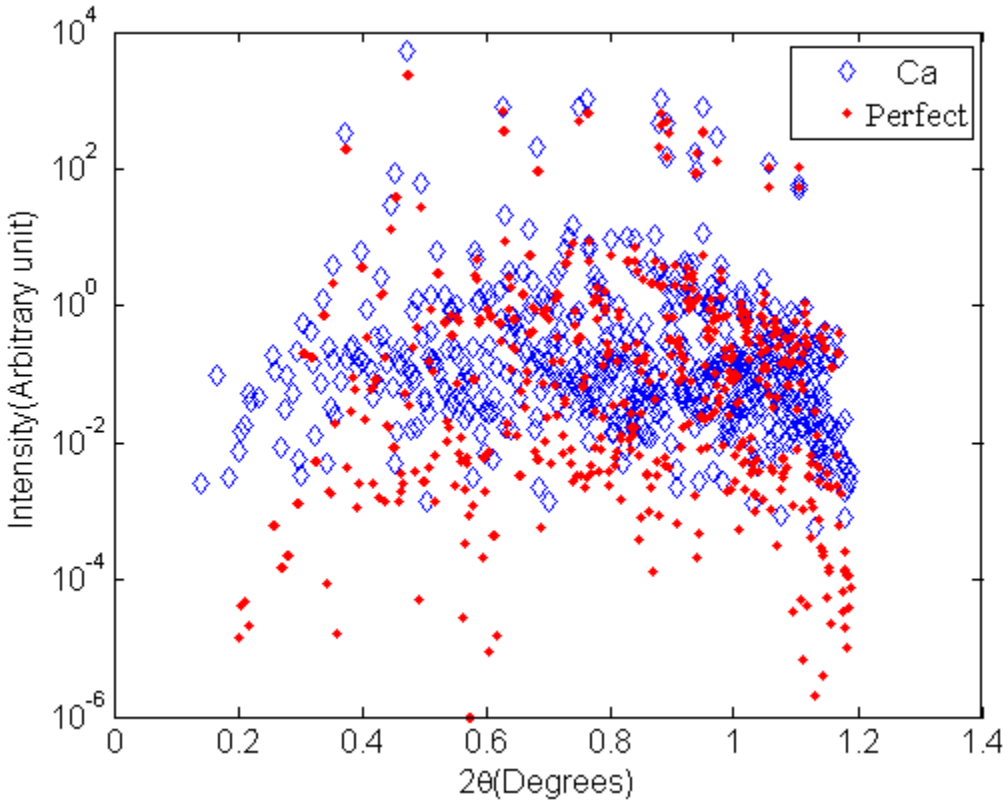

Figure 5.10: Semi-log plot of figure (5.9) to zoon the small diffraction peaks.

Below we will be examining two more cases. The first is where, CO_3 tilts and Ca sub-lattice distortions are introduced together and the second is where C sub-lattice distortions are introduced in addition to carbonate group tilts and Ca sub-lattice distortions.

5.4.3 Carbonate Tilts and Ca Sub-Lattice Distortion

Another calcite crystal of volume $\sim 99.8 \times 99.8 \times 170.6\, \mathring{A}^3$, containing 120,000 atoms was created where we had introduced both CO_3 tilts and Ca sub-lattice distortions according to the distributions mentioned in section (5.3). The powder diffraction line profile of this modeled crystal is presented in figure (5.11). It should be noticed that there are more differences from the perfect calcite diffraction pattern than in the previ-

ous two cases. Some of the crucial peaks like the one at 0.63° have almost vanished and the relative intensities of other peaks are diminished. In spite of all these it still does not resemble an amorphous diffraction pattern. Plotting the vertical axis on a log scale (not shown here) does not reveal much. This result does not surprise us given what we have seen in the previous two cases because we know that the scattering factors combining both Ca and O are merely of same order as the individual scattering factors. So if scattering from Ca and O separately does not produce an ACC diffraction profile we should not expect that the combination would be any more effective.

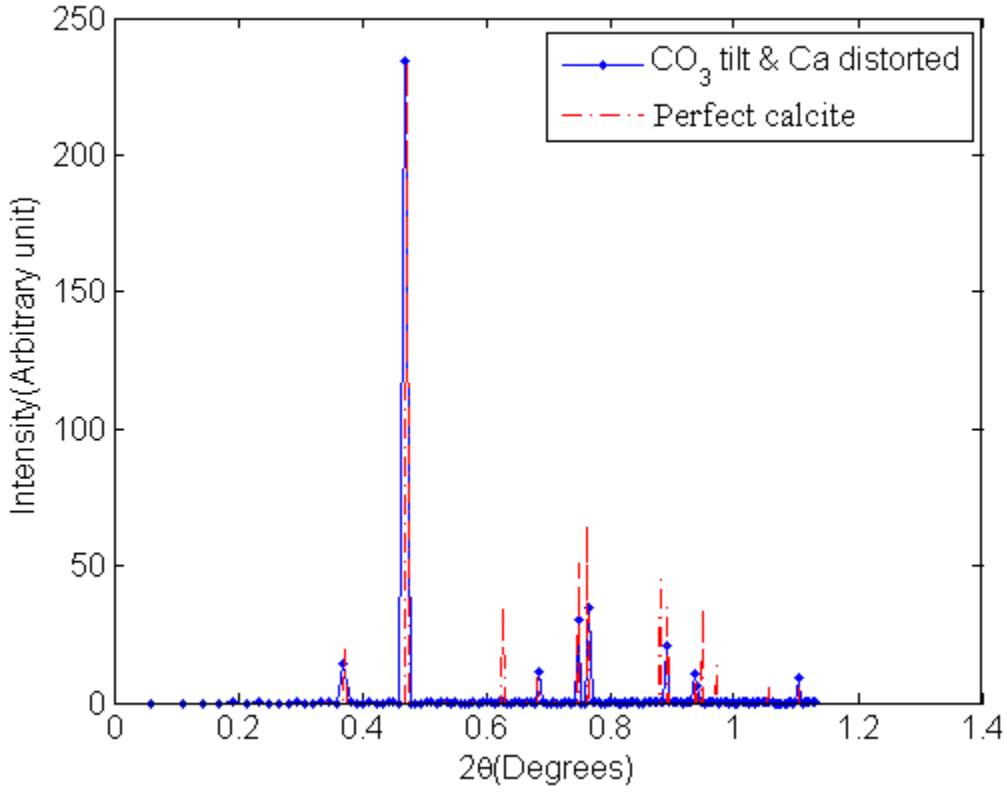

Figure 5.11: Powder diffraction line profile of a $\sim 100 \times 100 \times 170$ $\AA^3$ calcite crystal containing CO_3 tilts + Ca sub-lattice distortion.

5.4.4 Carbonates Tilts, Ca and C Sub-lattice Distortions

Here a $99.8 \times 99.8 \times 170.6\ \mathring{A}^3$ calcite crystal containing 120,000 atoms was created where we have introduced the combination of CO_3 tilts and Ca and C sub-lattice distortions according to the distributions described in section (5.3). The powder diffraction line profile from this model is shown in figure (5.12). Not surprisingly, here also we do not see much difference from the previous case. It is pretty clear from the above studies that CO_3 tilts, Ca and C sub-lattice distortions are not capable of producing a model for ACC starting with a Calcite structure.

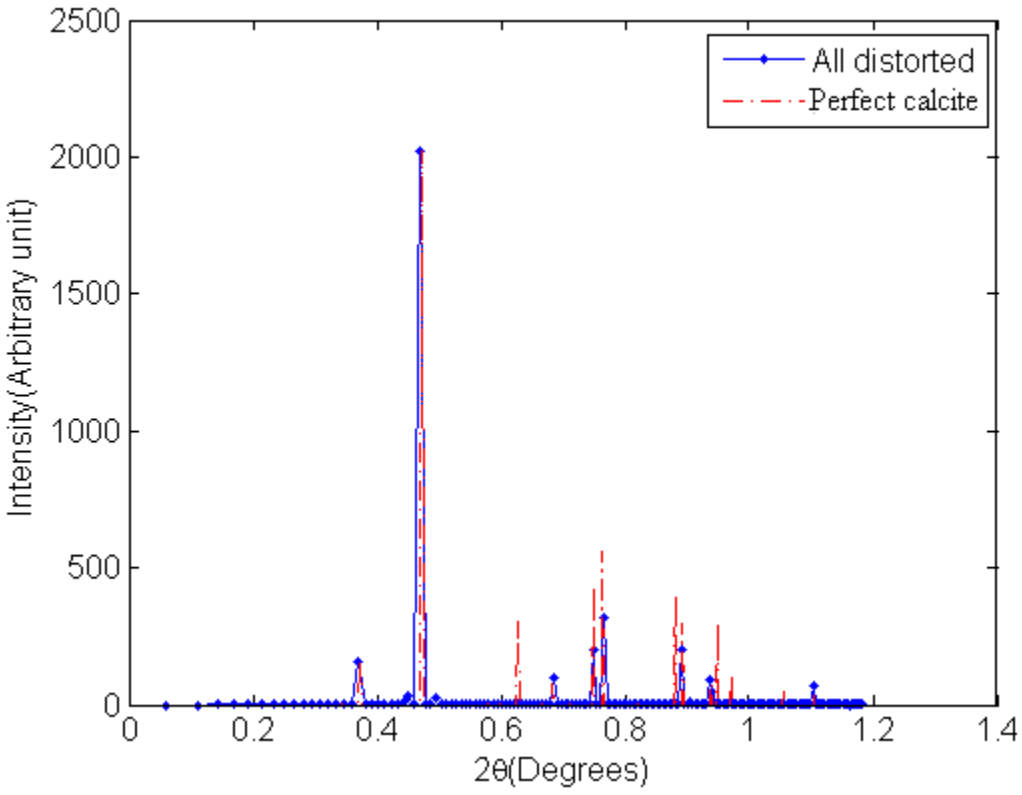

Figure 5.12: Powder diffraction line profile of a $\sim 100 \times 100 \times 170\ \mathring{A}^3$ calcite crystal with CO_3 tilts, C and Ca sub-lattice distortion.

5.5 Effects of Distortions on Aragonite Diffraction Line Profile

Following the arguments of previous section on calcite we would be surprised if the introduction of above mentioned distortion mechanisms in the aragonite structure generates an amorphous diffraction pattern. The only new factors for Aragonite are lower symmetry than Calcite and slightly higher density. The density of aragonite [114] is 2.93 gm cm^{-3}, $\sim 8\%$ greater than calcite [115] whose density is 2.71 gm cm^{-3}. These differences encourage us to study the effects of all the mentioned distortion mechanisms in the aragonite supercell.

5.5.1 Carbonate Tilts Only

A $99.2 \times 79.8 \times 172.2$ $\mathring{A}^3$ aragonite crystal, $10 \times 10 \times 10$ times the size of original Aragonite supercell, containing 120,000 atoms was created with its C and Ca sub-lattice intact but the carbonate planes were tilted according to the tilt distributions described in section (5.3.2) and (5.3.3). The calculated powder diffraction line profile (blue) for such a crystal is presented along with perfect aragonite diffraction peaks (red) in figure (5.13). It can be seen that there are few differences between both the plots, except some peaks (e.g. 0.65°) are missing in the modeled crystal and the relative intensity of the significant peaks is somewhat different.

In spite of these differences here also carbonate plane tilts do not make an amorphous diffraction profile, similar to calcite. To see the effects of CO_3 tilts in more detail we plotted the same data on a semi-log scale in figure (5.14). Here also we notice that CO_3 tilts are actually not doing much, though some small deviations are noticeable. In general, it enhances the smaller peaks, but certainly not enough to make an amorphous diffraction profile. Once again we can confidently rule out the possibility that the CO_3 tilt mechanisms can produce amorphous aragonite.

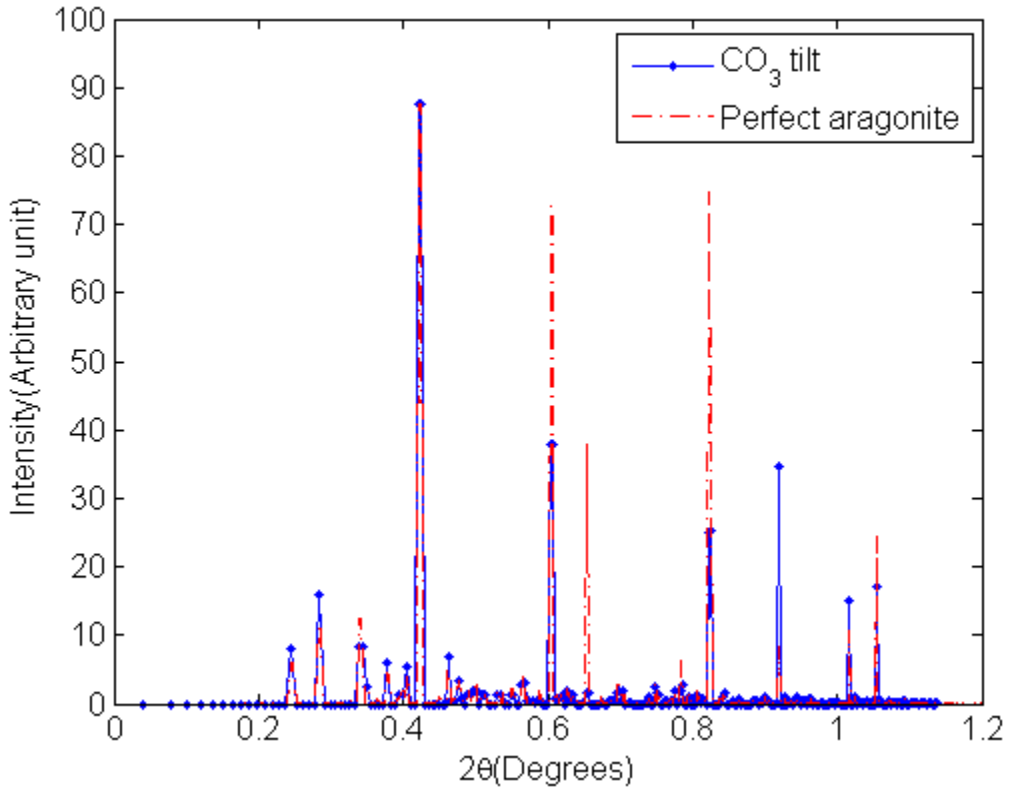

Figure 5.13: Powder diffraction line profile of a $\sim 100 \times 80 \times 170\ \mathring{A}^3$ aragonite crystal containing only carbonate tilts.

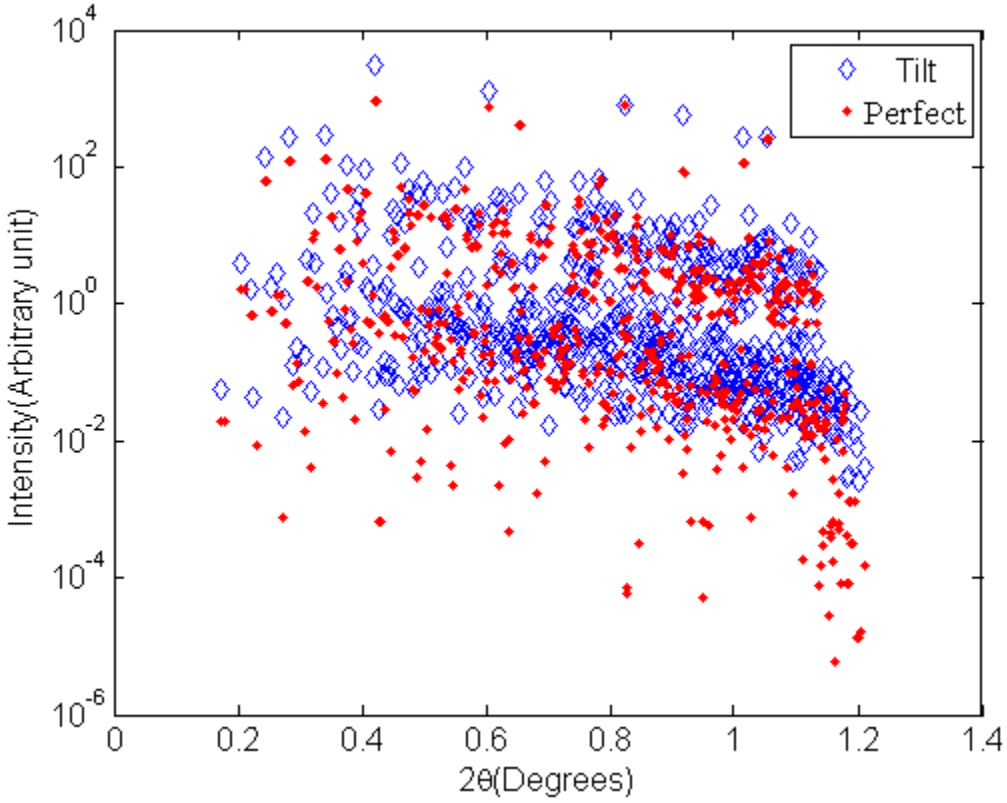

Figure 5.14: Semi-log plot of figure (5.13) to zoom the small diffraction peaks.

5.5.2 Ca Sub-lattice Distortion Only

Another $99.2 \times 79.8 \times 172.2\ \AA^3$ aragonite crystal containing 120,000 atoms was created with all the carbonate groups' orientation intact but this time the Ca sub-lattice was distorted according to the distributions discussed in section 5.3.4. The powder diffraction profile for this system is presented in figure (5.15). Again we can see here that there is even less effect from the introduction of the Ca sub-lattice distortion than from CO_3 tilts. We plot the same data in semi-log plot in figure (5.16) to emphasize small changes. We do not see any trend towards an amorphous diffraction pattern. In this case also we can conclusively rule out the possibility that the Ca sub-lattice distortion mechanism

alone can make a pure aragonite crystal amorphous. These results are consistent with the findings for calcite.

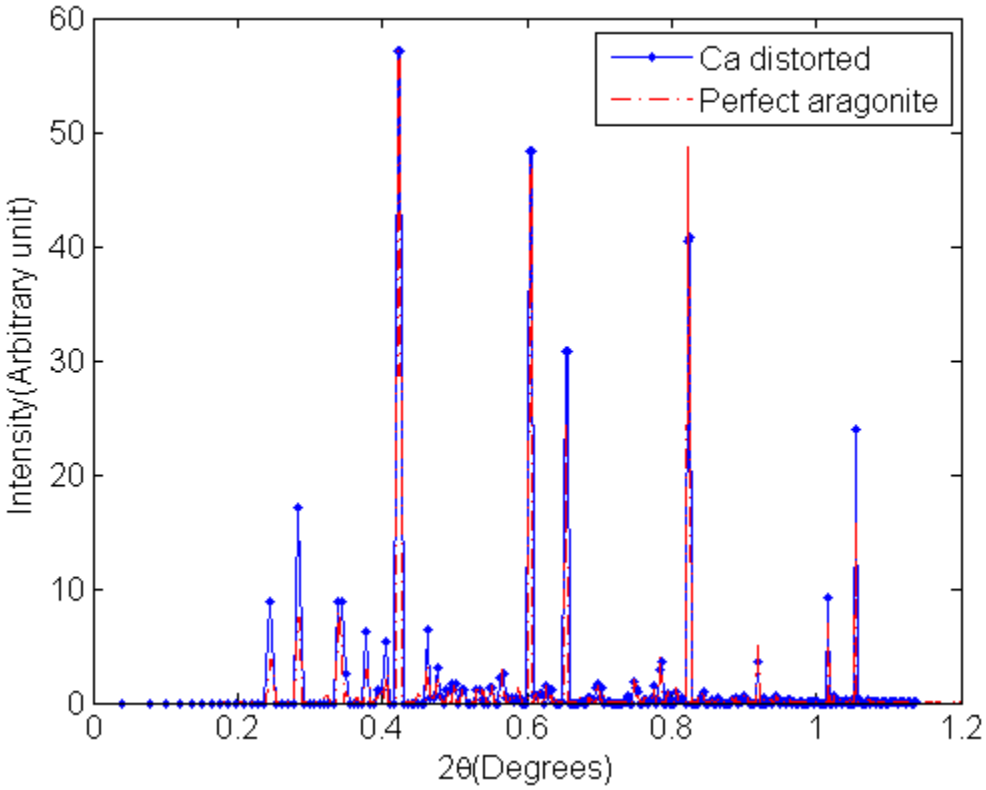

Figure 5.15: Powder diffraction line profile of a $\sim 100 \times 80 \times 170$ $\mathring{A}^3$ aragonite with only Ca sub-lattice distortion.

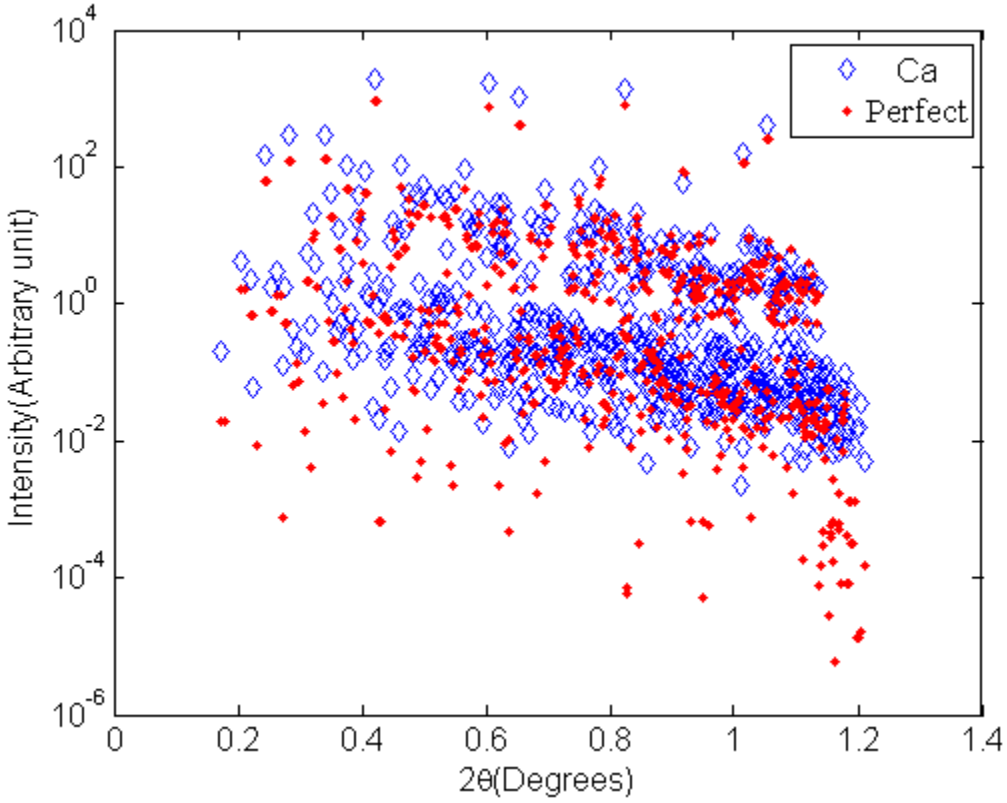

Figure 5.16: Semi-log plot of figure (5.15) to zoom the small diffraction peaks.

5.5.3 Carbonate Tilts and Ca Sub-Lattice Distortion

A $99.2 \times 79.8 \times 172.2\ \AA^3$ aragonite crystal containing 120,000 atoms was created where we now introduced both CO_3 tilts and a Ca sub-lattice distortions according to the distributions mentioned in section (5.3). The calculated powder diffraction line profile is presented in figure (5.17). As with calcite, the combination of carbonate tilts and Ca sub-lattice distortions is not sufficient to create a structure that gives an amorphous diffraction pattern, though it should be noticed that there are more differences between this pattern and the pure Aragonite diffraction pattern when compared with the previous two cases,. Some of the crucial peaks such as the peak at 0.65° are missing and the

relative intensities of other peaks are diminished in general. Nevertheless, we can also discard these combined mechanisms in aragonite as a candidate for an ACC model.

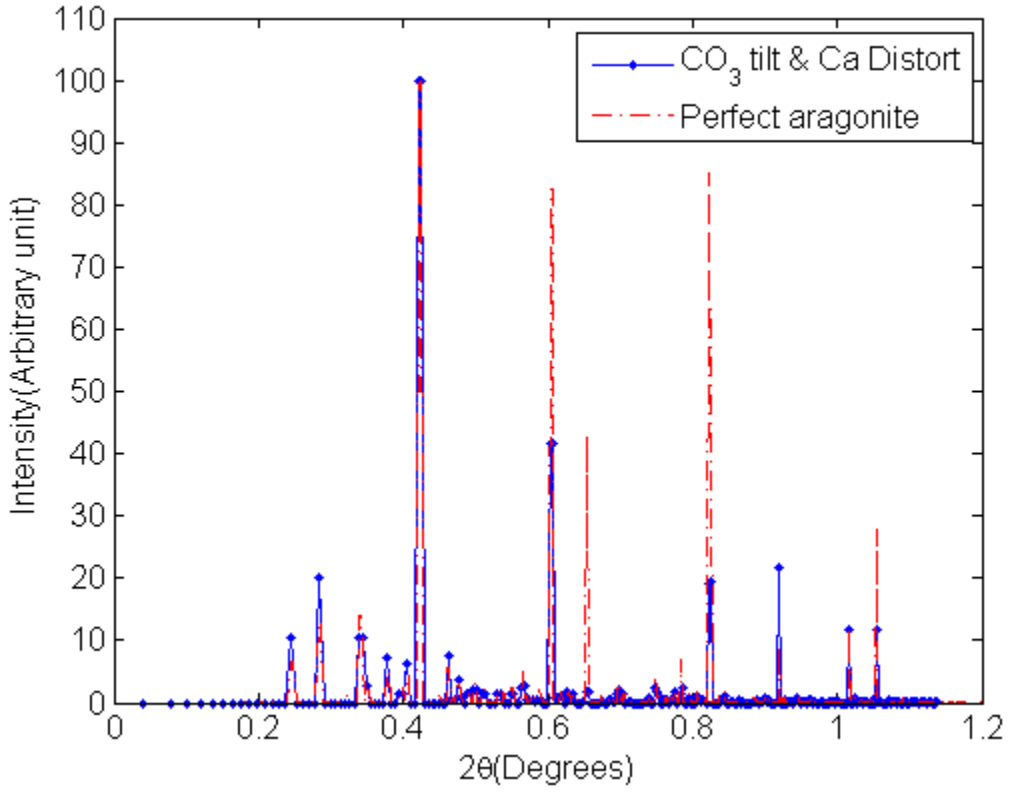

Figure 5.17: Powder diffraction line profile of a $\sim 100 \times 80 \times 170\ \AA^3$ aragonite crystal with CO3 tilts + Ca sub-lattice distortion.

5.5.4 Carbonate Tilts Combined with Ca and C Sub-lattice Distortions

Finally another Aragonite crystal of $10 \times 10 \times 10$ times original supercell, containing 120,000 atoms and of volume $99.2 \times 79.8 \times 172.2\ \AA^3$ was created where we introduced CO_3 tilts and distortions of both the Ca and C sub-lattices, according to the distributions mentioned in section (5.3). The powder diffraction line profile of this model is shown in figure (5.18). Not surprisingly we do not see much difference from the previous cases

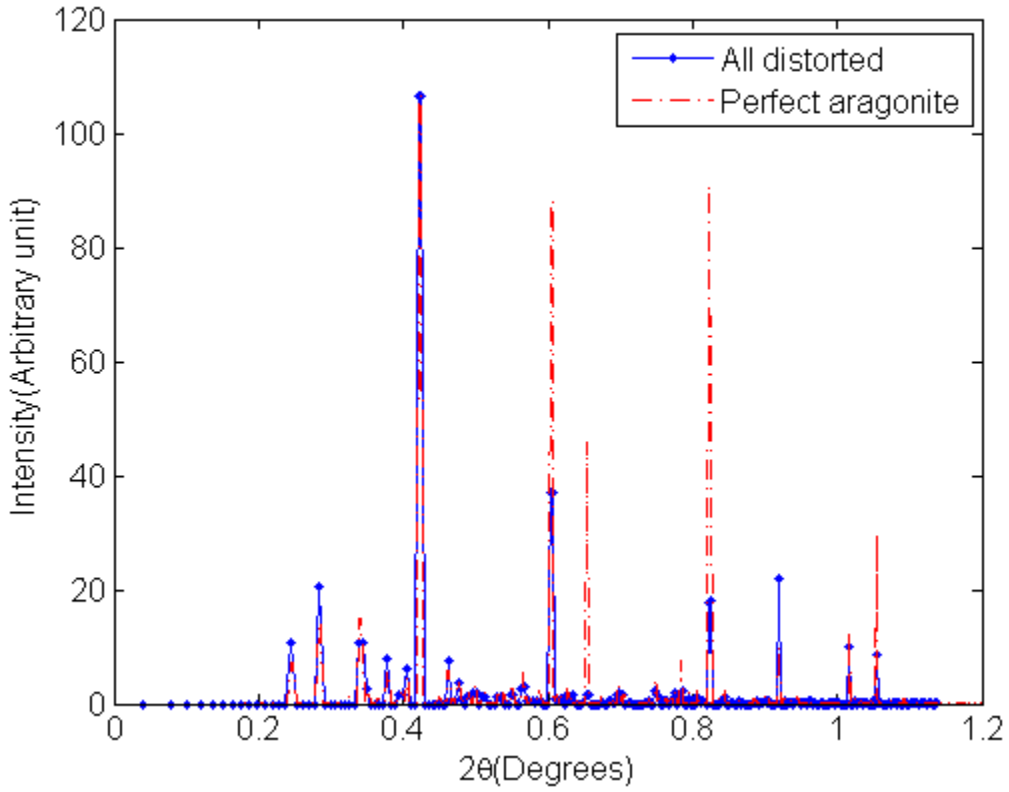

Figure 5.18: Powder diffraction line profile of a $\sim 100 \sim 80 \sim 170\, \mathring{A}^3$ aragonite crystal with CO_3 tilts + Ca sub-lattice distortion + C sub-lattice distortion.

5.6 Discussions and Evaluation of the Hypothesis

From the study in section (5.4) and (5.5) it is quite clear that as far as diffraction pattern of amorphous calcium carbonate is concerned, it cannot be created by merely introducing CO_3 tilts, Ca and C sub-lattice distortion in the crystal, either individually or in combination. This brings us back to the same question again as to how can we generate an ACC diffraction pattern starting from any form of $CaCO_3$ either calcite or aragonite.

An alternative hypothesis is that the amorphous diffraction pattern is the result of diffraction from nano-crystallites. We saw in chapter (3) that the smaller the crystal, the broader its shape function becomes. But the question is what should be the size

of such a nano-crystallites whose broad shape functions would swamp all the sharp features in diffraction line profile. Recent pair distribution function analysis [38] on high energy X-ray scattering spectra of ACC reveals some short and intermediate range structural coherence up to $\sim 15\ \mathring{A}$. This is very interesting as our original supercells are of the same size. In next chapter we shall investigate the effect of shape function and crystallite size on the diffraction profile.

Chapter 6

ACC AS NANO-CRYSTALLITES

The hypothesis that the ACC is composed of nano-crystallites is based on the fact that nano-crystals produce broad diffraction patterns, unlike the sharp features from large single crystals, due to their wide shape transformation. In this section we shall study the diffraction patterns of calcite and aragonite nano-crystallites. As the name suggests, the size of these crystals is $\sim$ nanometer and these may or may not contain defects and distortions. We shall study the diffraction line profile of various sized nano-crystallites and the effect of distortions on this profile to observe whether any of these can produce a diffraction profile resembling that from an amorphous material.

6.1 Diffraction Profile of the Calcite Nano-Crystallites

The results for the perfect calcite nano-crystallites of various sizes will be presented in this section. The purpose of this exercise is to observe how the diffraction profile varies as we change the crystal size. We shall examine 1x, 2x and 3x the original hexagonal supercell, whose volume is $99.8 \times 99.8 \times 170.6\ \mathring{A}^3$. The reason behind choosing these sizes is some recent studies [33, 59] (refer to chapter 1, section 1.5) which found that calcium carbonate formation starts with the formation of prenucleation clusters of dimension of ~ 2 nm.

6.1.1 1x of calcite Supercell

A calcite nano-crystallite of volume $9.98 \times 9.98 \times 17.06\ \mathring{A}^3$, containing 120 atoms was constructed as a model of such a nano-crystallite. The powder diffraction profile (blue curve) for such a crystal is presented in figure (6.1). The perfect calcite diffraction profile (red dotted line) was also shown here on the same scale for comparison purposes. Here it can be immediately noticed how large the effect of nano-crystallite size is, com-

pared to all the deformation cases we studied in chapter 5. This diffraction profile truly resembles an amorphous one. The most important thing to notice is the position of the broad peaks. The biggest broad peak appears exactly at $2\theta = 0.47^{\circ}$ which is the highest characteristic peak corresponding to [01-4] plane in calcite. Another broad peak occurs at the vicinity of $2\theta = 0.7^{\circ}$. This result clearly suggests that this nano-structure could be a potential candidate for ACC.

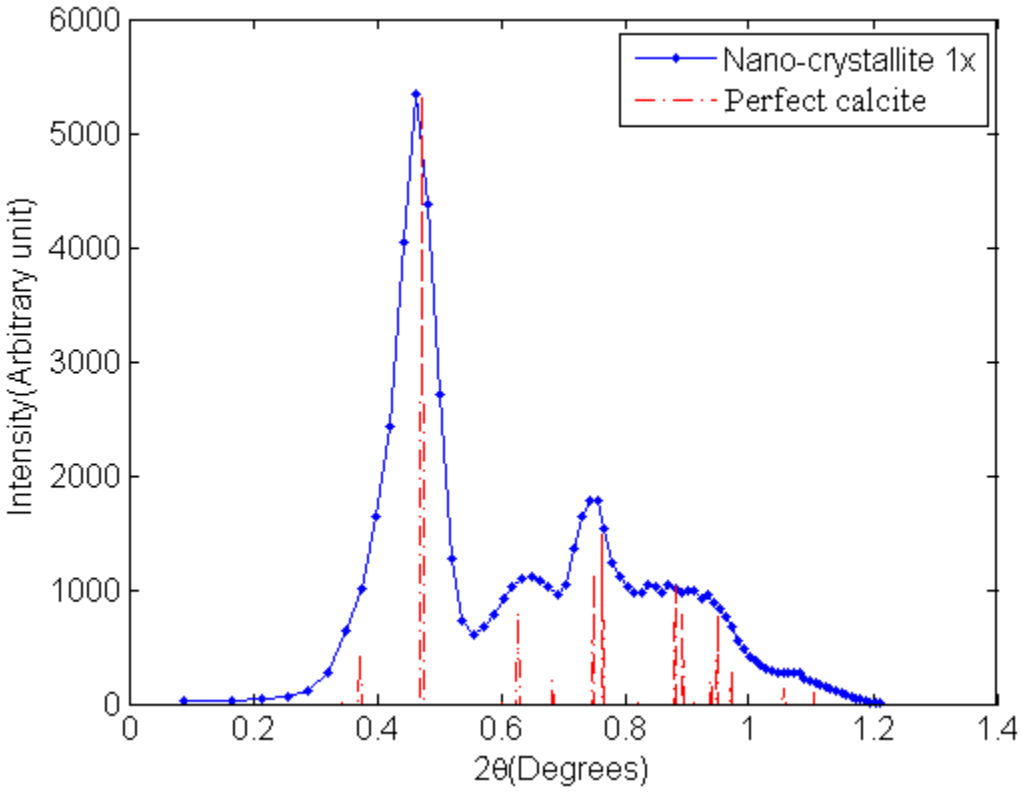

Figure 6.1: Powder diffraction line profile (blue) of a $\sim 10 \times 10 \times 17$ $\AA^3$ calcite nano-crystallite. Perfect crystal calcite diffraction line profile (red) was superimposed for comparison.

6.1.2 2x of calcite Supercell

A $19.96 \times 19.96 \times 34.12$ $\AA^3$ calcite crystal containing 240 atoms was constructed as a model of a nano-crystallite. The powder diffraction pattern for this crystal is presented

in figure (6.2). Comparing with figure (6.1) we can observe that the peak widths have shrunk considerably and the second broad peak at $2\theta \sim 0.7^\circ$ can be resolved into several peaks. This clearly suggests that the diffraction profile has started to resemble that from a macroscopic crystal and would probably not be classified as amorphous. Notice that the dimension of the crystallite structure is little more than 1.5 nm!

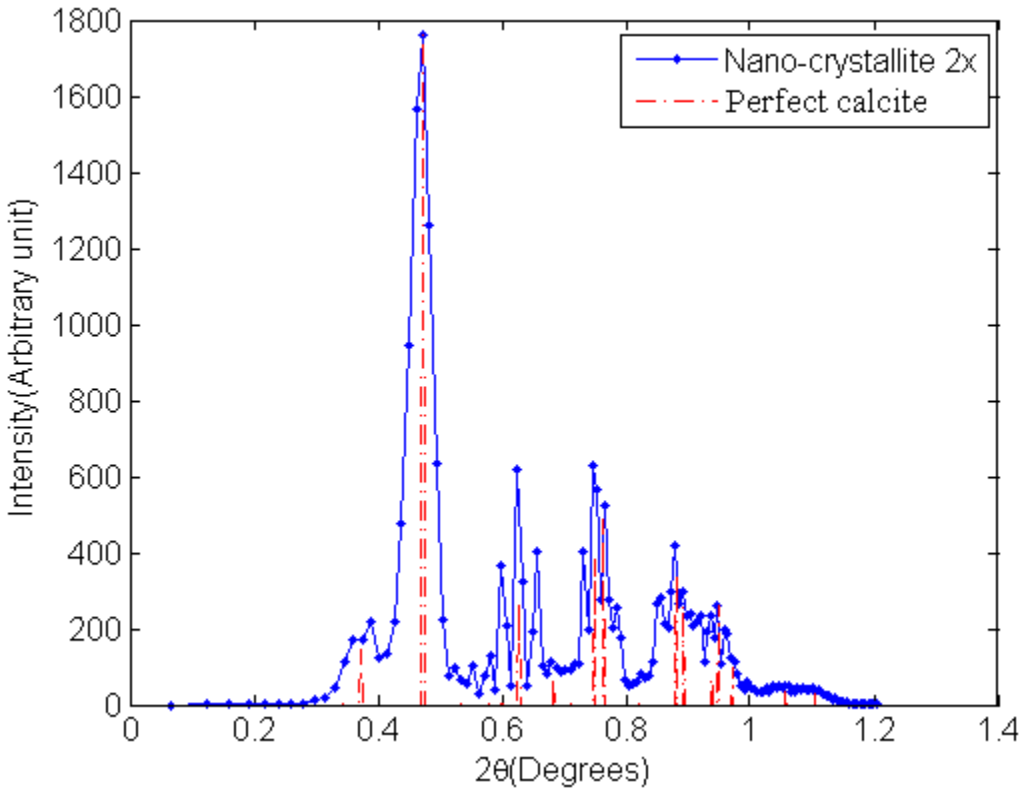

Figure 6.2: Powder diffraction line profile (blue) of a $\sim 20 \times 20 \times 35$ $\AA^3$ calcite nano-crystallite. Perfect crystal calcite diffraction line profile (red) was superimposed for comparison.

6.1.3 3x of calcite Supercell

A 29.94 $\times$29.94 $\times$ 51.18 $\AA^3$ calcite crystal containing 360 atoms was constructed as a model of a nano-crystallite. The powder diffraction profile for this particular crystal is presented in figure (6.3).

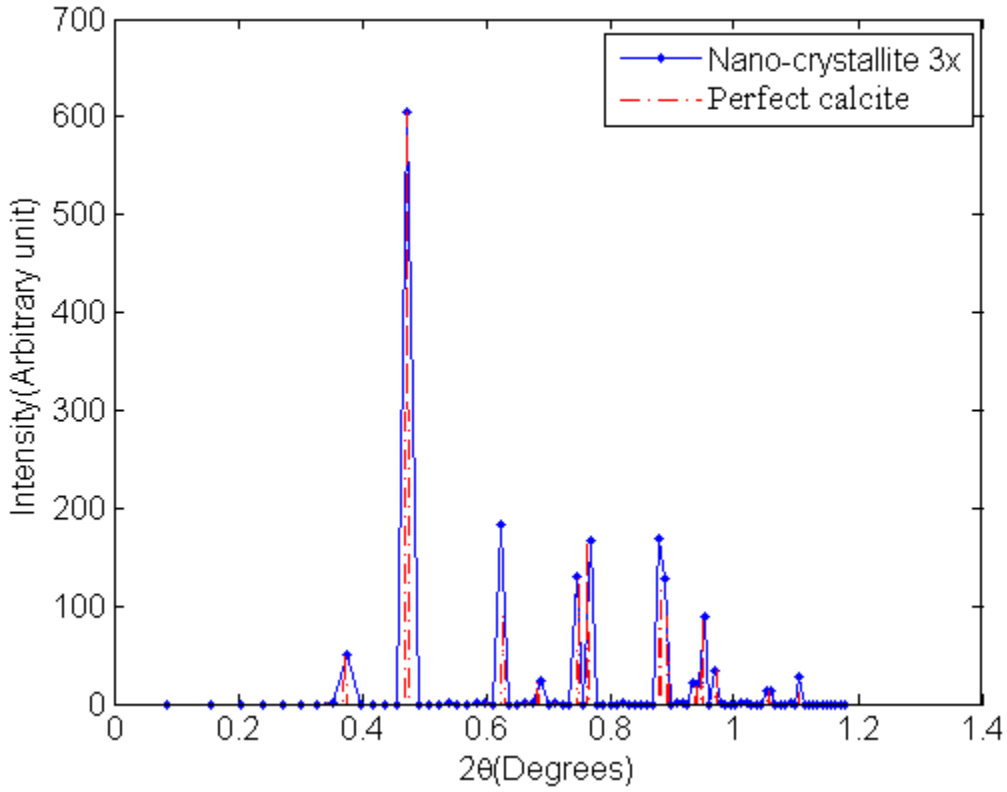

Figure 6.3: Powder diffraction line profile (blue) of a $\sim 30 \times 30 \times 50$ $\mathring{A}^3$ calcite nano-crystallite. Perfect crystal calcite diffraction line profile (red) was superimposed for comparison.

Comparing with figure (6.1) we can see this is no longer an amorphous diffraction pattern. The peak widths are very narrow and all the peaks can be easily resolved. This is very similar to diffraction from a perfect calcite crystal. This probably also answers why we were not able to generate amorphous diffraction pattern using a $\sim 100 \times 100 \times 170$ $\mathring{A}^3$ crystal in chapter 5 in spite of the introduction of many defects in the crystal.

In the above study one can clearly see how the calcite diffraction pattern goes from an amorphous to a crystalline pattern, as we vary the crystal sizes from $\sim 1 \times 1 \times 2$ nm^3 to $3 \times 3 \times 5$ nm^3. This result suggests that our hypothesis i.e. 'The ACC might be

composed of nano-crystallites' might be correct, and that the size of these crystallites is $\sim 1 \times 1 \times 2$ nm^3. This agrees with the claim of Pouget *et. al.* [33] that calcium carbonate crystal development starts with the formation of prenucleation clusters of dimension of $\sim 6 - 11$ $\mathring{A}$, and also explains why Michel *et. al.* [38] did not see any structural coherence in ACC beyond 15 $\mathring{A}$. In the next subsection we shall apply the same procedures on aragonite.

6.2 Diffraction Profile of the Aragonite Nano-Crystallites

Here we shall present the powder diffraction results for the aragonite nano-crystallites of various sizes to observe how the simulated diffraction profile changes with crystallite size . We shall again examine crystals that are 1x, 2x and 3x the original orthorhombic supercell that has dimensions $9.92 \times 7.98 \times 17.22$ $\mathring{A}^3$.

6.2.1 1x of aragonite Supercell

An aragonite nano-crystallite of volume $9.92 \times 7.98 \times 7.22$ $\mathring{A}^3$, containing 120 atoms was constructed as a model of a nano-crystallite. The powder diffraction pattern for such a crystal is presented in figure (6.4). Like calcite it should also be immediately noticed how large the effect of nano-crystallite size is compared to all the cases studied in chapter 5.

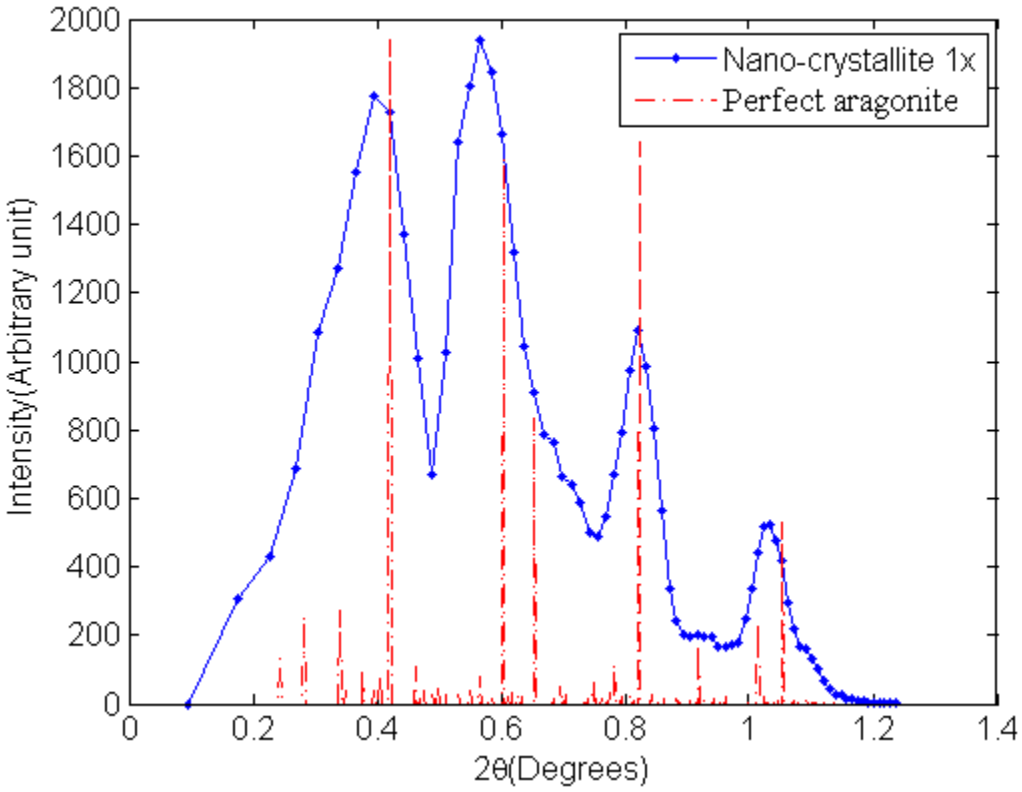

Figure 6.4: Powder diffraction line profile (blue) of a $\sim 10 \times 10 \times 20\,\mathring{A}^3$ aragonite nano-crystallite. Perfect crystal aragonite diffraction line profile (red) was superimposed for comparison.

This profile resembles an amorphous diffraction profile since we cannot identify the original aragonite peaks (red dotted line). Another important thing to notice is the position of the broad peaks. The couple of prominent broad peaks appear exactly at $2\theta = 0.42^\circ$ and 0.6° are characteristic peaks corresponding to (111) and (112) plane spacings in aragonite. From this result we can conclude this nano-structure could also be a candidate for ACC.

6.2.2 2x of aragonite Supercell

A $19.84 \times 15.78 \times 34.44\ \mathring{A}^3$ aragonite crystal containing 240 atoms was constructed as a model of such a nano-crystallite. The powder diffraction pattern for this crystal is presented in figure (6.5). Comparing with figure (6.4) we can see that the peak widths have diminished and the broad peaks are just starting to be resolved into narrow peaks. This clearly suggests that the diffraction profile has started to show more features characteristic of macroscopic crystals but still resembles an amorphous diffraction profile. Notice once again, the dimension of the crystallite is little more than 1.5 nm!

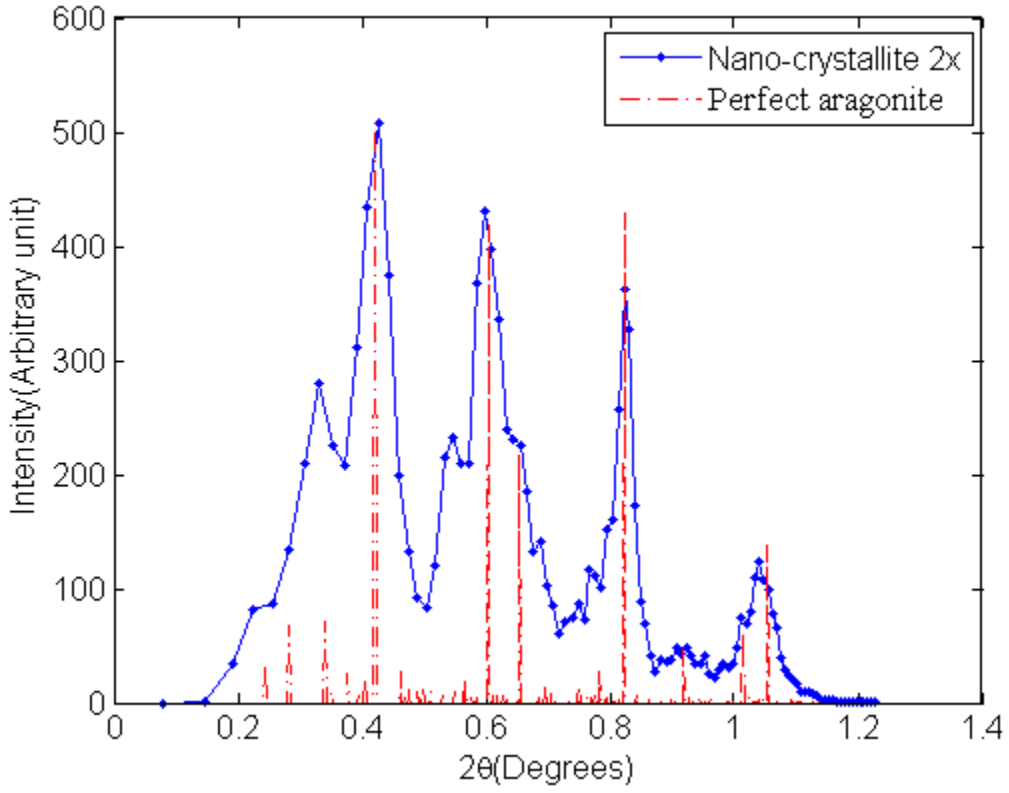

Figure 6.5: Powder diffraction line profile (blue) of a $\sim 20 \times 20 \times 40\ \mathring{A}^3$ aragonite nano-crystallite. Perfect crystal aragonite diffraction line profile (red) was superimposed for comparison.

6.2.3 3x of aragonite Supercell

A 29.76 $\times$23.67 $\times$ 51.66$\AA^3$ aragonite crystal containing 360 atoms was constructed to model such a nano-crystallite. The calculated powder diffraction profile for this particular crystal is presented in figure (6.6). Comparing with figure (6.4) we can see this no longer resembles an amorphous diffraction profile. The peak widths have become very small and all the peaks can be easily resolved. This is comparable to a macroscopic aragonite crystal.

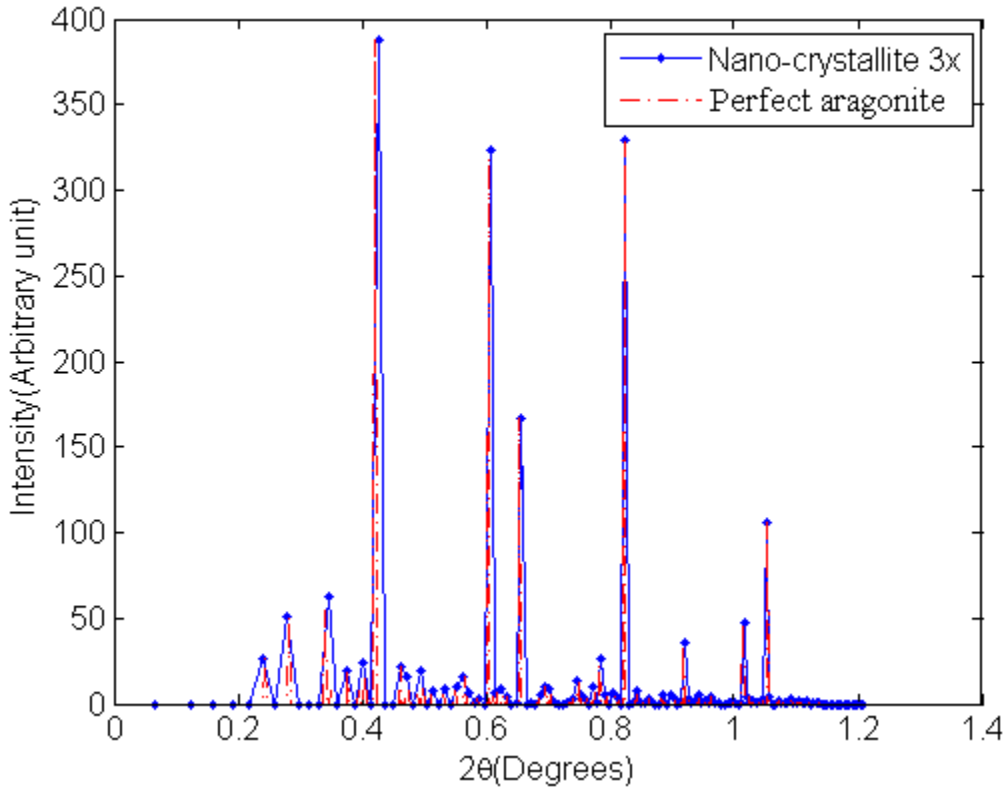

Figure 6.6: Powder diffraction line profile (blue) of a $\sim 30 \times 30 \times 60\,\AA^3$ aragonite nano-crystallite. Perfect crystal aragonite diffraction line profile (red) was superimposed for comparison.

Like calcite in the previous section one can also see here that, as the crystallite size is reduced the diffraction profile becomes more typical of an amorphous material.These results for calcite and aragonite along with other recent studies [33, 38, 59, 60] strongly suggest that the ACC phase may well just be a phase of $CaCO_3$ composed of nano-crystallites oriented in random directions, where the crystallite dimension is ~ 1.5 nm.

Given that we have an understanding of ACC nano-crystallite effect on its diffraction pattern; it would be interesting to see the effects of distortions such as carbonate tilts and Ca sublattice deviations on diffraction profiles from nano-crystallites. The reason we want to study this case is that ACC may contain some H_2O and Mg as impurities as discussed in chapter 1, and we showed in chapter 4 that the effect of these impurities in the crystal is basically introducing CO_3 tilts and Ca sub-lattice distortion in the crystal.

6.3 Diffraction Line Profile of Nano-crystallites with Distortions

In this section we shall study the diffraction pattern of calcite and aragonite 1x nano-crystallites (i.e. of volume $\sim 10 \times 10 \times 17$ $\mathring{A}^3$) when CO_3 tilts and Ca as well as C sub-lattice distortions are also present

6.3.1 Calcite

Carbonate tilts, Ca and C sub-lattice distortions were introduced in the cell used as the model for 1x calcite nano-crystallite in section 6.1.1. The simulated powder diffraction line profile (blue curve) is shown in figure 6.7. Comparing this diffraction pattern with that of perfect nano-crystallite (red dotted curve) we observe that there is not much difference between the two though the second peak around 0.7° is broader.

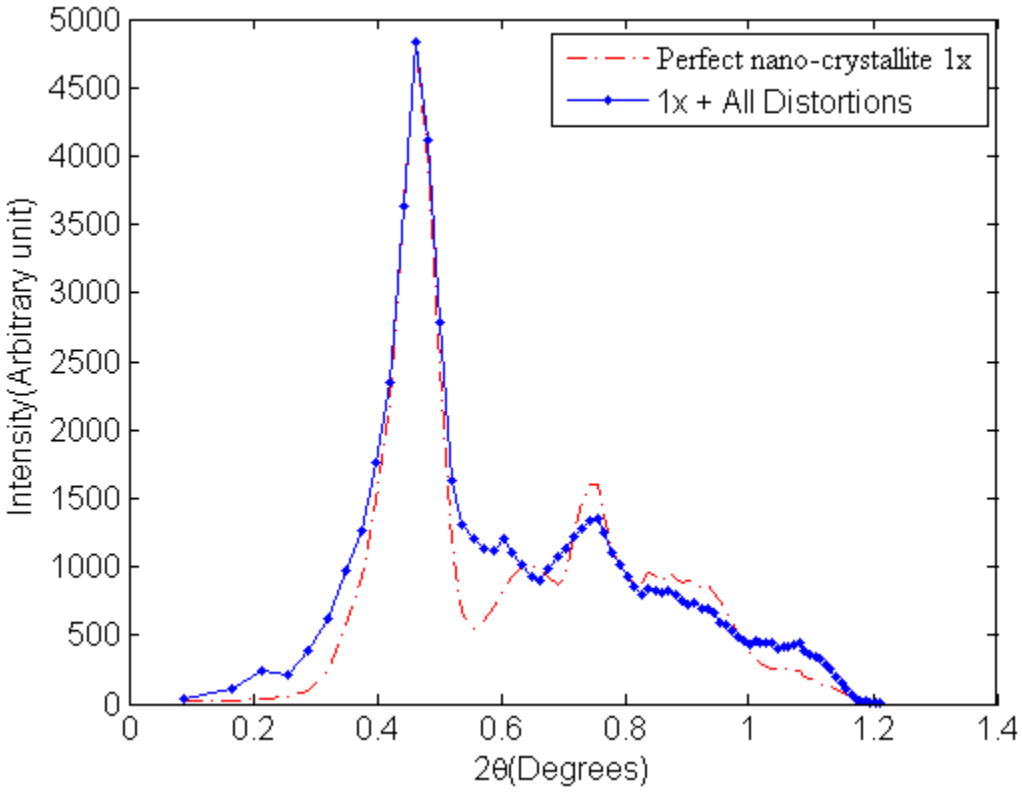

Figure 6.7: Powder diffraction line profile (blue) of a $\sim 10 \times 10 \times 17$ $\mathring{A}^3$ calcite nano-crystallite with CO_3 tilts + Ca sub-lattice distortion + C sub-lattice distortions. Pure calcite diffraction line profile (red) was plotted on same scale for comparison.

6.3.2 Aragonite

Carbonate tilts, Ca and C sub-lattice distortions were added in the cell described in section (6.2.1). A simulated diffraction profile of this distorted crystallite (blue) along with the perfect crystallite (red) is presented in figure 6.8. Comparing the two, we observe that there is a significant difference between two line profiles. In the distorted case, the peak at $2\theta = 0.53^\circ$ is very much reduced, the peak corresponding to $2\theta = 0.4^\circ$ is wider and in general the profile looks more like that from an amorphous material. So we can say that in this case the distortions do have the effect of making the diffraction profile appear more characteristic of that from an amorphous material.

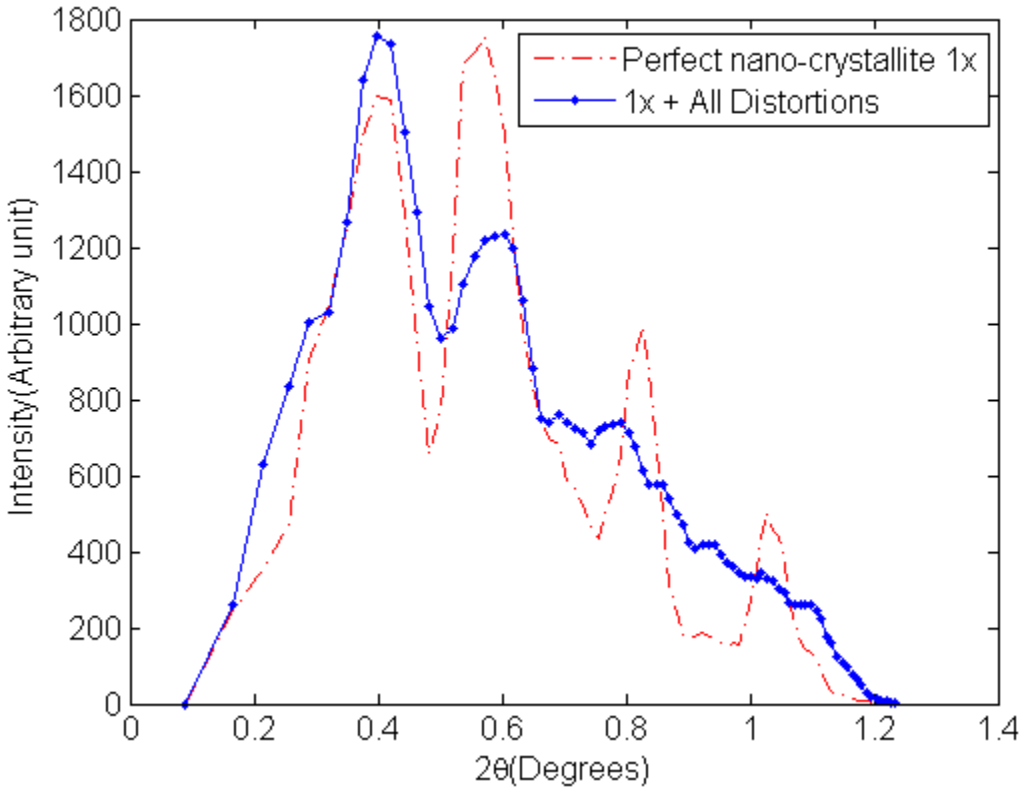

Figure 6.8: Powder diffraction line profile (blue) of a $\sim 10 \times 10 \times 20$ $\mathring{A}^3$ aragonite nano-crystallite with CO_3 tilts + Ca sub-lattice distortion + C sub-lattice distortions. Pure aragonite diffraction line profile (red) was superimposed for comparison.

6.3.3 Discussion

The above study clearly suggests that both calcite and aragonite nano-crystallites of dimension $\sim$ 1.5 nm are plausible explanations for ACC. Extra broadening of the peaks due to introduction of CO_3 tilts and Ca sub-lattice distortions even suggest that it is quite possible ACC might contain impurities like H_2O, Mg etc., as observed in nature. Below we present the electron diffraction results, obtained from transmission electron microscope at ASU, for an amorphous calcium carbonate sample and compare our calculations with it.

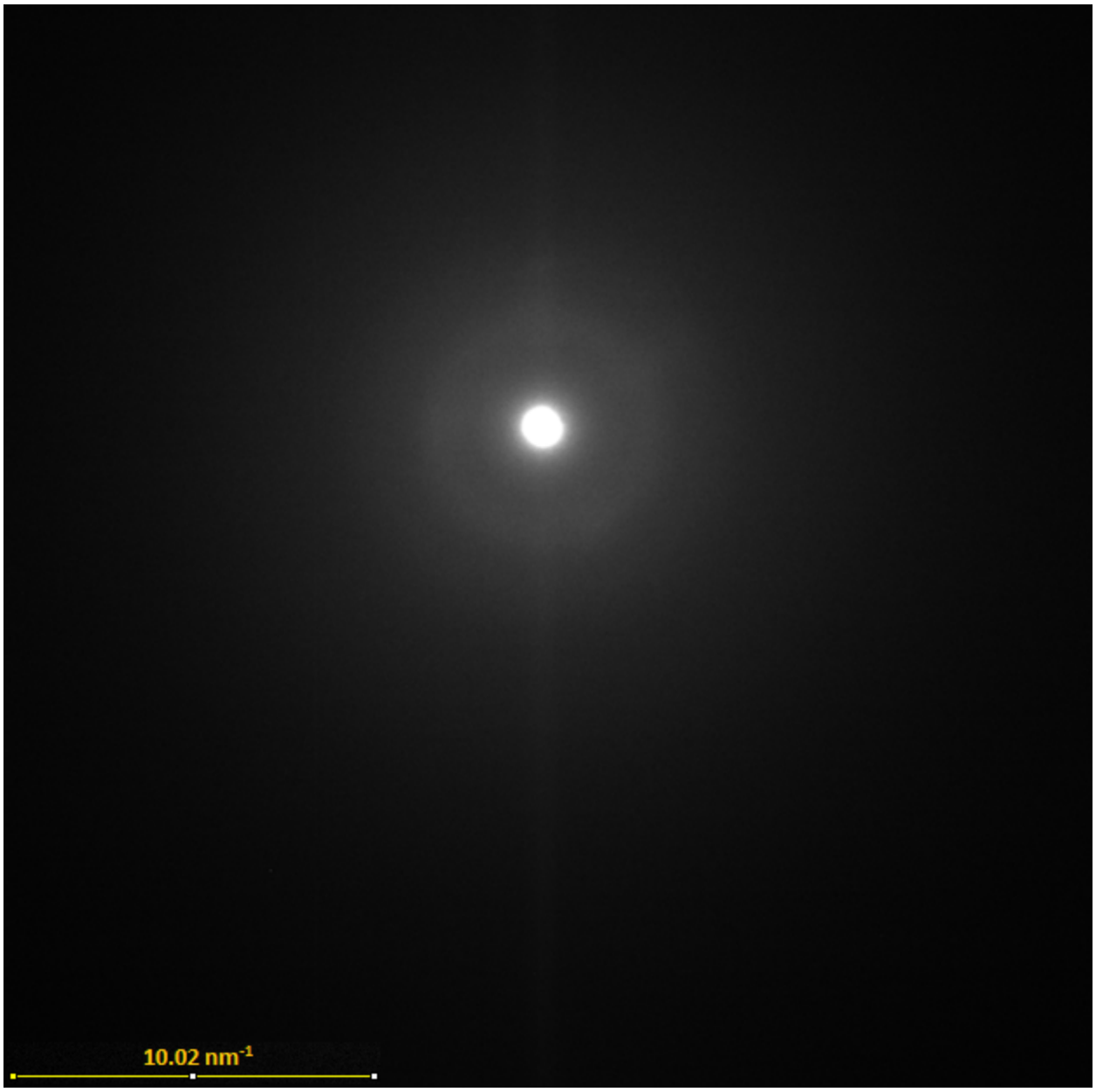

Figure 6.9: Transmission electron microscopy (200 keV electron beam) image (i) of amorphous calcium carbonate

Electron diffraction patterns were recorded from a sample of ACC provided by Yael Politi using the JEOL 2010 in the LECSSS operated at 200keV. The diffraction data

was recorded with both 12 cm and 15cm camera lengths with a 2 minute acquisition time. The 2nd condenser aperture was used as it was not possible to image specimen with the smaller 1st condenser aperture due to the very low intensity. Figure (6.9) and (6.11) are two electron diffraction (ED) patterns.

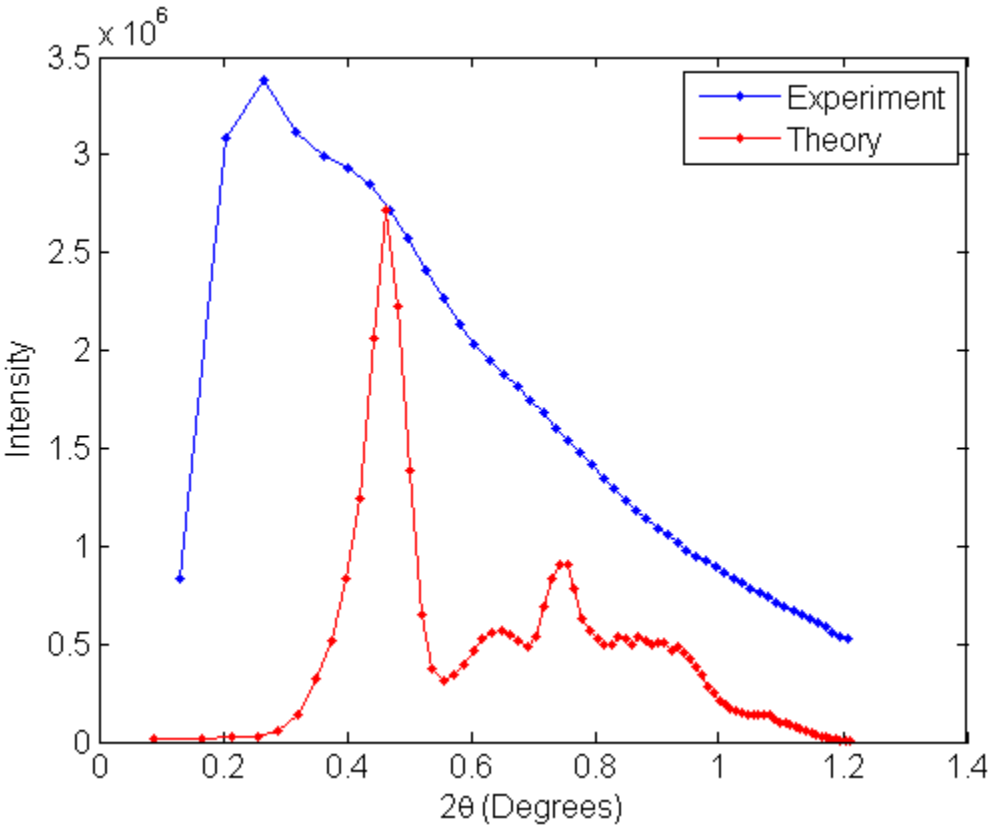

Figure 6.10: Annulus integrated diffracted line profile (blue) of image (i). Diffraction line profile of a $\sim 10 \times 10 \times 17$ $\AA^3$ calcite nano-crystallite (red) is shown on the same scale for comparison purpose.

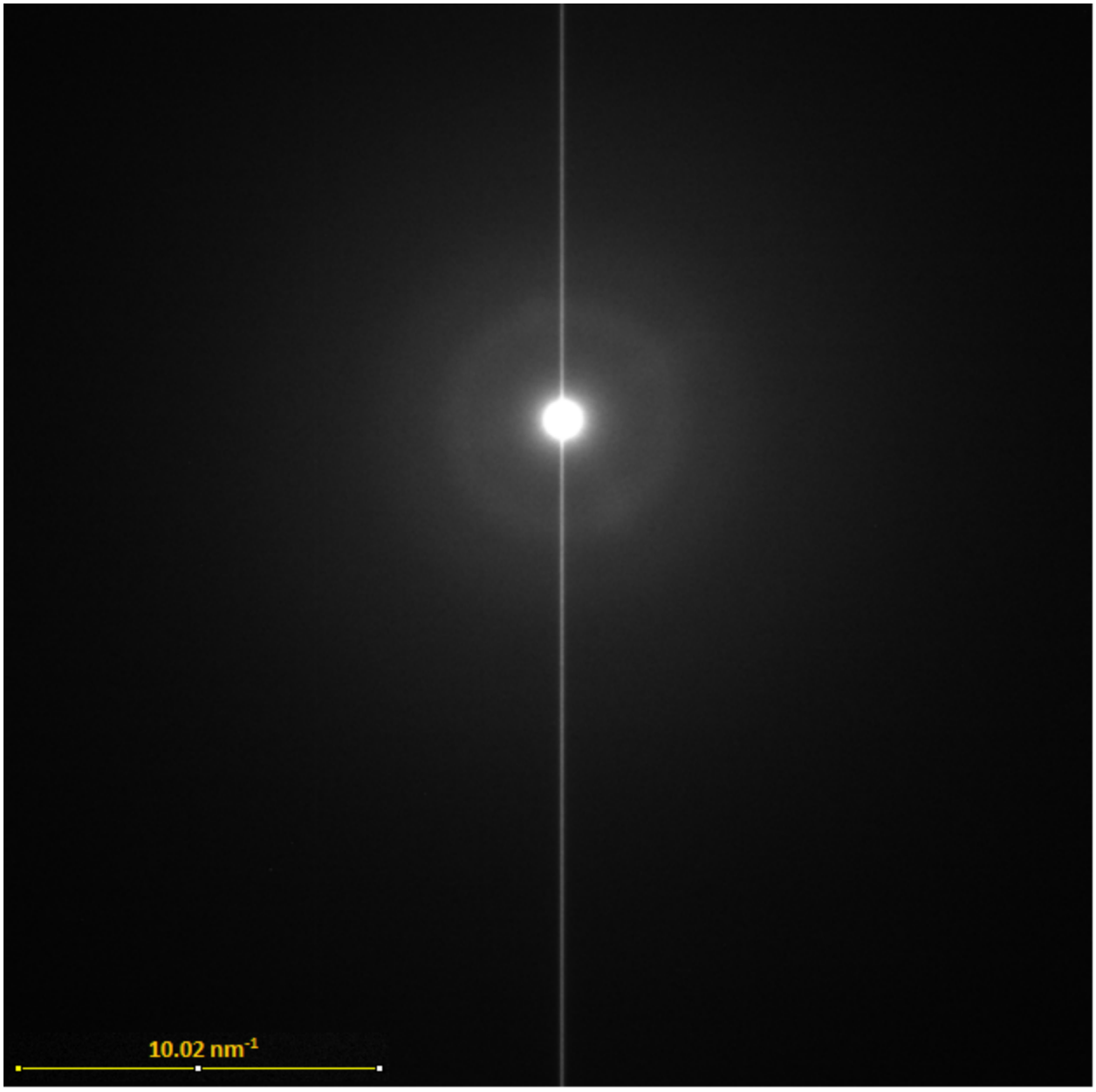

Figure 6.11: Another TEM (200 keV electron beam) image (ii) of amorphous calcium carbonate

Figure (6.10) and (6.12) are their corresponding annular integrated line profile. To compare our simulated results for model nano-crystallites with the ED line profiles, we show the perfect calcite 1x nano-crystallite diffraction profile on the same scale.

First we need to clarify that the measured ED line profile also has background noise from instrumental effects and inelastic scattering. So we shall only compare peak positions and peak widths. We shall assume that the background intensity varies smoothly compared to that of the diffraction peaks. Hence in figure (6.12) we fit a second order polynomial to the baseline (red circles) of the ED line profile. Figure (6.13) shows the baseline subtracted line profile of ED image (ii) along with the line profile from the calcite 1x nano-crystallite (red curve, plotted on same scale). Since the intensity cannot be negative, we took the subtracted value to be zero when the value given by the fit was greater than the measured intensity.

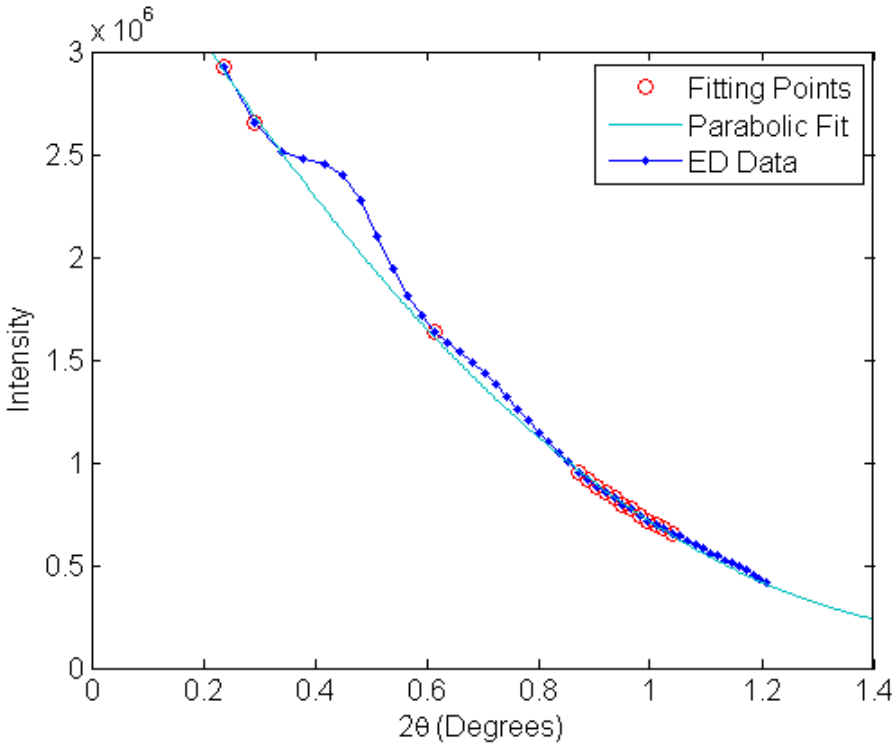

Figure 6.12: Annulus integrated diffracted line profile (blue) of image (ii). The baseline (red dots) points were fitted a second order polynomial (greenish-blue curve).

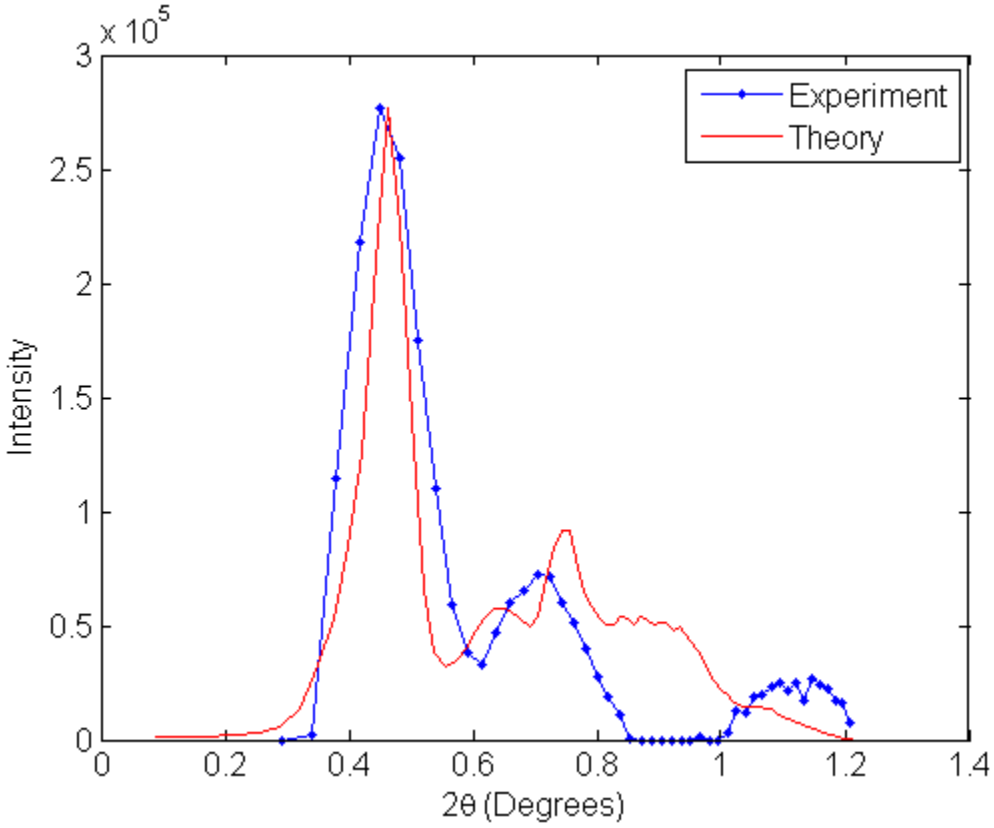

Figure 6.13: Baseline subtracted annulus integrated diffraction profile (blue) of image (ii). Diffraction line profile of a $\sim 10 \times 10 \times 17\ \mathring{A}^3$ calcite nano-crystallite (red) is shown on the same scale for comparison purpose.

6.5 Comparison between Theory and Experiment

We shall use figure (6.13) for a qualitative comparison between the experimental and the calculated line profiles. Apart from uncertainties introduced by the annular averaging and background removal in the experimental diffraction profile there are other reasons which make quantitative comparison problematic. Though the electron diffraction pattern obtained appeared amorphous, it should be mentioned that the sample used in experiment was $\sim$3 years old and might have partially transformed to calcite. We have also not taken into account the electron beam divergence angle in our data analysis In our calculations, we only used four directions to simulate the powder diffraction pattern,

hence we cannot possibly obtain all the peaks. Keeping all these constraints/limitations in mind let us compare the two profiles in figure (6.13).

We shall observe the peak positions, their widths and relative intensities. Our model predicts that there should be two peaks, the main one at $2\theta = 0.47^\circ$ and the other much broader secondary peak in the vicinity of 0.7° (from 0.65° to 0.85°). The experimental line profile shows the main peak at $2\theta = 0.45^\circ$, almost exactly where our calculation predicts. However the second peak does not match well, though the experimental profile does show a small broad peak $\sim 2\theta = 0.72^\circ$, close to theoretically predicted value. The experimental line profile also shows a small third peak which our theory does not predict. The main peak ($2\theta = 0.47^\circ$) width for our calculated profile is 0.08°, smaller than the experimental one $\sim 0.14^\circ$. But because the ED profile should be deconvoluted by beam divergence for proper analysis, one would expect the experimental peak width to shrink, hence the agreement might be far better agreement than it appears from this figure. Also the relative intensities of the main peak and the secondary peak qualitatively agree with the experiment.

Keeping the limitations in mind we can conclude that there is reasonable qualitative agreement between the calculated and experimental line profiles. Though certainly not conclusive, this result should bolster the claim that the ACC might be composed of nano-crystallites.

Chapter 7

CONCLUSION

In this dissertation we investigated the atomistic structure models of amorphous calcium carbonate (ACC) that are consistent with diffraction measurements. For that purpose a calcite supercell with 24 formula units was constructed by doubling the hexagonal cell along the '**a**' and '**b**' unit cell vectors. Various clustered and scattered configurations with 6 Mg atoms substituting for Ca, corresponding to 6 wt. %, were relaxed using the VASP plane wave pseudopotential code. The relaxation was repeated with clusters of 3 to 5 water molecules (2.25-3.75 wt %) and also with scattered distributions of 4 water molecules, inserted in the interstitial positions in the supercell. In both the hydrated and substitutional magnesium cases it was noticed that the clustered impurity configurations yieldes lower free energies than the scattered arrangements. Distributions of inter-cation distance and carbonate group tilts were calculated from the relaxed atomic positons. The procedure described above was also applied to aragonite, a polymorph of calcite. After relaxing the structures it was observed that when Mg substituted for Ca, the carbonate groups were undistorted and there was a very narrow distribution of inter-cation nearest neighbor distances). The most noticeable effect was the tilting of the carbonate groups over an 8° range. The insertion of water had even more dramatic effects on the carbonate groups which were generally tilted up to 30°, and the Ca sublattice was distorted heavily (half width $\sim 20\%$ of actual bond-length) in the vicinity of clusters.

Using these distortions a multi-scale model for ACC was developed that was used for calculating diffraction patterns. It was found that the induced distortions were not enough to generate a diffraction pattern typical of an amorphous material, though there were visible deviations from the diffraction profile of a prefect crystal. Next we turned our focus to nano-crystallites as some recent studies [33, 38, 59, 60] suggested

that ACC might be composed of nano-crystallites. We were finally able to generate a diffraction pattern that appeared similar to that from ACC for a crystallite of size ~ 2 nm^3.

To compare our theoretical results for nano-crystallites with experiment, we performed electron diffraction (ED) experiment on one amorphous calcium carbonate sample. In our preliminary analysis we observed a qualitative agreement between the two diffraction profiles, which should bolster the claim that ACC might be composed of nano-crystallites, though more measurements are necessary to come to have full confidence in this conclusion.

For a quantitative accurate calculation of powder diffraction profile we are currently working on including more directions of the incoming beams in our diffraction code. For a more refined width estimation of the diffracted peaks nano-crystallites with facets that are the appropriate lowest energy surfaces, rather than a heuristic hexagonal cell, should be chosen. More experimental results, may be even some X-ray diffraction patterns, should be compared with our calculations. A much more rigorous data analysis on the experimental diffraction pattern should be performed to separate the diffraction peaks completely from the background. Additionally it would be interesting to investigate the interaction of proteins and macromolecules with the calcite and aragonite surfaces, as in nature biominerals are often found in an environment where biomolecules are believed to play an important role in determining mineral structure and growth and growth mechanisms.

To summarize, the main effect of either substituting 6 wt.% Mg for Ca or inserting less than 4 wt% water in either a calcite or aragonite supercell consisting of 24 formula units, was tilting of the carbonate groups. There were some significant local distortions of the Ca sub-lattice near the impurity clusters. A multi-scale model of ACC based on these distortion distributions did not generate structures that gave amorphous

diffraction pattern, suggesting that local random fluctuations in the atoms position about their equilibrium did not sufficiently disturb the long-range order in the crystal. We were able to generate amorphous diffraction pattern by modeling the ACC as an ensemble of calcite or aragonite nano-crystallites of size ~ 2 nm^3, oriented in different directions. Some basic data-analysis on the ED pattern from an ACC sample shows a qualitative agreement with our calculated diffraction profiles for nano-crystallites.

REFERENCES

[1] S. Mann, *Biomineralization: Principles and Concepts in Biogenic Materials and Chemistry* (Oxford Univ. Press, Oxford, 2001).

[2] P.M. Dove, J.J. De Yoreo, S. Weiner, Eds., *Biomineralization* 54, 57-93 (Mineral Soc. of Am., Washington DC, 2004).

[3] H.A. Lowenstam, S. Weiner, *On Biomineralization* (Oxford Univ. Press, Orford, 1989).

[4] P.E. Hare, P.H. Abelson, *Carnegie Inst. Washington Yearb.* 64, 223-234 (1965).

[5] F. Wilt, *J. Struct. Biol.* 126, 216-226 (1999).

[6] J.P. Grotzinger, W.A. Waters, A.H. Knoll, *Paleobiology* 26, 334 (2000).

[7] J.D. Currey, Mechanical properties of mother of pearl in tension. *Proc.R. Soc. London, Ser. B* 196, 443 (1977).

[8] F.H. Wilt, Matrix and Mineral in the Sea Urchin Larval Skeleton. *J. Struct.Biol.* 126, 216-226, (1999).

[9] F.C. Meldrum, Calcium carbonate in biomineralisation and biomimetic chemistry. *Int. Mater. Rev.* 48, 187-224 (2003).

[10] H. Effenberger, *Monatsh. Chem.* 112, 899-909 (1981).

[11] E.E. Coleyshaw, G. Crump, W.P. Griffith, *Spectrochim. Acta, part A* 59, 2231-2239 (2003).

[12] M. Neumann, M. Epple, *Eur. J. Inorg. Chem.* 1953-1957 (2007).

[13] K.F. Hesse, H. Kueppers, E.Z. Suess, *Kristallgr.* 163, 227 (1983).

[14] L. Addadi, S. Raz, S. Weiner, *Adv. Mater.* 15, 959-170 (2003).

[15] J.R. Young, J.M. Didimus, P.P. Bowen, B. Prins, S. Mann, *Nature* 356, 516 (1992).

[16] L. Addadi, D. Joester, F. Nudelman, S. Weiner, *Chem. Eur. J.* 12, 980 (2006)

[17] F.C. Meldrum, *Int. Mater. ReV.* 48, 187 (2003).

[18] B. Hasse, H. Ehrenberg, J.C. Marxen, W. Becker, M. Epple, *Chems. Eur. J.* 6, 3679 (2000).

[19] C.E. Killian, *et. al. J. Am. Chem. Soc.* 131, 18404-18409 (2009).

[20] S.B. Mukkamala, C.E. Anson, A.K. Powell, *J. Inorg. Biochem.* 100, 1128 (2006).

[21] A.N. Kulak, P. Iddon, S.P. Armes, H. Coelfen, O. Paris, R.M. Wilson, F.C. Meldrum, *J. Am. Chem. Soc.* 129, 3729 (2007).

[22] L. Brecevic, A. Nielsen, *J. Cryst. Grow.* 98, 504-510 (1989).

[23] H. Setoguchi, M. Okazaki, S. Suga, *Origin, Evolution, and Modern Aspects of Biomineralization in Plants and Animals.* (Plenum Press, NewYork, 409-418 1989).

[24] H.A. Lowenstam, *Bull. Mar. Sci.* 45, 243-252 (1989).

[25] M.G. Taylor, K. Simkiss, G.N. Greaves, M. Okazaki, S. Mann, *Proc. R. Soc. Lond. B* 252, 75-80 (1993).

[26] E. Beniash, J. Aizenberg, L. Addadi, S. Weiner, *Proc. Roy. Soc. Lond B* 264, 461-465 (1997).

[27] I.M. Weiss, N. Tuross, L. Addadi, S. Weiner, *Proc. R. Soc. Lond. B* 264, 461 (1997).

[28] L. Gago-Duport, M.J.I. Briones, J.B. Rodriguez, B. Covelo, *J. Struct. Biol.* 162, 422-435 (2008).

[29] C.E. Killian *et al.*, *J. Am. Chem. Soc.* 131, 18404-18409 (2009).

[30] N. Koga, Y. Nakagoe, H. Tanaka, *Thermochim. Acta.* 318, 239-244 (1998).

[31] D. Wang, A.F. Wallace, J.J. De Yoreo, P.M. Dove *Proc. Natl. Acad. Sci.* 106, 21511-21516 (2009).

[32] N. Koga, Y. Yamane, *J. Therm. Anal. Calorim.* 94,379-387 (2008).

[33] E.M. Pouget, P.H.H. Bomans, J.A.C.M. Goos, P.M. Frederik, G. se Wirth, N.A.J.M. Sommerdijk, *SCIENCE* 323, 1455-1458 (2009).

[34] R.S.K. Lam, J.M. Charnock, A. Lenniec, F.C. Meldrum, *Cryst. Eng. Commun.* 9, 1226-1236 (2007).

[35] Radha *et al.*, *P.N.A.S* 107, 38, 16439 (2010).

[36] S. Raz, S. Weiner, L. Addadi, *Adv. Mater.* 12, 1 (2000).

[37] S. Raz, P.C. Hamilton, F.H. Wilt, S. Weiner, L. Addadi, *Adv. Funct. Mater.* 13, 480-486 (2003).

[38] F.M. Michel, J. MacDonald, J. Feng, B.L. Phillips, L. Ehm, C. Tarabrella, J.B. Parise, R. Reeder, *J. Chem. Mater.* 20 (2008).

[39] M. Faatz, F. Grohn, G. Wegner, *Adv. Mater.* 16, 996 (2004).

[40] K. Gorna, R. Munoz-Espi, F. Gohrn, G. Wegner, *Macromol. Biosci.* 7, 163 (2007).

[41] J. R. Lee *et. al.*, *J. Am. Chem. Soc.* 129, 10370 (2010).

[42] F. M. Michel, *et. al.*, *Chem. Mater.* 20, 4720-4728 (2008).

[43] Y. Levi-Kalisman, S. Raz, S. Weiner, L. Addadi, I. Sagi, *J. Chem. Soc.* 21, 3977-3982 (2000).

[44] H. Nebel, M. Neuman, C. Mayer, M. Epple, *Inorg. Chem.* 47, 7874-7879 (2008).

[45] J.S. Robach, S.R. Stock, A. Veis, *J. Struct. Biol.* 155, 87-95 (2006).

[46] L.M. Walter, J.S. Hanor, *J. Sediment Petrol* 49, 937-944 (1979).

[47] E. Loste, R.M. Wilson, R. Seshadri, F.C. Meldrum, *J. Cryst. Growth* 254, 206-218 (2003).

[48] X. Cheng, P.L. Varona, M.J. Olszta, L.B. Gower, *J. Cryst. Growth* 307, 395-404 (2007).

[49] E. Segev, J. Erez, *Geochem. Geophys. Geosyst.* 7, Q02P09 (2006).

[50] D. Wanga, A.F. Wallacea, J.J. De Yoreob, P.M. Dove, *P.N.A.S.* 106, 51, 21511-21516 (2009).

[51] L. Addadi, *et. al. Chem. Mater.* 22, 161, 161-166 (2010).

[52] P.U.P.A. Gilbert *et. al.*, *Langmuir* 24, 2680-2687 (2008).

[53] R.A. Metzler, G.A. Tribello, M. Parrinello, P.U.P.A. Gilbert, *J. Am. Chem. Soc.* 132, 11585-11591 (2010).

[54] S. Weiner, Y. Levi-Kalisman, S. Raz, L. Addadi, *Connect. Tissue Res.* 44, 214-218 (2003).

[55] B. A. Gotliv, L. Addadi, S. Weiner, *Chem. BioChem.* 4, 522-529 (2003).

[56] J. Aizenberg, G. Lambert, L. Addadi, S. Weiner, *Adv. Mater.* 8, 222-226 (1996).

[57] Y. Politi *et al.*, *Adv. Funct. Mater.* 16, 1289-1298 (2006).

[58] N. Koga *et al.*, *Thermochimica Acta.* 318, 239-244 (1998).

[59] D. Gebauer, A. Voelkel, H. Coelfen, *SCIENCE* 322, 1819-1822 (2008).

[60] P. Martin, D. Spagnoli, A. Marmier, S.C. Parker, D.C. Sayle, G. Watson, *Mol. Simul.* 32, 1079 (2006).

[61] M.G. Taylor, K. Simkiss, Structural and analytical studies on metal-ion containing granules. In *Biomineralization, chemical and biochemical perspectives*. (Ed. S. Mann, J. Webb, R.J.P. Williams), 427-460. (Weinheim, VCH, 1989).

[62] F. Wooten, K. Weiner, D. Weaire, *Phys. Rev. Lett.* 54, 13 (1985).

[63] A.M.R. de-Graff, M.F. Thorpe, *Acta. Cryst. A* 66, 22-31 (2010).

[64] W.H. Zachariasen, *J. Am. chem. Soc.* 54, 3841-3851 (1932).

[65] M. Lei, A.M.R. de Graff, M.F. Thorpe, S.A. Wells, A. Sartbaeva, *Phys. Rev. B* 80, 024118 (2009).

[66] P. Rez, A. Blackwell, *J. Phys. Chem. B* 115, 38, 11193-8 (2011).

[67] R.M. Martin, *Electronic structure: Basic Theory and Practical Methods* (Cambridge Univ. Press, Cambridge, 2004).

[68] M. Born, J.R. Oppenheimer, *Ann.Physik* 84, 457 (1927).

[69] M. Born, K. Huang, *Dynamical Theory of Crystal Lattices* (Oxford Univ. Press, Oxford, 1954).

[70] R. Pick, M.H. Cohen, R.M. Martin, *Phys. Rev. B* 1, 910-920 (1970).

[71] D. R. Hartree, *Proc. Cambridge Phil. Soc.* 24, 89, 111, 426 (1928).

[72] V.Fock, *Z. Phys.* 61, 126 (1930).

[73] H.D. Cohen, C. C. J. Roothaan, *J. Chem. Phys.* 43, S34 (1965).

[74] Richard A. Ferrell, *Phys. Rev.* 107, 1631-1634 (1957).

[75] A. Szabo, N.S. Ostlund, *Modern Quantum Chemistry.* (Mineola, New York, Dover Publishing, 1996).

[76] H. M. Gladney, A. Veillard, *Phys. Rev.* 180, 385-395 (1969).

[77] T. Ziegler, A. Rauk, *Inorg. Chem.* 18, 6, 1558-1565 (1979).

[78] B.D. Esry, C.H. Greene, J.P. Burke Jr., J.L. Bohn, *Phys. Rev. Lett.* 78, 3594-3597 (1997).

[79] J.A. Maruhn, P.G. Reinhard, P.D. Stevenson, M.R. Strayer, *Phys. Rev. C* 74, 027601 (2006).

[80] Y.H. Shao, C.A. White, M. Head-Gordon, *J. Chem. Phys.* 114, 6572-6577 (2001).

[81] P. Fulde, *Electron Correlations in Molecules and Solids* (Springer, 1995).

[82] R.M. Dreizler, E.K.U. Gross, *Density Functional Theory* (Springer, 1990).

[83] R.G. Parr, Y. Weitao, *Density-functional Theory of Atoms and Molecule* (Oxford Univ. Press, Oxford, 1994).

[84] W. Kohn, L.J. Sham, *Phys. Rev. A* 1133, A1133 (1965).

[85] P. Hohenberg, W. Kohn, *Phys. Rev. B* 76, 6062 (1964).

[86] M. Levy, *Proc. Nat. Acad. Sci.* 76, 6062 (1979).

[87] J. Kohanoff, *Electroninc Structure Calculations for Solid and Molecules* (Cambridge univ. Press, Cambridge, 2006).

[88] D. M. Ceperley, B. J. Alder, *Phys. Rev. Lett.* 45, 7, 566 (1980).

[89] R.Q. Hood, M.Y. Chou, A.J. Williamson, G. Rajagopal, R.J. Needs, *Phys. Rev. Lett.* 78, 17, 3350 (1997).

[90] R.Q. Hood, M.Y. Chou, A.J. Williamson, G. Rajagopal, R.J. Needs, *Phys. Rev. B* 57, 15, 8972 (1998).

[91] P. Fulde, *Electron Correlations in Molecules and Solids* (Springer, 1995).

[92] C. Kittel, *Introduction to Solid State Physics* (8th Ed., Wiley, 2004).

[93] N.W. Ashcroft, N.D. Marmin, *Solid State Physics* (1st Ed., Brooks Cole, 1976).

[94] J. Arfken, H. Waber, *Mathematical Methods for Physicists* (6th Ed., Academic Press, 2005).

[95] P.P. Ewald, *Physik. Z.* 14, 465-472 (1913).

[96] A. Doyle, P.S.Turner, *Acta. Cryst. A* 24, 390 (1968).

[97] D. Rez, P. Rez, I. Grant, *Acta. Cryst. A* 50, 481 (1994).

[98] F.W. Byron Jr., C.J. Joachin, *Phys. Rev. A* 1, 157, (1967).

[99] N. F. Mott, H.S.W. Massey, *The Theory of Atomic Collisions* (3rd Ed., Oxford Univ. Press, Oxford, 1965).

[100] *International Tables for X-ray Crystallography* Vol. III.

[101] V. Vand, T.F. Eiland, R. Pepinsky, *Acta. Cryst.* 10, 303 (1957).

[102] J.B. Forsyth, M. Wells, *Acta. Cryst.* 12, 412 (1959).

[103] D.T. Cromer, J.T. Waber, *Acta. Cryst.* 12, 104 (1965).

[104] G.H. Smith, R.E. Burge, *Acta. Cryst.* 15, 182 (1962).

[105] M. Born, E. Wolf, *Principle of Optics* (7th Ed., Cambridge Univ. Press, Cambridge, 1999).

[106] F. Jenkins, H. White, *Fundamentals of Optics* (4th Ed., McGraw-Hill, 2001).

[107] A. Ghatak, S. Lokanathan, *Quantum Mechanics Theory and Application* (1st Ed., Kluwer Ac. Pub., 2004).

[108] A. Authier, *Dynamical Theory of X-Ray Diffraction* (Rev. Ed., Oxford Univ. Press, Oxford, 2004)

[109] J.M. Cowley, P.M. Fields, *Acta. Cryst. A* 35, 28-37. (1979).

[110] http://www.crystalmaker.com/crystaldiffract/

[111] E.B. Tadmor, R.E. Miller, *Modeling Materials: Continuum, Atomistic and Multiscale Techniques* (Cambridge Univ. Press, Cambridge, 2011).

[112] W. H. Press *et al.*, *Numerical recipes in C++* (2nd Ed. Cambridge Univ. Press, Cambridge, 2002).

[113] http://www.gnu.org/s/gsl/manual/html_node/The_Gaussian_Distribution.html

[114] http://webmineral.com/data/Aragonite.shtml

[115] http://webmineral.com/data/Calcite.shtml

APPENDIX A

THE DIFFRACTION CODE

The diffraction code, written in C is included below. The Working principle of this code can be found in chapter 3 in the form of a flowchart.

```
/*

 *-------------------------AmorphousXtalDiffraction.c-------------------------*
      *.....................CREDIT: SOURABH SINHA.....................*

1. Make a crystal of variable size (upto 10x10x10 of original super-cell in POSC
AR ~ 2 nm^3), with/without the distortions i.e. carbonate tilts, Ca/C sub-lattic
e distortions to generate the model of ACC.

2. Notice, a perfect nano-crystallite is nothing but the original supercell with
 no distortions.

3. Generate the diffraction pattern for the above model crystal.

~~~~~~~~~~~~~~~~~~~~~~~~~~~~~~~~~~~~~~~~~~~~~~~~~~~~~~~~~~~~~~~~~~~~~~~~~~~~~~*/

#include<stdio.h>
#include<stdlib.h> //for RAND_MAX
#include<math.h>
#include<time.h> //for seeding random number
#include<string.h>
#include<gsl/gsl_rng.h>//GNU-scientific library for random number
#include<gsl/gsl_randist.h>//generator for gaussian deviates

#define PI (2*acos(0))

int Status(int N,char EOCell,int n,float HeightC,float zMinC,float CoordCz);
float THeta(float ThetaMax, float Slope, float yIntercept);
float PHi(float PhiMax);
void gnuplot(const char *gnucommand);

int main(int argc, char *argv[])
{
  srand((unsigned int)time(NULL));
  FILE *ifp=NULL;
  ifp = fopen("POSCAR_calcite","r");

  long int i=0;
  int i0=0, i1=0, i2=0, i3=0, i4=0;
  int species=4;//have to be careful for different samples
  int lines=0, TotalAtoms=0;
  char c;
  float x[200], y[200], z[200], RealBasis[3][3];
  float CoordinateC[50][3], CoordinateCa[50][3];
  float CoordinateH[20][3], CoordinateO[100][3];
  float ScaleFactor=0.0;

// Extract the atoms and their numbers from POSCAR
  int SpeciesNumber[10];

// Find the number of lines in POSCAR
  if(ifp == NULL)
  {
    lines = 0;
  }
  else
  {
    while((c = fgetc(ifp)) != EOF)
    {
      if(c == '\n')
      {
        lines = lines + 1;
//Writing the real space basis vectors
```

```
        if(lines == 1)
        {
          fscanf(ifp,"%f",&ScaleFactor);
        }
        if(lines>=2 && lines<5)
        {
          fscanf(ifp,"%f %f %f",&x[lines],&y[lines],&z[lines]);
          RealBasis[i0][0] = ScaleFactor*x[lines];
          RealBasis[i0][1] = ScaleFactor*y[lines];
          RealBasis[i0][2] = ScaleFactor*z[lines];
          i0++;
        }
//find the total number of atoms and number of each species
        if(lines == 5)
        {
          for(i=0; i<species; i++)
          {
            fscanf(ifp,"%d",&SpeciesNumber[i]);

            TotalAtoms += SpeciesNumber[i];
          }
        }
//Writing the Co-ordiantes of each atoms
        if(lines >= 7  && lines < (SpeciesNumber[0]+7)) //C
        {
          fscanf(ifp,"%f %f %f",&x[lines],&y[lines],&z[lines]);
          CoordinateC[i1][0] = x[lines];
          CoordinateC[i1][1] = y[lines];
          CoordinateC[i1][2] = z[lines];
          i1++;
        }
        if(lines >= (SpeciesNumber[0]+7)  && lines < (SpeciesNumber[0]+SpeciesNu
mber[1]+7)) //Ca
        {
          fscanf(ifp,"%f %f %f",&x[lines],&y[lines],&z[lines]);
          CoordinateCa[i2][0] = x[lines];
          CoordinateCa[i2][1] = y[lines];
          CoordinateCa[i2][2] = z[lines];
          i2++;
        }
//We are not keeping the water molecules in the supercell for now.
        if(lines >= (SpeciesNumber[0]+SpeciesNumber[1]+7)  && lines < (SpeciesNu
mber[0]+SpeciesNumber[1]+SpeciesNumber[2]+7)) //H
        {
          fscanf(ifp,"%f %f %f",&x[lines],&y[lines],&z[lines]);
          CoordinateH[i3][0] = x[lines];
          CoordinateH[i3][1] = y[lines];
          CoordinateH[i3][2] = z[lines];
          i3++;
        }
        if(lines >= (SpeciesNumber[0]+SpeciesNumber[1]+ SpeciesNumber[2]+7)  &&
lines < (TotalAtoms+7)) //O
        {
          fscanf(ifp,"%f %f %f",&x[lines],&y[lines],&z[lines]);
          CoordinateO[i4][0] = x[lines];
          CoordinateO[i4][1] = y[lines];
          CoordinateO[i4][2] = z[lines];
          i4++;
        }
        if(lines == (TotalAtoms+7))
        {
          break;
        }
```

```
      }
    }
  }

  fclose(ifp);

/*==========================================================================*/

//Convert the fractional coordinates to Cartesian coordiantes (we are using only
 Ca and C lattice. We will create the CO3 group later.)

  float CoordC[SpeciesNumber[0]][3];

  for(i=0;i<SpeciesNumber[0];i++)
  {
    CoordC[i][0]=CoordinateC[i][0]*RealBasis[0][0]+CoordinateC[i][1]*RealBasis[1
][0]+CoordinateC[i][2]*RealBasis[2][0];
    CoordC[i][1]=CoordinateC[i][0]*RealBasis[0][1]+CoordinateC[i][1]*RealBasis[1
][1]+CoordinateC[i][2]*RealBasis[2][1];
    CoordC[i][2]=CoordinateC[i][0]*RealBasis[0][2]+CoordinateC[i][1]*RealBasis[1
][2]+CoordinateC[i][2]*RealBasis[2][2];
  }

  float CoordCa[SpeciesNumber[1]][3];

  for(i=0;i<SpeciesNumber[1];i++)
  {
    CoordCa[i][0]=CoordinateCa[i][0]*RealBasis[0][0]+CoordinateCa[i][1]*RealBasi
s[1][0]+CoordinateCa[i][2]*RealBasis[2][0];
    CoordCa[i][1]=CoordinateCa[i][0]*RealBasis[0][1]+CoordinateCa[i][1]*RealBasi
s[1][1]+CoordinateCa[i][2]*RealBasis[2][1];
    CoordCa[i][2]=CoordinateCa[i][0]*RealBasis[0][2]+CoordinateCa[i][1]*RealBasi
s[1][2]+CoordinateCa[i][2]*RealBasis[2][2];
  }

/*==========================================================================*/

// Repetition of unit cell in all 3 directions
  int N=0; //Can go upto 5
  char EOCell = 'O';//even or odd cell? Values only can be 'O' or 'E'. 'O' for
odd which has (2*N+1) cells (includes 0), and 'E' for even which has 2*N cells (
excludes 0)
  long int TotalCNum, TotalCaNum;
  if(EOCell == 'E')
  {
    TotalCNum = SpeciesNumber[0]*(2*N)*(2*N)*(2*N);
    TotalCaNum = SpeciesNumber[1]*(2*N)*(2*N)*(2*N);
  }
  else if (EOCell == 'O')
  {
    TotalCNum = SpeciesNumber[0]*(2*N+1)*(2*N+1)*(2*N+1);
    TotalCaNum = SpeciesNumber[1]*(2*N+1)*(2*N+1)*(2*N+1);
  }

  float NewCoordC[TotalCNum][3];
  float NewCoordCa[TotalCaNum][3];
  long int j, k, l=0, m=0;
//Diclaration for Ca distortion, we will insert the distortion in one direction
only for simplicity.
  float Sigma = 2.0;
  float Mu = 0.0;
  float MinDist = -0.39; //In Ang, see the distribution
  float MaxDist = 0.39; //You should read these from am Input file
```

```
  float GaussDv = 0.0;
  const gsl_rng_type * T0;
  gsl_rng * Random;

  gsl_rng_env_setup();
  T0 = gsl_rng_default;
  Random = gsl_rng_alloc (T0);

  if(EOCell == 'E') //cell is symmetric about the origin
  {
//for C
    i = -N;//+1 is to gerenate the edge atoms for PDFs
    do
    {
      j = -N;
      do
      {
        k = -N;
        do
        {
          for(l=0; l<SpeciesNumber[0]; l++)
          {
            do
            {// ~ 20% distortion in C-sublattice
              GaussDv = gsl_ran_gaussian(Random, Sigma) + Mu;
            } while ((GaussDv <= MinDist) || (GaussDv >= MaxDist));

            NewCoordC[m][0] = CoordC[l][0] + i*(RealBasis[0][0]) + j*(RealBasis[
1][0]) + k*(RealBasis[2][0]) + GaussDv;
            NewCoordC[m][1] = CoordC[l][1] + i*(RealBasis[0][1]) + j*(RealBasis[
1][1]) + k*(RealBasis[2][1]) + GaussDv;
            NewCoordC[m][2] = CoordC[l][2] + i*(RealBasis[0][2]) + j*(RealBasis[
1][2]) + k*(RealBasis[2][2]) + GaussDv;
            m++;
          }
          k++;
        }while(k < N);
        j++;
      }while(j < N);
      i++;
    }while(i < N);

//for Ca
    m=0;

    i = -N;
    do
    {
      j = -N;
      do
      {
        k = -N;
        do
        {
          for(l=0; l<SpeciesNumber[1]; l++)
          {
            do
            {
              GaussDv = gsl_ran_gaussian(Random, Sigma) + Mu;
            } while ((GaussDv <= MinDist) || (GaussDv >= MaxDist));
//Simplest case, insert the distortion only in one direction (X)

            NewCoordCa[m][0] = CoordCa[l][0] + i*(RealBasis[0][0]) + j*(RealBasi
```

```
s[1][0]) + k*(RealBasis[2][0]) + GaussDv;
            NewCoordCa[m][1] = CoordCa[l][1] + i*(RealBasis[0][1]) + j*(RealBasi
s[1][1]) + k*(RealBasis[2][1]) + GaussDv;
            NewCoordCa[m][2] = CoordCa[l][2] + i*(RealBasis[0][2]) + j*(RealBasi
s[1][2]) + k*(RealBasis[2][2]) + GaussDv;
            m++;
          }
          k++;
        }while(k < N);
        j++;
      }while(j < N);
      i++;
    }while(i < N);
  }

  else if(EOCell == 'O')//cell is asymmetric about
  {                                //the origin
//for C
    i = -N;//+1 is to gerenate the edge atoms for PDFs
    do
    {
      j = -N;
      do
      {
        k = -N;
        do
        {
          for(l=0; l<SpeciesNumber[0]; l++)
          {
            do
            {// ~ 20% distortion in C-sublattice
              GaussDv = gsl_ran_gaussian(Random, Sigma) + Mu;
            } while ((GaussDv <= MinDist) || (GaussDv >= MaxDist));

            NewCoordC[m][0] = CoordC[l][0] + i*(RealBasis[0][0]) + j*(RealBasis[
1][0]) + k*(RealBasis[2][0]) + GaussDv;
            NewCoordC[m][1] = CoordC[l][1] + i*(RealBasis[0][1]) + j*(RealBasis[
1][1]) + k*(RealBasis[2][1]) + GaussDv;
            NewCoordC[m][2] = CoordC[l][2] + i*(RealBasis[0][2]) + j*(RealBasis[
1][2]) + k*(RealBasis[2][2]) + GaussDv;
            m++;
          }
          k++;
        }while(k <= N);
        j++;
      }while(j <= N);
      i++;
    }while(i <= N);

//for Ca
    m=0;

    i = -N;
    do
    {
      j = -N;
      do
      {
        k = -N;
        do
        {
          for(l=0; l<SpeciesNumber[1]; l++)
          {
```

```
            do
            {
              GaussDv = gsl_ran_gaussian(Random, Sigma) + Mu;
            } while ((GaussDv <= MinDist) || (GaussDv >= MaxDist));
//Simplest case, insert the distortion only in one direction (X)

            NewCoordCa[m][0] = CoordCa[l][0] + i*(RealBasis[0][0]) + j*(RealBasi
s[1][0]) + k*(RealBasis[2][0]) + GaussDv;
            NewCoordCa[m][1] = CoordCa[l][1] + i*(RealBasis[0][1]) + j*(RealBasi
s[1][1]) + k*(RealBasis[2][1]) + GaussDv;
            NewCoordCa[m][2] = CoordCa[l][2] + i*(RealBasis[0][2]) + j*(RealBasi
s[1][2]) + k*(RealBasis[2][2]) + GaussDv;
            m++;
          }
          k++;
        }while(k <= N);
        j++;
      }while(j <= N);
      i++;
    }while(i <= N);
  }

  gsl_rng_free(Random);

/*============================================================================*/

//Form the Carbonate plane centered around C atoms from the known CO3 tilt distr
ibution

/*For Calcite*/
  int n=3; //in 1 cell there are 3+3 alternate Carbonate planes
  int ExSt=1;
  long int TotalONum = 3*TotalCNum;
  float NewCoordO[TotalONum][3];
  float zMinC = NewCoordC[0][2], temp=0.0, BondDist=1.287;
  float HeightC = RealBasis[2][2]/6;
  float O1x, O1y, O1z, O2x, O2y, O2z, O3x, O3y, O3z;
  float Random1, Random2;
  float Theta=0.0, Phi=0.0, sum;
  float THETA[3][3], PHI[3][3], T[3][3];

  FILE *FITfp=NULL;
  float ThetaMax=0.35, PhiMax=1.57, yIntercept=6.0, Slope=-1.0;

  FITfp = fopen("ThetaPhiFit.dat","r");
  fscanf(FITfp,"%f %f %f %f",&ThetaMax,&Slope,&yIntercept,&PhiMax);
  fclose(FITfp);

  FILE *ThPhiFP=NULL;
  ThPhiFP = fopen("SampledThPhi.dat","w");

//Finding the lowest C plane
  i = 0;
  for(i=0;i<TotalCNum;i++)
  {
    if(zMinC >= NewCoordC[i][2])
    {
      temp = NewCoordC[i][2];
      zMinC = temp;
    }
  }

//Fill-up the Oxygen positions in the form of alternet planes
```

```
  m = 0;
  for(l=0; l<TotalCNum; l++)
  {
    ExSt = Status(N,EOCell,n,HeightC,zMinC,NewCoordC[l][2]);
    if(ExSt == 0)
    {
      O1x = -BondDist;
      O1y = 0.0;
      O1z = 0.0;

      O2x = BondDist*sin(PI/6);
      O2y = -BondDist*cos(PI/6);
      O2z = 0.0;

      O3x = BondDist*sin(PI/6);
      O3y = BondDist*cos(PI/6);
      O3z = 0.0;

//Tilt the Carbonate plane.
      Theta = THeta(ThetaMax, Slope, yIntercept);
      Phi = PHi(PhiMax);
//For Pure Calcite
//      Theta = 0.0;
//      Phi = 0.0;

      fprintf(ThPhiFP,"%f %f\n",Theta,Phi);

//Creating PHI matix, i.e. rotation about Z-axis
      PHI[0][0] = cos(Phi);
      PHI[0][1] = sin(Phi);
      PHI[0][2] = 0.0;
      PHI[1][0] = -sin(Phi);
      PHI[1][1] = cos(Phi);
      PHI[1][2] = 0.0;
      PHI[2][0] = 0.0;
      PHI[2][1] = 0.0;
      PHI[2][2] = 1.0;

//Creating THETA matrix, i.e. rotation about X-axis
      THETA[0][0] = 1.0;
      THETA[0][1] = 0.0;
      THETA[0][2] = 0.0;
      THETA[1][0] = 0.0;
      THETA[1][1] = cos(Theta);
      THETA[1][2] = sin(Theta);
      THETA[2][0] = 0.0;
      THETA[2][1] = -sin(Theta);
      THETA[2][2] = cos(Theta);

//Creating Transformation matix, combined rotation matrix: first PHI then THETA
      for(i=0;i<3;i++)
      {
        for(j=0;j<3;j++)
        {
          sum = 0.0;
          for(k=0;k<3;k++)
          {
            sum = sum + PHI[i][k]*THETA[k][j];
          }
          T[i][j] = sum;
        }
      }
```

```
//Tilted Carbonate group's Oxygen Co-ordinate
      NewCoordO[m][0]=T[0][0]*O1x + T[0][1]*O1y + T[0][2]*O1z + NewCoordC[l][0];
      NewCoordO[m][1]=T[1][0]*O1x + T[1][1]*O1y + T[1][2]*O1z + NewCoordC[l][1];
      NewCoordO[m][2]=T[2][0]*O1x + T[2][1]*O1y + T[2][2]*O1z + NewCoordC[l][2];

      NewCoordO[m+1][0]=T[0][0]*O2x + T[0][1]*O2y + T[0][2]*O2z + NewCoordC[l][0
];
      NewCoordO[m+1][1]=T[1][0]*O2x + T[1][1]*O2y + T[1][2]*O2z + NewCoordC[l][1
];
      NewCoordO[m+1][2]=T[2][0]*O2x + T[2][1]*O2y + T[2][2]*O2z + NewCoordC[l][2
];

      NewCoordO[m+2][0]=T[0][0]*O3x + T[0][1]*O3y + T[0][2]*O3z + NewCoordC[l][0
];
      NewCoordO[m+2][1]=T[1][0]*O3x + T[1][1]*O3y + T[1][2]*O3z + NewCoordC[l][1
];
      NewCoordO[m+2][2]=T[2][0]*O3x + T[2][1]*O3y + T[2][2]*O3z + NewCoordC[l][2
];
    }
    else
    {
      O1x = BondDist;
      O1y = 0.0;
      O1z = 0.0;

      O2x = -BondDist/2.0;
      O2y = 0.866*BondDist;
      O2z = 0.0;

      O3x = -BondDist/2.0;
      O3y = -0.866*BondDist;
      O3z = 0.0;
//Tilt the Carbonate plane.
      Theta = THeta(ThetaMax, Slope, yIntercept);
      Phi = PHi(PhiMax);
//For Pure Calcite
//      Theta = 0.0;
//      Phi = 0.0;

         fprintf(ThPhiFP,"%f %f\n",Theta,Phi);

//Creating PHI matrix
      PHI[0][0] = cos(Phi);
      PHI[0][1] = sin(Phi);
      PHI[0][2] = 0.0;
      PHI[1][0] = -sin(Phi);
      PHI[1][1] = cos(Phi);
      PHI[1][2] = 0.0;
      PHI[2][0] = 0.0;
      PHI[2][1] = 0.0;
      PHI[2][2] = 1.0;

//Creating THETA matrix
      THETA[0][0] = 1.0;
      THETA[0][1] = 0.0;
      THETA[0][2] = 0.0;
      THETA[1][0] = 0.0;
      THETA[1][1] = cos(Theta);
      THETA[1][2] = sin(Theta);
      THETA[2][0] = 0.0;
      THETA[2][1] = -sin(Theta);
      THETA[2][2] = cos(Theta);
```

```
//Creating Transformation matrix
      for(i=0;i<3;i++)
      {
        for(j=0;j<3;j++)
        {
          sum = 0.0;
          for(k=0;k<3;k++)
          {
            sum = sum + THETA[i][k]*PHI[k][j];
          }
          T[i][j] = sum;
        }
      }

//Tilted Carbonate group's Oxygen Co-ordinate
      NewCoordO[m][0]=T[0][0]*O1x + T[0][1]*O1y + T[0][2]*O1z + NewCoordC[l][0];
      NewCoordO[m][1]=T[1][0]*O1x + T[1][1]*O1y + T[1][2]*O1z + NewCoordC[l][1];
      NewCoordO[m][2]=T[2][0]*O1x + T[2][1]*O1y + T[2][2]*O1z + NewCoordC[l][2];

      NewCoordO[m+1][0]=T[0][0]*O2x + T[0][1]*O2y + T[0][2]*O2z + NewCoordC[l][0
];
      NewCoordO[m+1][1]=T[1][0]*O2x + T[1][1]*O2y + T[1][2]*O2z + NewCoordC[l][1
];
      NewCoordO[m+1][2]=T[2][0]*O2x + T[2][1]*O2y + T[2][2]*O2z + NewCoordC[l][2
];

      NewCoordO[m+2][0]=T[0][0]*O3x + T[0][1]*O3y + T[0][2]*O3z + NewCoordC[l][0
];
      NewCoordO[m+2][1]=T[1][0]*O3x + T[1][1]*O3y + T[1][2]*O3z + NewCoordC[l][1
];
      NewCoordO[m+2][2]=T[2][0]*O3x + T[2][1]*O3y + T[2][2]*O3z + NewCoordC[l][2
];
    }
    m = 3*l+3;
  }

  fclose(ThPhiFP);

/*============================================================================*/

/* Writing the Co-ordinates of the atoms along with their Scattering factors in
a file. We chose the scattering factor with s=0.25 Ang^-1, where s= sin(theta)/L
ambda, since inter-planer distance between two adjacent Ca-Ca planes and CO3-CO3
 planes is 2.84 Ang. s=1/(2*d) */

  FILE *ofp=NULL;
  FILE *XtalFP=NULL;
  FILE *PDFfp=NULL;

  ofp = fopen("Coordinate.dat","w");
  XtalFP = fopen("NewCrystal.xyz","w");
  PDFfp = fopen("PDFinput","w");

  long int TotalAtomNum = (TotalCNum + TotalCaNum + TotalONum);// substructing O
 in H2O
  fprintf(XtalFP,"%ld\n\n",TotalAtomNum);
  fprintf(PDFfp,"%s %s %s\n","C","Ca","O");
  fprintf(PDFfp,"%ld %ld %ld\n",TotalCNum, TotalCaNum, TotalONum);
  fprintf(PDFfp,"%d\n",N);

  for(i=0;i<3;i++)
  {
    fprintf(PDFfp,"%f %f %f\n",RealBasis[i][0],RealBasis[i][1],RealBasis[i][2]);
```

```
  }

//Writing the coordinates of C
  for(i=0;i<TotalCNum;i++)
  {
    fprintf(XtalFP,"%s %f %f %f\n","C",NewCoordC[i][0], NewCoordC[i][1], NewCoordC
[i][2]);
    fprintf(ofp,"%f %f %f %f %f %f %f %f %f %f %f\n",NewCoordC[i][0], NewCoordC[i][1],
NewCoordC[i][2],0.73,37.0,1.20,11.30,0.46,2.81,0.13,0.35);// Last 8 numbers are
the electron scattering factor parameters [4 a and 4 b parameters from Doyle and
 Turner Acta Cryst. (1968) A24, 390; written like a1,b1,a2,b2...]
    fprintf(PDFfp,"%f %f %f %s\n",NewCoordC[i][0],NewCoordC[i][1],NewCoordC[i][2],
"!C"); //for X-Ray diffraction from same paper
  }

//Writing the coordinates of Ca
  for(i=0;i<TotalCaNum;i++)
  {
    fprintf(XtalFP,"%s %f %f %f\n","Ca",NewCoordCa[i][0], NewCoordCa[i][1], NewCoo
rdCa[i][2]);
    fprintf(ofp,"%f %f %f %f %f %f %f %f %f %f %f\n",NewCoordCa[i][0], NewCoordCa[i][1]
, NewCoordCa[i][2],4.47,99.52,2.97,22.70,1.97,4.20,0.48,0.42);
    fprintf(PDFfp,"%f %f %f %s\n",NewCoordCa[i][0], NewCoordCa[i][1], NewCoordCa[i
][2],"!Ca");
  }

//Writing the coordinates of O
  for(i=0;i<TotalONum;i++)
  {
    fprintf(XtalFP,"%s %f %f %f\n","O",NewCoordO[i][0], NewCoordO[i][1], NewCoordO
[i][2]);
    fprintf(ofp,"%f %f %f %f %f %f %f %f %f %f %f\n",NewCoordO[i][0], NewCoordO[i][1],
NewCoordO[i][2],0.45,23.78,0.92,7.62,0.47,2.14,0.14,0.30);
    fprintf(PDFfp,"%f %f %f %s\n",NewCoordO[i][0], NewCoordO[i][1], NewCoordO[i][2
],"!O");
  }

  fclose(XtalFP);
  fclose(ofp);
  fclose(PDFfp);

/*=============================================================================*/

// Generate receprocal space basis vectors
// /*Define the center of the receprocal lattice (according to Ewald sphere cons
truction) assuming the incident radiation coming along negetive Z direction. The
 wavelength of the electrons in a 10 kV SEM is then 12.3 x 10âM-^HM-^R12  m (12.
3 pm) while in a 200 kV TEM the wavelength is 2.5 pm. In comparison the waveleng
th of X-rays usually used in X-ray diffraction is in the order of 100 pm (Cu kÎ±
: Î»=154 pm).*/

  float Lambda = 0.025; // For TEM in Angstrom (200 KeV)
//  float LambdaX = 1.54; // For X-ray diffraction
  float rEwald = 1/Lambda;//radius of the Ewald sphere
  float vRealBasis=0.0;
  float RecpBasis[3][3];
  long int GMax[1][3];

//Volume of the real-space unit-cell.
  vRealBasis = RealBasis[0][0]*(RealBasis[1][1]*RealBasis[2][2] - RealBasis[2][1
]*RealBasis[1][2]) + RealBasis[0][1]*(RealBasis[2][0]*RealBasis[1][2] - RealBasi
s[2][2]*RealBasis[1][0]) + RealBasis[0][2]*(RealBasis[1][0]*RealBasis[2][1] - Re
alBasis[2][0]*RealBasis[1][1]);
```

```
//A=
  RecpBasis[0][0] = (2*PI)*(RealBasis[1][1]*RealBasis[2][2] - RealBasis[2][1]*Re
alBasis[1][2])/vRealBasis;
  RecpBasis[0][1] = (2*PI)*(RealBasis[2][0]*RealBasis[1][2] - RealBasis[2][2]*Re
alBasis[1][0])/vRealBasis;
  RecpBasis[0][2] = (2*PI)*(RealBasis[1][0]*RealBasis[2][1] - RealBasis[2][0]*Re
alBasis[1][1])/vRealBasis;

//B=
  RecpBasis[1][0] = (2*PI)*(RealBasis[2][1]*RealBasis[0][2] - RealBasis[0][1]*Re
alBasis[2][2])/vRealBasis;
  RecpBasis[1][1] = (2*PI)*(RealBasis[0][0]*RealBasis[2][2] - RealBasis[0][2]*Re
alBasis[2][0])/vRealBasis;
  RecpBasis[1][2] = (2*PI)*(RealBasis[2][0]*RealBasis[0][1] - RealBasis[0][0]*Re
alBasis[2][1])/vRealBasis;

//C=
  RecpBasis[2][0] = (2*PI)*(RealBasis[0][1]*RealBasis[1][2] - RealBasis[1][1]*Re
alBasis[0][2])/vRealBasis;
  RecpBasis[2][1] = (2*PI)*(RealBasis[1][0]*RealBasis[0][2] - RealBasis[1][2]*Re
alBasis[0][0])/vRealBasis;
  RecpBasis[2][2] = (2*PI)*(RealBasis[0][0]*RealBasis[1][1] - RealBasis[1][0]*Re
alBasis[0][1])/vRealBasis;

  for(j=0; j<3; j++)
  {
    GMax[0][j] = (rEwald/(sqrt(pow(RecpBasis[j][0],2) + pow(RecpBasis[j][1],2) +
 pow(RecpBasis[j][2],2))) + 1.0);
  }

/*============================================================================*/

//Generate Receprocal lattice points(mesh/grid) around Ewald-Sphere and Search w
hich receprocal points are on the Ewald sphere i.e. which receprocal points are
at a distance 1/Lambda away from (0,0,0).

  FILE *DirectionFP=NULL;
  DirectionFP = fopen("Directions.dat","r");
  int DirectionNum = 1; //Number of lines in Directions.dat
                        //Best selection for Calcite 4, Aragonite 5
  long int h, G1, G2, G3;//, H[10000], K[10000], L[10000];
  long int count=0;
  int QxBinNum=9, QyBinNum=9,QzBinNum=5;
  long int QNum = 1500*QxBinNum*QyBinNum*QzBinNum;//1500 is the number of select
ed Brag directions
  float dQx=1.0, dQy=1.0, dQz=0.5;
  float dqx=(dQx/QxBinNum), dqy=(dQy/QyBinNum), dqz=(dQz/QzBinNum); //These are
for finer mesh around proper direction. I calculated for an angular (2*theta) sp
read of 0.1 deg dq ~ 0.5. Since Recp-a or Recp-b ~ 2*Recp-c, hence I took the bi
ns like that.
  float qX[QNum], qY[QNum], qZ[QNum], q[QNum]; //size will depend on number of d
irections, gap-size and mesh-size in recp-space.For 4 directions number of G~150
0, array size will be (1500*QxBinNum*QyBinNum*QzBinNum)
  float temp1,Gx, Gy, Gz;
  float tmp=0.0, ModG=5.0;//for 2*theta=1 deg, Lambda = 0.025 Ang
  float xIn, yIn, zIn, rIn; //Read the co-ordinates the direction
  int d, hIn, kIn, lIn; // from the Directions.dat file

  i=0; j=0; m=0;

  for(d=0;d<DirectionNum;d++)//loop for different direction
  {
```

```
    fscanf(DirectionFP,"%d %d %d %f %f %f %f",&hIn,&kIn,&lIn,&xIn,&yIn,&zIn,&rIn);

    h = GMax[0][0];
    k = GMax[0][1];
    l = GMax[0][2];

// Receprocal space basis vectors about the receprocal space center (which is rE
wald down along X or Y or Z direction depending on which direction electron beam
 is coming).
    for(G1=-h; G1<=h; G1++)
    {
      for(G2=-k; G2<=k; G2++)
      {
        for(G3=-l; G3<=l; G3++)
        {
          if((G1 != 0) && (G2 != 0) && (G3 != 0))
          {
            Gx = G1*RecpBasis[0][0]+G2*RecpBasis[1][0]+G3*RecpBasis[2][0] - xIn;

            Gy = G1*RecpBasis[0][1]+G2*RecpBasis[1][1]+G3*RecpBasis[2][1] - yIn;
            Gz = G1*RecpBasis[0][2]+G2*RecpBasis[1][2]+G3*RecpBasis[2][2] - zIn;
            temp1 = sqrt(Gx*Gx + Gy*Gy + Gz*Gz);
// Receprocal space scales: A*=B*=1.45 Ang^-1, C*=0.368 Ang^-1. the threshold sh
ould be less than the right scale (depensing on which direction the incident bea
m is coming). Best gap 0.8.
            if((temp1 >= (rEwald-0.8)) && (temp1 <= (rEwald+0.8)))
            {
              tmp = sqrt(pow((Gx+xIn),2) + pow((Gy+yIn),2) + pow((Gz+zIn),2));
              if(tmp <= ModG)
              {
//q is a Scattering vector (or vector diffence in receprocal space), not from th
e center of Ewald Sphere. Here we want to generate much closer K-space grid abou
t each diffraction direction so that we can see the shape of the peaks (due to l
imited size of the crystal).
                for(i=-(QxBinNum-1)/2; i<=(QxBinNum-1)/2; i++)
                {
                  for(j=-(QyBinNum-1)/2; j<=(QyBinNum-1)/2; j++)
                  {
                    for(m=-(QzBinNum-1)/2; m<=(QzBinNum-1)/2; m++)
                    {
                      qX[count] = Gx + xIn + i*RecpBasis[0][0]*dqx + j*RecpBasis
[1][0]*dqy + m*RecpBasis[2][0]*dqz;
                      qY[count] = Gy + yIn + i*RecpBasis[0][1]*dqx + j*RecpBasis
[1][1]*dqy + m*RecpBasis[2][1]*dqz;
                      qZ[count] = Gz + zIn + i*RecpBasis[0][2]*dqx + j*RecpBasis
[1][2]*dqy + m*RecpBasis[2][2]*dqz;
                      q[count] = sqrt(pow(qX[count],2) + pow(qY[count],2) + pow(
qZ[count],2));
                      count++;
                    }
                  }
                }
              }
            }
          }
        }
      }
    }
  }

  fclose(DirectionFP);
//  printf("%ld\n",count);
```

```
/*============================================================================*/

//Calculate the intensity as a function of selected G points and write the inten
sities as a function of the radius on X-Y cut of Ewald sphere.

  FILE *ifp1=NULL;
  FILE *outfp=NULL;

  ifp1 = fopen("Coordinate.dat","r");
  outfp = fopen("CalcitePeaks.dat","w");

  float X, Y, Z, Sfactor, Phase, TempSfactor=0.0;
  float a1=0.0,a2=0.0,a3=0.0,a4=0.0,b1=0.0,b2=0.0,b3=0.0,b4=0.0;
  float sSq; //sSq=(sin(theta)/Lambda)^2 = |G|^2/(4*PI)^2
  float ReF, ImF, I[count];//qR[count];
  i=0; j=0;

  for(i=0; i<count; i++)
  {//over the selected points on Ewald sphere
    ReF = 0.0;
    ImF = 0.0;
    I[i] = 0.0;

    sSq = (q[i]*q[i])/(16*PI*PI);

    for(j=0; j<TotalAtomNum; j++)
    {
      fscanf(ifp1,"%f %f %f %f %f %f %f %f %f %f %f",&X,&Y,&Z,&a1,&b1,&a2,&b2,&a3,&b3,
&a4,&b4);
      Sfactor=a1*exp(-b1*sSq)+a2*exp(-b2*sSq)+a3*exp(-b3*sSq)+a4*exp(-b4*sSq);//
+C for Xray
      Phase = (qX[i]*X + qY[i]*Y + qZ[i]*Z);
      ReF += Sfactor*cos(Phase);
      ImF += Sfactor*sin(Phase);
    }
    rewind(ifp1);

    I[i] = (pow(ReF,2) + pow(ImF,2));
    fprintf(outfp,"%f %f\n",q[i],I[i]);
   }

  fclose(outfp);
  fclose(ifp1);

/*============================================================================*/

/*
//Add the shape function to the peaks

  int qBinNum=1000, qPointsNum=count*(qBinNum+1); k=0; i=0; j=0;
  float Aparture=(2*N+1)*(2*RealBasis[0][0]+RealBasis[2][2])/3;//Avg crystal siz
e
  float Dq = 5*(2*PI/Aparture), qBinSize=Dq/qBinNum;
  float q[qPointsNum], Iq[qPointsNum], Arg;

  for(i=0;i<count;i++)
  {
    for(j=-qBinNum/2;j<=qBinNum/2;j++)
    {
      q[k] = qR[i] + j*qBinSize;
      Arg = ((q[k]-qR[i])*Aparture)/2.0;
      Iq[k] = I[i]*ShapeFn(Aparture, Arg);
```

```
      k++;
    }
  }
*/

/*=============================================================================*/

// Sort the intensities according to increasing radii.

  float temp2, temp3, temp4, temp5, temp6;
  float tmp1=0.0, Dspacing, TwoTheta;
  long int qPointsNum = count;

  for(i=0;i<count;i++)
  {
    for(j=i+1;j<count;j++)
    {
      if(q[i] > q[j])
      {
        temp2 = q[i];
        q[i] = q[j];
        q[j] = temp2;

        temp3 = I[i];
        I[i] = I[j];
        I[j] = temp3;
      }
    }
  }

//Finding the Average Intensity
  float Isum=0.0, Iavg=0.0;
  for(i=0;i<qPointsNum;i++)
  {
    Isum += I[i];//excluding the unscattered beam
  }

  Iavg = Isum/qPointsNum;

  for(i=0;i<qPointsNum;i++)
  {
    Dspacing = (2*PI)/q[i];
    TwoTheta = ((180*Lambda)/(Dspacing*PI));
  }

/*=============================================================================*/

// Add all the Intensities on the same radius to obtain diffraction line profile
 as a function of 2Theta (Theta is glancing angle).

  FILE *ofp1=NULL;
  ofp1 = fopen("LineProfile.dat","w");

  float R0=ModG/25,Rnew=0.0,Rold=0.0,Ravg=0.0;
  float Area = PI*R0*R0;
  float Intensity=0.0, TmpI=0.0, TempI=0.0;

  for(i=0;i<qPointsNum;i++)
  {
    Intensity=0.0;
    TempI = TmpI;;
    TmpI = 0.0;
    Rnew = sqrt((Area/PI)*(i+1));
```

```
    Rold = sqrt(i*Area/PI);
    Ravg = (Rnew+Rold)/2;
    TwoTheta = 2*((180*Ravg*Lambda)/(4*PI*PI));

    for(j=0;j<qPointsNum;j++)
    {
      if((q[j] >= Rold) && (q[j] < Rnew))
      {
        TmpI += I[j]/Iavg;
      }
    }

//smoothing the intensity due to uneven grids
    if(i > 5)
    {
      Intensity = (0.5*TmpI + 0.5*TempI);
      fprintf(ofp1,"%f %f\n",TwoTheta,Intensity);
    }
    else
    {
      Intensity = TmpI;
      fprintf(ofp1,"%f %f\n",TwoTheta,Intensity);
    }

    if(Rnew >= q[qPointsNum-1]) //break when 2Theta = desired angle
    {
      break;
    }
  }

  fclose(ofp1);

/*============================================================================*/

//Plotting in GNU-plot

  gnuplot("plot 'LineProfile.dat' using 1:2 w l;\n");

  return 0;
}

/*====================End of Main. User Defined Functions====================*/

/* Function to decide alternate carbonate planes are facing towards
 +X or-X axis. */
int Status(int N,char EOCell,int n,float HeightC,float zMinC,float CoordCz)
{
  int i=0, ex=1;
  float zMin=0.0, zMax=0.0;
  float Threshold = 1.30; //Z Range of O while CO3 planes tilt. 1.33<HeightC/2 f
or Calcite
  if(EOCell == 'E')
  {
    for(i=0;i<2*N*n;i++) //supercell extends 2N times
    {
      zMin = 2*i*HeightC + zMinC - Threshold;
      zMax = 2*i*HeightC + zMinC + Threshold;
      if((CoordCz >= zMin) && (CoordCz <= zMax))
      {
        ex = 0;
        break;
      }
    }
```

```
  }
  else if(EOCell == 'O')
  {
    for(i=0;i<(2*N+1)*n;i++) //supercell extends (2N+1) times
    {
      zMin = 2*i*HeightC + zMinC - Threshold;
      zMax = 2*i*HeightC + zMinC + Threshold;
      if((CoordCz >= zMin) && (CoordCz <= zMax))
      {
        ex = 0;
        break;
      }
    }
  }
  return ex;
}

/*============================================================================*/

/* Function to find theta at random from its distributions */

float THeta(float ThetaMax, float Slope, float yIntercept)
{
  float RandTheta;
  float Theta;
  float ThetaNorm = 1/(((Slope/2)*ThetaMax*ThetaMax) + (yIntercept*ThetaMax));
// Choosing theta at random; Theta is a linear distribution
  RandTheta=((float) rand()/((float)(RAND_MAX)+(float) (1))); //Random number be
tween 0 to 1
  Theta = (-yIntercept + sqrt(pow(yIntercept,2) + 2*Slope*(RandTheta/ThetaNorm))
)/Slope;

  return Theta;
}

/*============================================================================*/

//Function to find phi at random

float PHi(float PhiMax)
{
  float Phi, RandPhi;

  RandPhi=((float) rand()/((float)(RAND_MAX) + (float) (1)))*PhiMax;
  Phi=RandPhi;

  return Phi;
}

/*============================================================================*/

//Function to plot using GNU-plot.

void gnuplot(const char *gnucommand)
{
  char syscommand[1024];
  sprintf(syscommand, "echo \"%s\" | gnuplot -persist", gnucommand);
  system(syscommand);
}

/*~~~~~~~~~~~~~~~~~~~~~~~~~~~~~~~~~~The End~~~~~~~~~~~~~~~~~~~~~~~~~~~~~~~~~~~~*/
```